



Cite this: DOI: 10.1039/d6sc01361a

Unlocking the potential of Bi₂S₃ for photocatalysis: a roadmap for next-generation solar catalysts

Wei Zhao,^{†a} Qing Chen,^{†c} Lifeng Cai,^{*a} Jie Liang^{*b} and Fang-Xing Xiao^{†c}

Photocatalysis enables the direct conversion of solar energy into chemical fuels, presenting a compelling strategy to mitigate the global energy crisis and environmental pollution. However, traditional photocatalysts are severely hampered by inefficient visible-light harvesting and undesirably rapid recombination of photogenerated carriers, which bottlenecks their large-scale practical deployment. Thus, developing efficient, stable, and broadband-responsive photocatalytic materials remains a paramount research imperative. Bismuth sulfide (Bi₂S₃), a prototypical narrow-bandgap semiconductor, has recently garnered immense interest. Its judiciously positioned band edges and strong visible-light absorption confer distinct advantages for solar-driven photoredox reactions. Despite significant advances, the field still lacks a comprehensive and timely review consolidating Bi₂S₃-based artificial photosystems. This review systematically summarizes the latest progress in Bi₂S₃-based photocatalysts, with a particular focus on morphology control, heterojunction construction, elemental doping, and defect engineering. We elucidate how these strategies precisely manipulate the electronic structure, facilitate charge separation, broaden light absorption, and enhance material stability. Furthermore, we outline critical future perspectives: (i) designing novel multicomponent architectures, (ii) unraveling the kinetic mechanisms of interfacial carrier transfer, and (iii) validating scalable performance under realistic environmental conditions. This review provides a holistic roadmap for Bi₂S₃-mediated photoredox catalysis, serving as a vital resource for researchers advancing solar energy conversion technologies.

Received 15th February 2026
Accepted 13th April 2026

DOI: 10.1039/d6sc01361a

rsc.li/chemical-science

1. Introduction

Photocatalysis offers a unique advantage in directly converting solar energy into chemical energy, showing broad prospects for addressing energy shortages and environmental remediation.^{1–3} The core of photocatalysis involves photo-exciting semiconductors to utilize the electrons and holes for redox reactions. This fundamental process relies heavily on semiconductor materials absorbing photon energy to create electro-hole pairs, which then drive a series of redox reactions such as photocatalytic H₂ production, CO₂ reduction, mineralization of organic pollutants, and bacterial disinfection.^{4–7} This process mainly consists of three consecutive yet interrelated key stages, which includes photon absorption and carrier excitation, charge separation and migration, and surface redox reactions.

Despite its great potential, photocatalysis still faces several technical hurdles before large-scale deployment. First, the separation efficiency of photogenerated charge carriers is intrinsically low. Most electron-hole pairs recombine within nanoseconds to picoseconds after formation, severely limiting the quantum yield. Thus, low quantum efficiency and severe carrier recombination remain long-standing bottlenecks for photocatalytic materials.⁸ Second, conventional photocatalysts such as TiO₂ absorb only UV light, which accounts for less than 5% of the solar spectrum, leading to poor overall solar energy utilization.⁹ Moreover, current photocatalytic materials still exhibit shortcomings in long-term reaction stability, raw-material cost, and scalable preparation technologies,¹⁰ which further restrict their practical application scope.

The central challenge in photocatalysis is to harvest solar energy efficiently while boosting redox reaction efficiency. To this end, researchers have devoted sustained effort to developing new photocatalysts, such as metal oxides, metal sulfides, and plasmonic metal nanocrystals. Representative metal oxides such as TiO₂ and ZnO exhibit good stability and low cost, yet their wide band gaps restrict absorption mainly to the UV region, leaving visible light largely unutilized.^{11–13} Although graphitic carbon nitride (g-C₃N₄), as a non-metallic semiconductor, offers visible-light activity and high chemical stability, its limited surface area and rapid carrier recombination hinder further enhancement of

^aKey Laboratory of Ecological Environment and Information Atlas, Fujian Provincial University (Putian University), College of Environmental and Biological Engineering, Putian 351100, P. R. China. E-mail: 89437499@qq.com

^bFujian Key Laboratory of Ecological Impacts and Treatment Technologies for Emerging Contaminants, Putian University, Putian 351100, P. R. China. E-mail: ptxylj0321@126.com

^cCollege of Materials Science and Engineering, Fuzhou University, New Campus, Minhou, Fujian Province, 350108, P. R. China. E-mail: fxxiao@fzu.edu.cn

[†] Wei Zhao and Qing Chen contributed equally to this work.



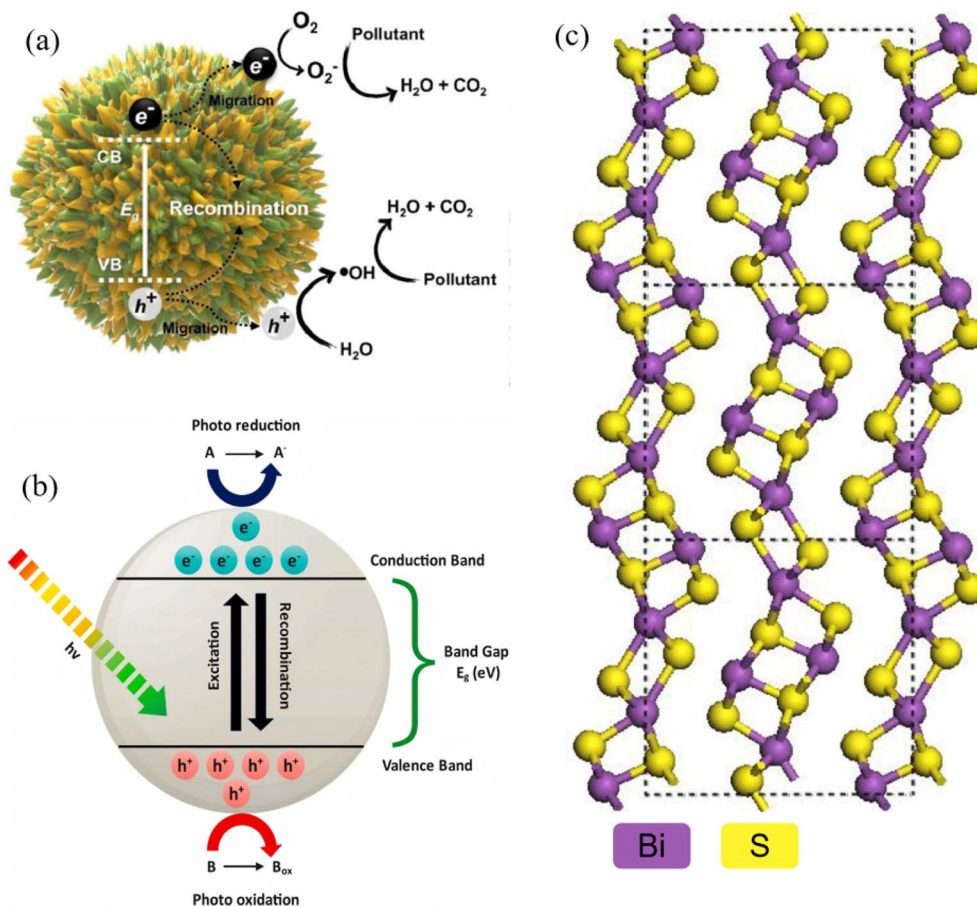


Fig. 1 (a) Photocatalytic mechanism diagram.²⁹ Copyright 2023, Elsevier Ltd. (b) Schematic representation of mechanisms involved in semiconductor-based photocatalysis.² Copyright 2024, Elsevier Ltd. (c) Bi_2S_3 crystal structure and band structure.¹⁶ Copyright 2025, Elsevier.

catalytic performance.¹⁴ Narrow-band-gap sulfides such as CdS exhibit strong visible-light absorption, yet suffer from severe photocorrosion and potential environmental toxicity.¹⁵ Overall, conventional photocatalysts still fail to overcome the simultaneous bottlenecks of high carrier-recombination rate, restricted solar-spectral response, and insufficient long-term stability. Against this backdrop, bismuth sulfide (Bi_2S_3), a V–VI group narrow-band-gap semiconductor, has emerged as a research hotspot owing to its unique structure and optoelectronic properties along with low toxicity, offering a fresh strategy to break the above bottlenecks and driving diverse photocatalytic reactions including CO_2 reduction, N_2 fixation and heavy-metal reduction. The band gap of Bi_2S_3 can be tuned between 1.3 and 1.7 eV, pushing its absorption edge into the near-infrared (*ca.* 800–1000 nm) and covering roughly 40% of the solar energy spectrum. Its high absorption coefficient (10^4 – 10^5 cm^{-1}) endows it with exceptional light-harvesting capability. Moreover, a favorable combination of high carrier mobility and suitable band-edge positions facilitates the efficient charge separation and accelerates charge migration to surface reaction sites, conferring significant advantages in light-conversion kinetics.¹⁶

However, inherent drawbacks such as short carrier-diffusion lengths and facile photocorrosion under illumination still restrict the practical deployment of Bi_2S_3 .¹⁷ To address these issues, a variety of modification strategies have been developed

including morphology control (quantum dots, nanorods, nanosheets),¹⁸ heterojunctions engineering (Type-II, Z-scheme or S-scheme),^{19–21} elemental doping (Fe, N, *etc.*),²² single-atom deposition,²³ sulfur vacancies modulation,^{23,24} and hybridizing with cocatalysts (MoS_2 , NiS).²⁵ These modified strategies provide alternative approaches to accelerate the charge transport kinetics, increase specific surface area, and boost charge separation efficiency of Bi_2S_3 -based artificial photosystems.²⁶ Despite the advancement, there is still lack of timely, comprehensive, and systematic review article that summarizes the latest development of Bi_2S_3 -based artificial photosystems.

In this review, we present a comprehensive 2019–2025 roadmap of Bi_2S_3 -based photocatalysis following a “structure–property–application” hierarchy. Starting with its intrinsic crystal and electronic traits, we summarize the precision-synthesis tools (hot-injection, template, microwave, *etc.*) and dissect the morphology-performance links across dimensions from 0D quantum dots to 3D flower-spheres. We then spotlight Type-II, Z-scheme, p–n and Schottky heterojunctions, coupled with doping, defect and cocatalyst synergies, and showcase their emerging application in photocatalytic pollutant degradation, CO_2 reduction, N_2 fixation, photoelectrochemical (PEC) H_2 evolution and bacterial disinfection. The future perspectives and challenges are finally provided



for further pushing forward the prosperity of Bi_2S_3 -based photocatalysis toward solar energy conversion.

2. Fundamental properties of Bi_2S_3

2.1. Crystal and electronic structure of Bi_2S_3

2.1.1. Lattice structure. Bi_2S_3 crystallizes in an orthorhombic system. Kyono *et al.*, first identified the natural mineral as the orthorhombic stibnite structure (space group $Pnma$) by single-crystal diffraction, with lattice constants $a \approx 11.15 \text{ \AA}$, $b \approx 11.30 \text{ \AA}$, $c \approx 3.98 \text{ \AA}$ and 20 atoms per unit cell (4 formula units of Bi_2S_3).²⁷ The architecture is strongly anisotropic, that is, the fundamental motif is an infinite $(\text{Bi}_2\text{S}_3)_n$ ribbon that propagates in a zig-zag fashion along the c -axis. Within each ribbon Bi is octahedrally coordinated and S is approximately close-packed with every Bi atom bonding to seven S atoms, thereby giving two distinct short (2.589–2.738 \AA , covalent) and long (2.975–3.328 \AA , van-der-Waals-like) bond lengths (Fig. 1). Adjacent ribbons are linked only by these weak Bi–S interactions, yielding a highly anisotropic layered array. Because the lowest surface energy is along the chain direction, crystals grow preferentially into one-dimensional nanowires or nanorods, providing a structural basis for morphology control.²⁸

This orthorhombic lattice is thus a hybrid chain-layer structure whose hallmark is “infinite Bi_2S_3 chains aligned along [001]”. Black *et al.*, using early X-ray crystallography, showed that Bi^{3+} and S^{2-} form endless chains parallel to the c -axis. Specifically, Bi^{3+} occupies a strongly distorted octahedron in which three short covalent Bi–S bonds stabilize the chain and dictate the preferential growth along c .³⁰ Consequently, bonding is covalent and strong along c , whereas the inter-chain interactions perpendicular to the a - b plane are weak van-der-Waals forces. Researchers investigating nanostructure growth emphasize that this bond hierarchy is the key to the facile formation of 1-D nanomorphologies. In other words, rapid c -axis growth is driven by strong covalent bonds, while lateral growth is kinetically hindered by weak inter-chain forces.³¹ The lattice anisotropy directly governs electronic and optical behaviour. Deshpande *et al.*, observed a blue-shifted absorption edge in Bi_2S_3 nanorods and attributed it to the combined effects

of quantum confinement and the oriented chain-like atomic arrangement, which modifies the electronic transition barrier.³²

2.1.2. Electronic band structure. The narrow band gap of Bi_2S_3 (1.3–1.7 eV) (Fig. 2) is the fundamental reason that it can harvest visible-to-near-infrared photons with high efficiency.¹⁶ Density functional theory (DFT) provides an atomistic roadmap for understanding both the gap origin and the catalytic activity of Bi_2S_3 . First-principles calculations show that the valence-band maximum (VBM) originates from hybridized S 3p and Bi 6s orbitals. Because Bi is a heavy element, its 6s level is pushed upward by strong spin orbit coupling (SOC), raising the VBM and thus shrinking the gap. The conduction-band minimum (CBM) is dominated by Bi 6p states, endowing the material with a powerful reduction potential.^{33–36} This unique p–s orbital mixing, amplified by SOC, produces the characteristic narrow gap. The DFT calculations start from the intrinsically SOC-narrowed band gap, proceed through strain fine-tuning, and culminate in interfacial charge reorganization, providing a reliable theoretical tool for interpreting band-gap engineering and heterostructure construction.

2.2. Optical and electrical properties of Bi_2S_3

2.2.1. Light-absorption characteristics. The intrinsic narrow band gap and high density of p–s antibonding states at the valence-band top endow Bi_2S_3 with broadband visible-to-near-infrared (NIR) harvesting. Its absorption edge extends to 800–1000 nm, and the absorption coefficient in the visible region reaches 10^4 – 10^5 cm^{-1} . Recent work has disentangled how size, heterojunctions and local electromagnetic fields jointly tailor the absorption edge, coefficient and hot-electron yield. For example, Li *et al.*³⁸ deposited 6–8 nm Bi_2S_3 quantum dots (QDs) on TiO_2 nanotubes by a SILAR (Successive Ionic Layer Adsorption and Reaction) method. UV-vis diffuse reflectance showed that bulk-like Bi_2S_3 absorbs up to 800 nm (1.3 eV), whereas the $\text{Bi}_2\text{S}_3/\text{TiO}_2$ QD film exhibits a blue-shifted edge at 780 nm (1.59 eV). The average absorption coefficient in the 400–800 nm window reaches $1.2 \times 10^5 \text{ cm}^{-1}$ which is five times that of bare TiO_2 ($2.4 \times 10^4 \text{ cm}^{-1}$), demonstrating that QD confinement preserves high absorbance while enabling gap tunability. When the QD film was used as a photoanode, photogenerated electrons were injected into stainless steel, lowering its potential and preventing corrosion. This solar-driven cathodic protection strategy directly evidences the synergistic high-absorption and efficient-carrier-output feature of Bi_2S_3 QDs. Chen *et al.*³⁹ successfully prepared a $\text{Bi}_2\text{S}_3/\text{ReS}_2$ heterojunction. Coupling with ReS_2 synergistically exploits the narrow band gaps of both components, broadening the light-harvesting range and enhancing absorption intensity. Moreover, tuning the $\text{Bi}_2\text{S}_3/\text{ReS}_2$ mass ratio significantly boosts NIR absorption efficiency. This superior optical absorption underpins efficient photothermal conversion (35.2% efficiency in aqueous solution) and Z-scheme charge transfer, ultimately elevating photocatalytic H_2 evolution performance to 7.36 times that of bare Bi_2S_3 . In another case, Jiang *et al.*⁴⁰ synthesized Bi_2S_3 nanorods with defect structures *via* a solvothermal route. UV-vis-NIR spectroscopy revealed that these nanorods exhibit a broad and intense absorption band in the near-infrared region (700–1400 nm) with a molar extinction coefficient of $12.3 \text{ L g}^{-1} \text{ cm}^{-1}$,

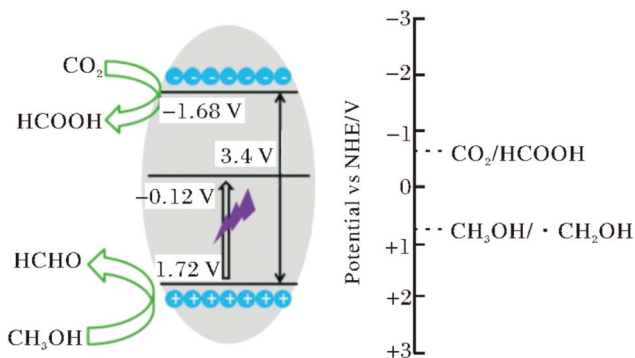


Fig. 2 Band structure of Bi_2S_3 microspheres.³⁷ Copyright 2013, Royal Society of Chemistry.



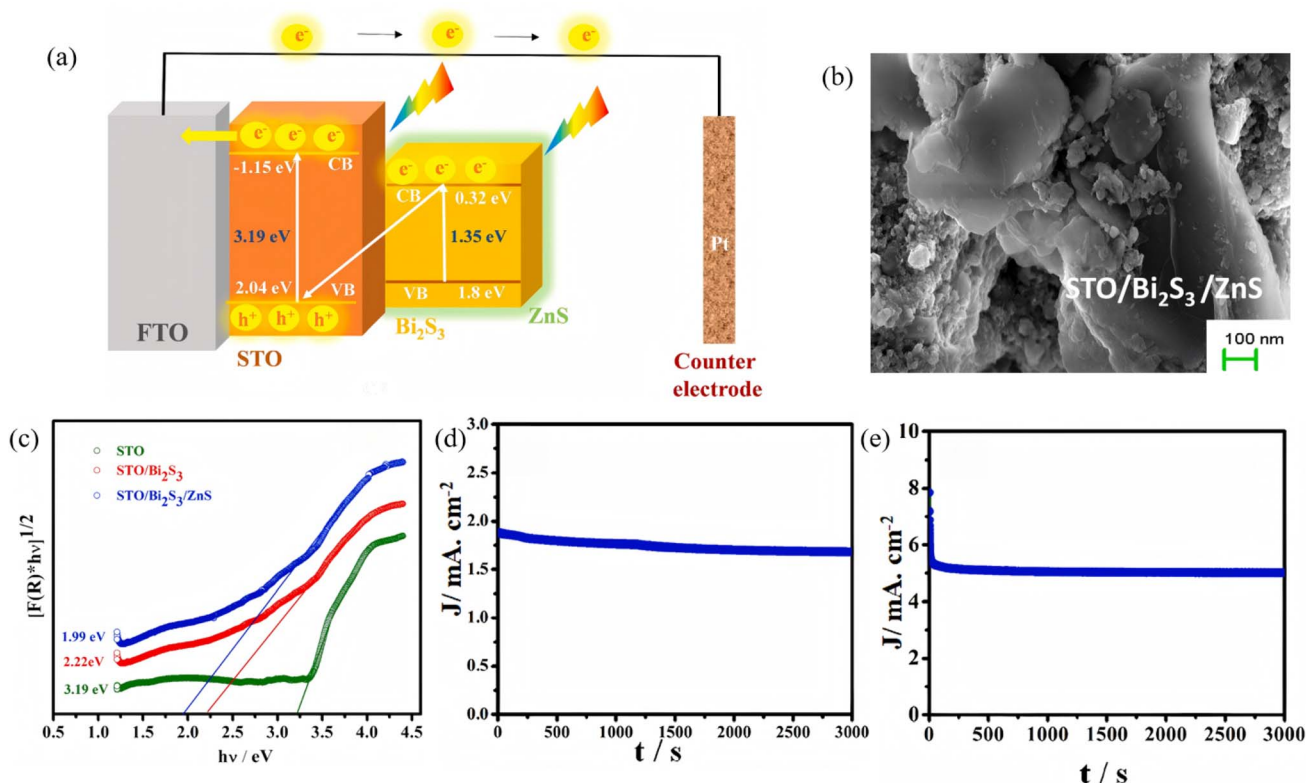


Fig. 3 (a) Schematic representation of the band alignment and mechanism of electron transfer in the STO/Bi₂S₃/ZnS system. (b) SEM image of the STO/Bi₂S₃/ZnS composites. (c) Kubelka–Munk plot of reflectance spectra for band gap estimation. Chronoamperometric (*I*–*t*) curve of STO/Bi₂S₃/ZnS photoelectrode in (d) neutral medium (pH 7), (e) alkaline medium (pH 12.4).⁴¹ Copyright 2024, Elsevier.

significantly higher than conventional Bi₂S₃ nanomaterials. This absorption characteristic originates from the unique morphology and defect structure of the nanorods, wherein the defect structure confers metallic-like absorption properties, while the special morphology modulates the absorption peak position. Their synergy enhances NIR harvesting efficiency, enabling excellent photothermal conversion under 808 nm laser irradiation. This study confirms that the optical absorption properties of Bi₂S₃ nanorods can be tuned through morphology and defect engineering. Collectively, size, defect and morphology engineering can synchronize ultra-broad absorption (400–1200 nm) with efficient photothermal/carrier generation, laying the optical foundation for full-spectrum photocatalysis.

2.2.2. Carrier dynamics. Although the narrow band gap and high absorption coefficient of Bi₂S₃ guarantee efficient harvesting of visible-to-NIR photons, its intrinsic carrier diffusion length is short (~100 nm) and recombination is rapid ($\tau < 10$ ns), giving rise to pronounced bulk and surface losses that severely limit the quantum efficiency of photocatalysis. Recent studies have adopted a hierarchical strategy to unravel and manipulate charge separation and transport in heterostructures. Joy *et al.*⁴¹ deposited an atomic-layer-deposited ZnS passivation layer on SrTiO₃/Bi₂S₃ nanorods to construct a ternary SrTiO₃/Bi₂S₃/ZnS photoanode (Fig. 3). PL spectroscopy revealed that the ZnS layer isolates Bi₂S₃ from direct contact with the electrolyte while providing active states that promote charge transfer, markedly suppressing carrier

recombination. The structure delivers a photocurrent density of 1.89 mA cm⁻² in neutral medium and 5.06 mA cm⁻² in alkaline medium, with a HC-STH (Half-Cell Solar-to-Hydrogen Efficiency) efficiency up to 4.8%, confirming the beneficial role of ZnS passivation in optimizing carrier kinetics. Xiao *et al.*⁴² designed a self-supporting B-g-C₃N_x/Bi₂S₃/CdS dual S-scheme heterojunction film. TRPL (Time-Resolved Photoluminescence) measurements showed significantly longer carrier lifetimes for this ternary architecture compared to binary heterojunctions or bare B-g-C₃N_x. The dual built-in electric fields of the double S-scheme provide multi-channel charge-transfer pathways that effectively suppress charge recombination, achieving a photocatalytic H₂-evolution rate of 4.78 mmol g⁻¹ h⁻¹ and 98.7% oxytetracycline degradation. In summary, hierarchical synergy can prolong carrier lifetime, enable high-velocity shunting and achieve spatial separation in Bi₂S₃-based photosystems, laying the kinetic foundation for efficient full-spectrum photocatalysis.

3. Controllable synthesis of Bi₂S₃ nanomaterials

3.1. Synthesis method

3.1.1. Hydrothermal/solvothermal methods.

Hydrothermal/solvothermal synthesis has become the dominant route for the controlled fabrication of one- to three-dimensional Bi₂S₃ nanostructures, thanks to its simple



equipment, low temperature, high crystallinity, and easily tunable morphology. Fundamentally, it couples reactions inside a sealed autoclave; by adjusting solvent polarity, temperature, and reaction time, the nucleation rate and facet-selective growth kinetics of Bi_2S_3 can be precisely tuned, enabling the targeted construction of ultra-long wires, nanobelts, or hierarchical nanoflowers. In 2003, Liu *et al.*⁴³ first reported a classic solvothermal route for large-scale synthesis of Bi_2S_3 single-crystal nanobelts (Fig. 4a). Using $\text{Bi}(\text{NO}_3)_3 \cdot 5\text{H}_2\text{O}$ and $\text{Na}_2\text{S}_2\text{O}_3$ as precursors, with an aqueous NaOH /glycerol mixed solvent (volume ratio 2 : 1), reaction at 160 °C for 20 h *via* a solid-dissolution-solid transformation yielded single-crystal nanobelts 50–300 nm in width, 20–80 nm in thickness, and several millimeters in length, with high purity and yield. This work not only validated the feasibility of the “glycerol– NaOH –sulfur source” system, but also confirmed *via* HRTEM that nanobelts grow along [210] with side facets exposing (220) and (120) planes, clarifying the critical roles of glycerol coordination and NaOH concentration in dimension and facet control and providing essential theoretical foundations for subsequent Bi_2S_3 dimensional engineering and selective facet growth. As high specific surface areas and well-defined interfaces are beneficial for boosting the photoactivity, researchers have turned their attention to three-dimensional flower-ball structures self-assembled from two-dimensional nanosheets. For instance, Yang *et al.*⁴⁴ employed solvothermal self-assembly followed by wet impregnation–annealing method to prepare 3D flower-like CoO using $\text{Co}(\text{NO}_3)_2 \cdot 6\text{H}_2\text{O}$ as the cobalt precursor, and the wire-like micro-petals of CoO serve as an excellent growth substrate for Bi_2S_3 . After wet impregnation and annealing, Bi_2S_3 nanosheets epitaxially grow on the CoO micro-petal surface, forming 3D chrysanthemum-like Bi_2S_3 @ CoO heterojunction arrays with an average size of $\sim 10.73 \mu\text{m}$ (Fig. 4b). The Bi_2S_3 nanosheets are ~ 10 nm thick and form a stable heterointerface with the CoO (111) plane. This

hierarchical structure combines high specific surface area, multiple light reflection/scattering channels, and optimized molecular diffusion kinetics, providing a structural foundation for efficient separation and migration of photogenerated charges in Z-scheme heterojunctions, thereby enhancing photocatalytic oxidation/reduction performance. Sang *et al.*⁴⁵ proposed a pre-oxidation followed by *in situ* sulfidation one-step hydrothermal strategy. $\text{Bi}(\text{NO}_3)_3 \cdot 5\text{H}_2\text{O}$ was dissolved in a DMF solution containing nitric acid, then mixed with an aqueous thiourea solution and transferred to an autoclave for reaction at 100 °C for 12 h. Under acidic conditions, thiourea slowly hydrolyzes to release S^{2-} , which first reacts with Bi^{3+} to form a Bi_2O_3 nanosheet framework, followed by *in situ* sulfidation to yield $\text{Bi}_2\text{O}_3/\text{Bi}_2\text{S}_3$ p–n heterojunction flower-balls. The structure retains intimate contact between the Bi_2O_3 (111) and Bi_2S_3 (101) planes, establishing a built-in electric field that markedly suppresses photogenerated carrier recombination. Under visible light, 99.7% RhB is removed and 91.8% Cr(vi) is reduced within 90 min, and this outstanding performance stems from the synergistic effect of charge separation by the p–n heterojunction and the bifunctional catalytic sites. Recently, Wang *et al.*⁴⁶ synthesized a Bi_2S_3 – In_2S_3 heterostructure *via* a one-step hydrothermal route at 200 °C for 24 h, achieving face-to-face coupling between the Bi_2S_3 (060) and In_2S_3 (440) planes. In this architecture, Bi_2S_3 exists as nanorods (~ 200 nm long, ~ 20 nm in diameter) and In_2S_3 as nanoparticles (~ 25 nm). The core of this facet coupling lies in the matching atomic spacing between the two phases, providing a robust interface for charge transfer. This face-to-face coupling not only shortens carrier diffusion distances but also delivers 100% Cr(vi) photoreduction within 30 min, which is about 44 times higher than bare Bi_2S_3 , demonstrating a novel concept combining facet engineering with Z-scheme heterojunction optimization, and directly confirming the advantage of facet-to-facet coupling, shortening carrier diffusion distance while preserving highly active crystal planes.

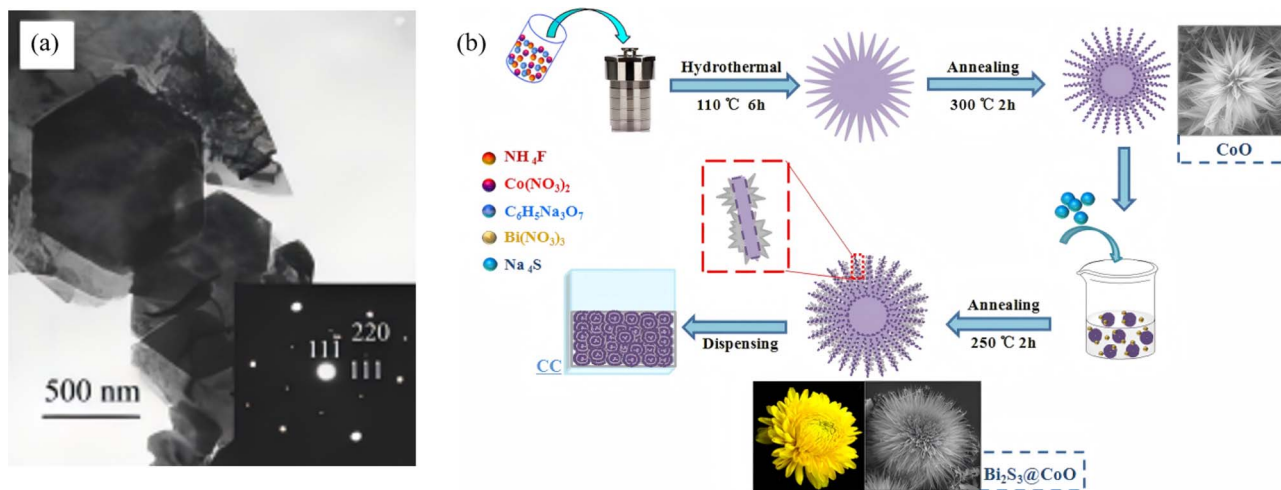


Fig. 4 (a) TEM images of Bi_2S_3 obtained by solvothermal treatment at 160 °C for 48 h. Inset: ED patterns of the particles.⁴³ Copyright 2003, Wiley-Blackwell. (b) Schematic illustration of the preparation process of 3D CoO and Bi_2S_3 @ CoO chrysanthemums-like arrays.⁴⁴ Copyright 2019, Elsevier.



From 1D single-crystalline nanobelts to 3D facet-coupled heteroflowers, hydrothermal/solvothermal methods exploit a three-parameter (solvent-ligand-temperature) coupling to achieve hierarchical control of dimension, facet, and band structure within a single reaction system. All products retain the intrinsic orthorhombic lattice of Bi_2S_3 while exposing different high-activity facets, offering a rich structural platform for subsequent photo and electro-catalytic optimization.

3.1.2. Hot-injection method. The hot-injection (HI) technique is the cornerstone for producing monodisperse and highly crystalline Bi_2S_3 nanocrystals. By separating nucleation (high-temperature, seconds) from growth (lower-temperature, minutes), HI achieves temporal-spatial decoupling that yields quantum dots or nanorods with narrow size distribution and uniform morphology. As early as 2010, Wu *et al.*⁴⁷ pioneered a hot-injection route to Bi_2S_3 nanostructures, wherein BiCl_3 was dissolved in oleylamine at 150 °C, followed by rapid injection of a thioacetamide-oleylamine solution and heating to 180 °C for 5–10 min, yielding orthorhombic single-crystal nanorods (Fig. 5). The work confirmed that intrinsic chain-like growth along [001] drives the one-dimensional morphology. The resulting nanodots exhibited excellent visible-light photocatalytic activity due to their high specific surface area, efficiently degrading organic dyes such as RhB. To address the issues of poor mixing in dual-solution systems and poor batch-to-batch reproducibility, Saah *et al.*⁴⁸ proposed a single-source-precursor-mediated hot-injection strategy, preparing high-purity orthorhombic Bi_2S_3 nanorods within 30 min. By co-injecting lead piperidine dithiocarbamate precursors, continuous synthesis of $\text{Pb}_x\text{Bi}_{(1-x)}\text{S}$ alloy nanomaterials (Bi doping 0–100%) was achieved, with morphology evolving from cubic (low Bi, $\leq 50\%$) to rod-like (high Bi, $\geq 80\%$). The band gap tunes linearly from 0.72 eV (PbS) to 1.94 eV (Bi_2S_3). This single-source hot-injection method offers high atom economy (90–100% utilization), high product purity, and controllable morphology,

providing high-performance model materials for optoelectronic devices and photovoltaics.

In summary, hot injection, based on millisecond supersaturation and second-scale nucleation, coupled with rational precursor design and the three-lever control strategy, enables continuous tuning of size, shape and hetero-interfaces of Bi_2S_3 nanocrystals. Its excellent reproducibility, high yield and straightforward scalability have made HI one of the preferred routes for both laboratory research and commercial production of high-quality Bi_2S_3 nanomaterials.

3.1.3. Ion-exchange strategy. Ion exchange, occurring at solid-liquid or solid-solid interfaces under ambient conditions, offers a mild, low-energy post-synthetic pathway for precisely tailoring Bi_2S_3 -based heterojunctions. A highly reactive parent framework is first prepared, and subsequent selective replacement of anions (or cations) by S^{2-} and Bi^{3+} then produces an intimately bonded heterostructure in which band alignment and defect passivation are achieved simultaneously. Lu *et al.*⁴⁹ employed hollow spherical BiOCl as a parent material and reacted it with thioacetamide (TAA) solution at room temperature. The hydrolysis of TAA releases S^{2-} ions that selectively replace Cl^- in BiOCl , generating Bi_2S_3 nanoparticles *in situ* on the BiOCl surface to form a $\text{BiOCl}/\text{Bi}_2\text{S}_3$ heterojunction (Fig. 6). XRD, XPS, SEM and TEM characterization confirmed that the composite fully retains the hollow spherical morphology of the BiOCl parent, with Bi_2S_3 nanoparticles uniformly dispersed on the surface. The Bi_2S_3 loading can be tuned by adjusting the ion-exchange reaction time. The resulting composite exhibits excellent Cr^{6+} reduction performance under visible light. The optimal sample $\text{BiOCl}/\text{Bi}_2\text{S}_3$ -4h achieves a reduction rate constant of 0.400 min^{-1} , completely reducing Cr^{6+} within 9 min, which is about 31 times higher than pure BiOCl . This anion-exchange strategy enables efficient heterointerface construction, providing a reference for the preparation of narrow-band-gap coupled photocatalytic systems. Huang *et al.*⁵⁰ first synthesized CdS nanorods *via* solvothermal route, then

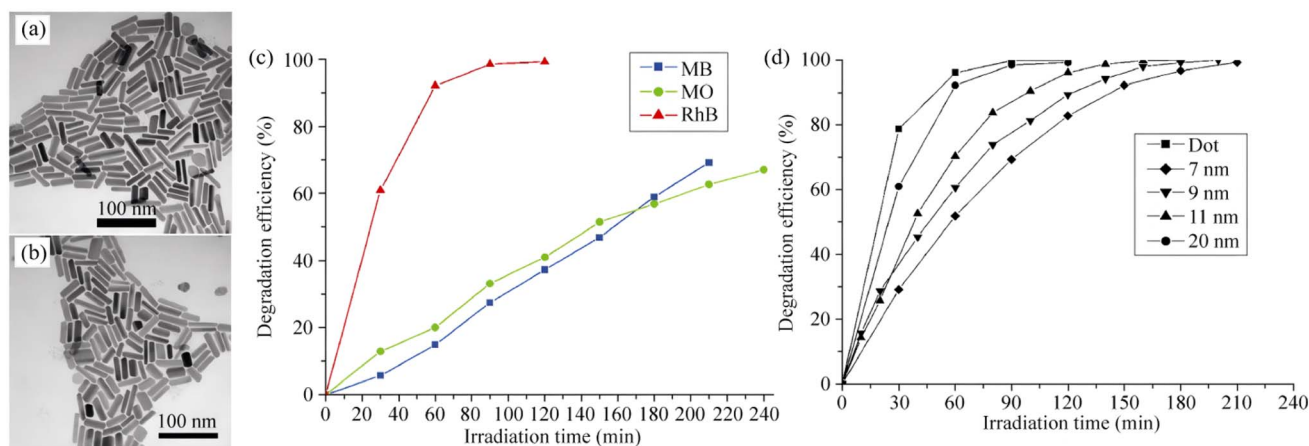


Fig. 5 (a) TEM image of Bi_2S_3 nanocrystals prepared with a Bi/S ratio of 1 : 1.5 and Bi precursor concentrations of 0.025 mol L^{-1} . (b) TEM images of Bi_2S_3 nanocrystals prepared with a Bi precursor concentration of 0.025 mol L^{-1} with Bi/S molar ratios of 1 : 1.5. (c) Photodegradation efficiency of Bi_2S_3 nanorods (prepared with a Bi source concentration of 0.025 mol L^{-1} , Bi : S = 2 : 3) with MO, MB, and RhB. (d) Efficiency of Bi_2S_3 nanodots and nanorods with different diameters on the photodegradation of RhB.⁴⁷ Copyright 2010, Tsinghua University Press.



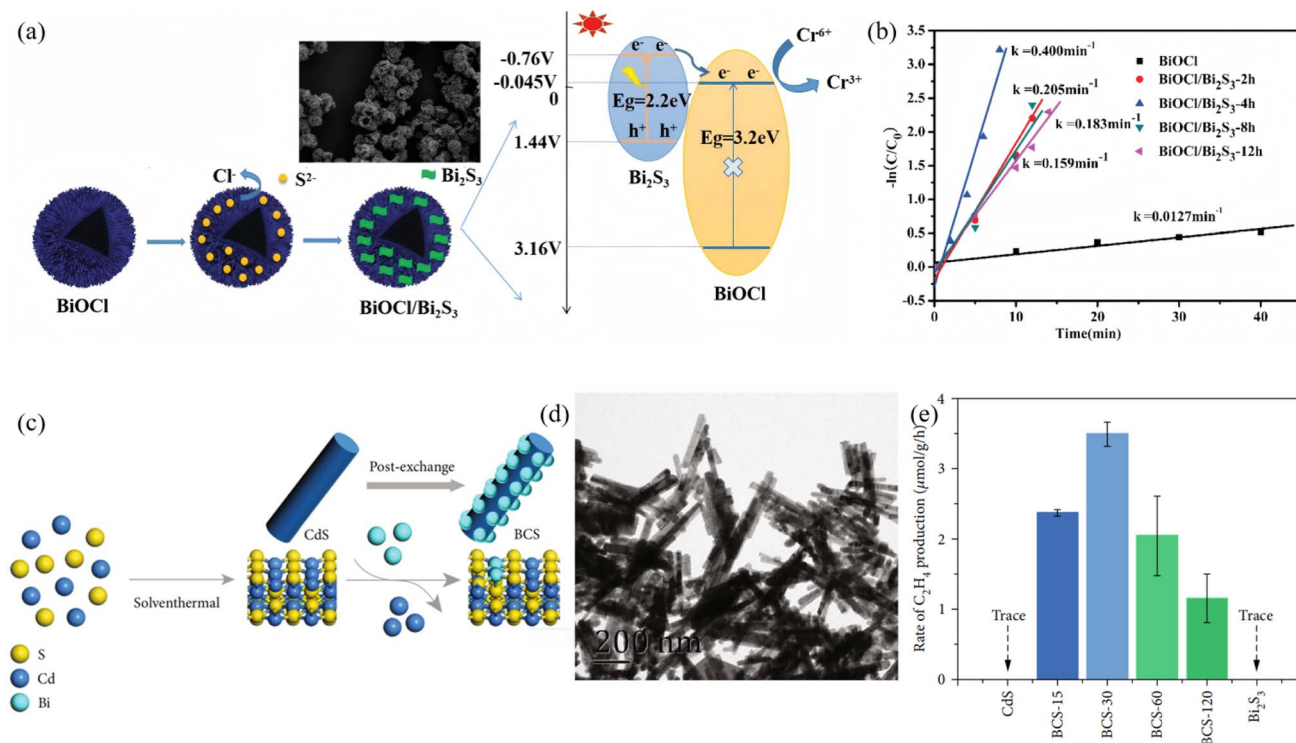


Fig. 6 (a) Synthesis process and SEM images of hollow spherical BiOCl/Bi₂S₃, and photocatalytic mechanism of BiOCl/Bi₂S₃. (b) Plots of $\ln(C/C_0)$ versus time for Cr⁶⁺ reduction over different catalysts.⁴⁹ Copyright 2020, Elsevier. (c) Schematic illustration of the synthetic process of BCS-*t* composite. (d) TEM image of the BCS-30. (e) The yield of C₂H₄ from CdS, Bi₂S₃, and BCS-*t* under visible light irradiation.⁵⁰ Copyright 2022, AMER ASSOC ADVANCEMENT SCIENCE.

used Bi³⁺-oleate complex as an exchange agent to exploit the much lower solubility product of Bi₂S₃ ($K_{sp} \approx 1 \times 10^{-97}$) compared to CdS ($K_{sp} \approx 8 \times 10^{-27}$), partially replacing Cd²⁺ with Bi³⁺ to disperse Bi₂S₃ nanoparticles *in situ* on CdS, forming a Bi₂S₃/CdS heterojunction. Mott-Schottky analysis confirmed that both CdS and Bi₂S₃ are n-type semiconductors, forming a Z-scheme band alignment. This core-shell cascade energy-level strategy drives photogenerated electrons from the Bi₂S₃ conduction band to the CdS conduction band, enhancing charge separation efficiency while preserving strong redox capability and resulting in significantly improved selectivity for CO₂ reduction to C₂H₄ far beyond single components. Furthermore, this bidirectional exchange strategy has been extended to multidimensional structures. Xu *et al.*⁵¹ immersed pre-hydrothermally synthesized 2-D Bi₂WO₆ nanosheets (BWO) in a TAA solution, the hydrolysis of TAA releases S²⁻ that selectively replaces interlayer O²⁻ in Bi₂WO₆, generating Bi₂S₃ nanodots *in situ* on the nanosheet surface to form a Bi₂S₃/2D-Bi₂WO₆ type-II heterojunction. The 2D sheet morphology of Bi₂WO₆ is preserved, while Bi₂S₃ decoration introduces surface oxygen vacancies and promotes charge separation, effectively lowering charge recombination. Consequently, the composite exhibits a markedly higher visible-light-driven photodegradation rate constant for RhB than pure Bi₂WO₆, with sample BWS-2 showing the optimal activity.

Overall, ion exchange enables controlled fabrication of Bi₂S₃ heterojunctions at low temperature and ambient pressure. The

exchange depth can be tuned continuously from nanodot, thin shell, to core/shell, while the interfacial defect density remains low. These attributes make ion exchange an indispensable post-synthetic tool for constructing high-efficiency photocatalytic systems.

3.1.4. Microwave-assisted method. In recent years, microwave (MW) irradiation has emerged as a promising route for the rapid and energy-efficient fabrication of nanostructured materials. Instantaneous volumetric heating generated by dipolar polarization and ionic conduction enables nucleation and crystallization to be completed within minutes, which conventionally require hours under solvothermal conditions, thereby offering a green alternative for tailoring Bi₂S₃ nanoarchitectures. The evolution of MW-assisted Bi₂S₃ synthesis can be summarized as a dot-wire-flower sequence, while simultaneously demonstrating the tunability of facet exposure and defect density under the microwave field. As early as 2008, Li *et al.*⁵² reported a one-step MW-solvothermal protocol. In this scenario, Bi(NO₃)₃·5H₂O and Na₂S·5H₂O were reacted under MW irradiation, producing single-crystalline nanowires 20 nm in diameter and tens of micrometres in length (yield >95%) (Fig. 7). Compared with conventional solvothermal methods, microwave-assisted heating offers rapid volumetric heating, fast reaction rates, short processing time, high selectivity and energy efficiency, enabling highly efficient anisotropic growth of Bi₂S₃ in an extremely short period. This study not only provides a novel route for rapid preparation of Bi₂S₃ nanomaterials, but



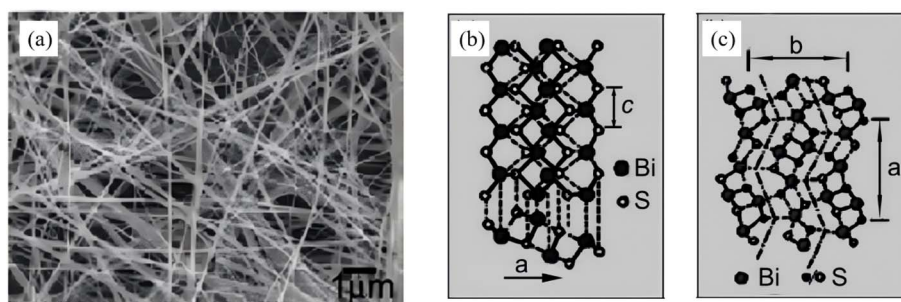


Fig. 7 (a) SEM image of the obtained nanowires. (b and c) Schematic structures of the chain-type Bi_2S_3 .⁵² Copyright 2008, Elsevier.

also establishes an important methodological foundation for precise dimensional control of nanomaterials through the tunable microwave power feature. Subsequently, Godzier *et al.*⁵³ employed microwave-assisted synthesis to fabricate flower-like 3D microrods assembled from nanorods. The rapid and uniform heating of the microwave field drastically shortens reaction time while enabling controlled nucleation and growth of Bi_2S_3 crystals, effectively regulating the aspect ratio and dispersity of the particles. This result validates the pronounced advantages of the microwave method in tailoring Bi_2S_3 morphology and enhancing carrier transport efficiency, which originate from the smaller microrod diameter and higher aspect ratio.

By coupling three operational parameters including power, time and solvent polarity, the MW-assisted approach can accomplish a controllable 1D nanowire and 3D microflower transformation within 10–20 min. Volumetric heating suppresses local overheating and defect aggregation, yielding highly crystalline products with tunable facet exposure. Consequently, microwave synthesis has become a green and scalable alternative for rapidly preparing high-performance Bi_2S_3 nanostructures for photocatalytic applications.

3.1.5. Template-directed synthesis. The template approach follows a shape-first and sulphidation-second philosophy, in which a removable hard or soft scaffold is erected, and Bi and S precursors are then infiltrated, and ultimately Bi_2S_3 is nucleated within the confined space, thereby dictating macro-/meso-

scopic morphology and preferential facet exposure. Methodological evolution proceeds through three stages including hard, soft and synergistic process which sequentially solve the challenges of shape replication, interfacial coupling and band alignment. Dai *et al.*⁵⁴ employed rod-like Bi-based MOF CAU-17 as both sacrificial template and Bi source to construct, in one pot, a hierarchical C- Bi_2S_3 /ZnIn₂S₄ heterojunction in which ZnIn₂S₄ nanosheets decorate the MOF-derived Bi_2S_3 framework (Fig. 8). Benefiting from the inherited CAU-17 architecture, C- Bi_2S_3 possesses a high specific surface area of 179 m² g⁻¹ (>13 times that of ordinary solvothermal O- Bi_2S_3) and abundant mesopores. During the single-step synthesis sulfur acts as a “bridge”, creating intimate inter-layer contact between ZnIn₂S₄ and C- Bi_2S_3 , suppressing nanosheet aggregation and exposing more active sites. Under visible light and ambient air the composite delivers 1178–1324 μmol L⁻¹ H₂O₂ while degrading >95% of pollutants and markedly lowering chemical oxygen demand (COD). This work first demonstrates that a Bi-MOF hard template can simultaneously tailor morphology and porosity of Bi_2S_3 -based heterojunctions through structural inheritance and growth confinement, offering a new paradigm for photocatalysts that balance active-site exposure and carrier transport. Mi *et al.*⁵⁵ employed bismuth salicylate (BiSSA) as a hard template and synthesized 1-D Bi_2S_3 /Bi₄O₅Br₂ S-scheme hierarchical microbundles *via* a simple one-pot solvothermal route. The method achieves uniform dispersion of Bi_2S_3 nanoparticles throughout the Bi₄O₅Br₂ matrix, greatly enlarging the

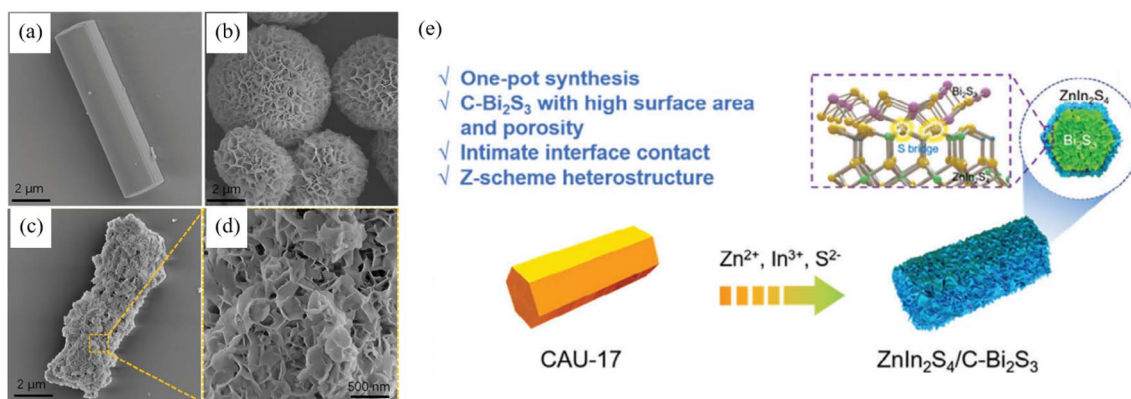


Fig. 8 SEM images of (a) CAU-17, (b) ZnIn₂S₄ and (c and d) ZCB-1. (e) Creative synthetic method of ZnIn₂S₄/Bi₂S₃ hybrids.⁵⁴ Copyright 2024, Wiley-VCH Verlag.



heterojunction interface. HRTEM image confirms atomic-scale face-to-face coupling between the Bi_2S_3 (211) and $\text{Bi}_4\text{O}_5\text{Br}_2$ (402) planes. This lattice-matching effect, synergistic with band-structure modulation, accelerates charge separation and migration. Under visible light the microbundles degrade 98% of RhB within 30 min, with a rate constant 3.2 times that of bare $\text{Bi}_4\text{O}_5\text{Br}_2$ and 137 times that of bare Bi_2S_3 , far outperforming a conventional surface-supported heterojunction (Ss). The work highlights the unique advantage of hard-template strategies in simultaneously realizing precise facet coupling and band alignment for superior photocatalytic performance.

By combining hard scaffolds for shape confinement and soft interfaces for facet registration, the template route enables low-temperature, ambient-pressure customization of Bi_2S_3 thickness, crystal facet and pore structure within a single protocol. The removable nature of the templates eliminates surface-ligand residues and furnishing clean as well as highly active interfaces. Consequently, template-directed synthesis has become a general and powerful strategy for constructing sophisticated Bi_2S_3 -based heterojunctions tailored to photocatalytic applications.

3.2. Morphology–property relationships

3.2.1. Zero-dimensional nanoparticles. Zero-dimensional Bi_2S_3 nanocrystals (≤ 10 nm) serve as an ideal model for high-efficiency photocatalysis because of complete exciton confinement, ultra-high surface area and size-tunable band gaps.

Establishing their morphology–performance paradigm follows a size–band gap–interface hierarchy. For example, monodisperse quantum dots (QDs) are first obtained *via* mild solution or ultrasonic routes; surface coupling or *in situ* deposition then builds interfacial electric fields; finally, size-dependent carrier separation is quantified. Uddin *et al.*⁵⁶ used soluble starch $[(\text{C}_6\text{H}_{10}\text{O}_5)_n]$ as both stabilizer and capping agent to synthesize Bi_2S_3 nanoparticles (NPs) *via* a one-pot aqueous route. $\text{Bi}(\text{NO}_3)_3 \cdot 5\text{H}_2\text{O}$ and Na_2S served as Bi and S sources, respectively, and the reaction was conducted stepwise at $70\text{--}90^\circ\text{C}$. Hydroxyl groups of the starch coordinate with Bi^{3+} , which caps the growing nuclei and suppresses aggregation, yielding monodisperse quasi-spherical Bi_2S_3 NPs with an average diameter of ~ 11 nm (7–15 nm range) and excellent colloidal stability. UV-vis spectroscopy reveals a strong excitonic shoulder at 310 nm, based on which Tauc analysis gives a band gap of 2.86 eV, a pronounced blue-shift relative to bulk Bi_2S_3 (1.3 eV), confirming that quantum-confinement-induced discrete energy levels dominate the size-dependent optical properties. Li *et al.*⁵⁷ developed a facile one-step solvothermal route in which $\text{Bi}(\text{NO}_3)_3$ and $\text{Na}_2\text{S}_2\text{O}_3$ serve as Bi and S sources, respectively, in ethylene glycol (Fig. 9). Under these conditions, zero-dimensional Bi_2S_3 nanoparticles (~ 10 nm) are grown *in situ* onto $g\text{-C}_3\text{N}_4$ nanosheets, yielding a 0D/2D $\text{Bi}_2\text{S}_3/g\text{-C}_3\text{N}_4$ heterojunction. TEM image confirms the uniform dispersion of the quantum dots across the nanosheet support. Band alignment ($g\text{-C}_3\text{N}_4$: $E_g = 2.71$ eV, CB = -1.13 eV, VB = 1.57 eV; Bi_2S_3 : $E_g =$

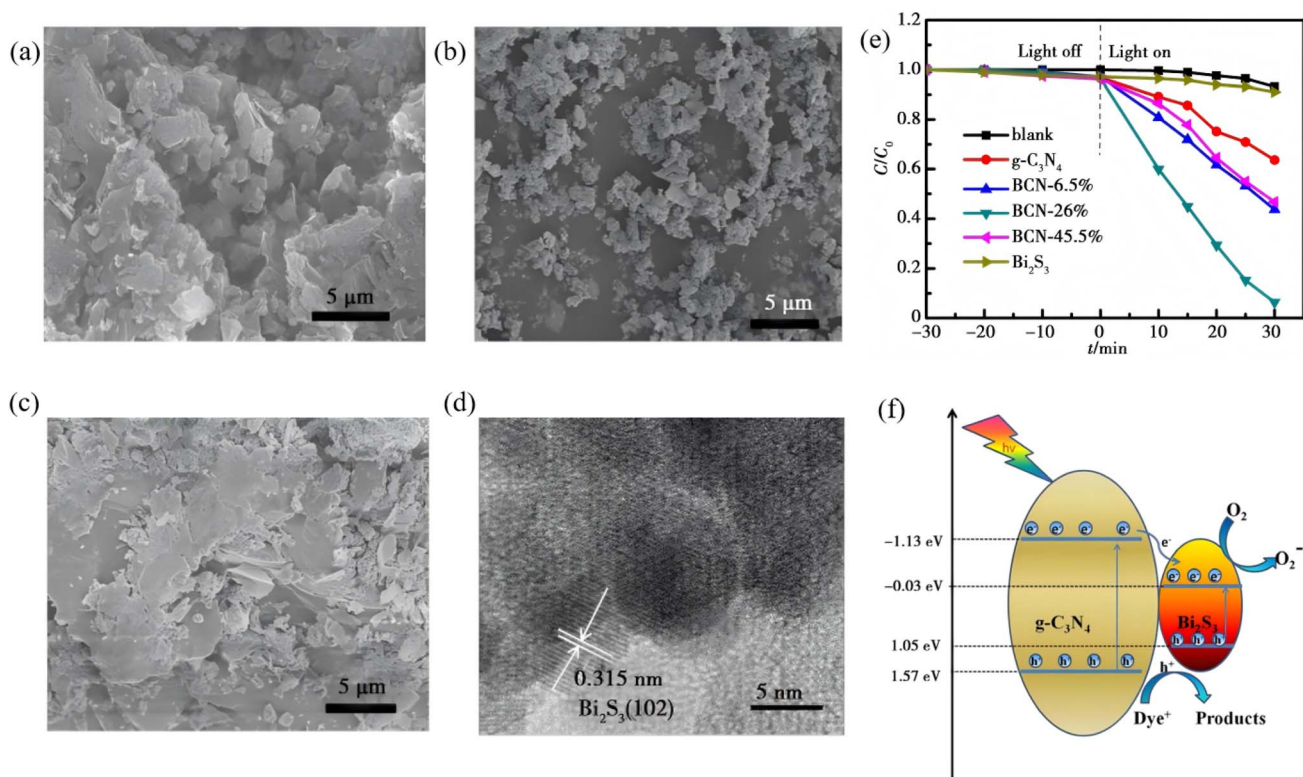


Fig. 9 SEM images of (a) pure $g\text{-C}_3\text{N}_4$, (b) Bi_2S_3 , (c) BCN-26%. (d) HRTEM images of BCN-26%. (e) Degradation curves of RhB under visible light irradiation using pure $g\text{-C}_3\text{N}_4$, Bi_2S_3 , and $\text{Bi}_2\text{S}_3/g\text{-C}_3\text{N}_4$ heterojunction (f) Schematic illustration of photocatalytic mechanism of $\text{Bi}_2\text{S}_3/g\text{-C}_3\text{N}_4$ heterojunction under visible light irradiation.⁵⁷ Copyright 2020, Chongqing Southwest Information Co., Ltd.



1.24 eV, CB = 1.05 eV, VB = -0.33 eV) drives photogenerated electrons from the $g\text{-C}_3\text{N}_4$ conduction band into the Bi_2S_3 conduction band, suppressing charge recombination and prolonging carrier lifetime. The thus-prepared composite demonstrates the extended visible-light absorption, and the 26 wt% $\text{Bi}_2\text{S}_3/g\text{-C}_3\text{N}_4$ sample exhibits the highest activity, which is remarkably larger than bare $g\text{-C}_3\text{N}_4$ while retaining stable performance over five cycles. This study not only validates the direct benefit of size-controlled 0D Bi_2S_3 quantum dots but also provides a universal framework for designing quantum-dot-based heterojunctions with optimized photocatalytic performance.

3.2.2. One-dimensional nanostructures. One-dimensional (1-D) Bi_2S_3 nanorods/nanowires are regarded as ideal platforms for accelerating photogenerated charge separation because they combine directional charge transport channels, high specific surface area and facet-selective exposure. Establishing their structure–performance paradigm follows a diameter–facet–interface strategy. First, intrinsic extension along [001] is achieved *via* solvothermal or microwave routes. Second, radial size is tuned to optimize band-edge positions. Finally, core–shell or epitaxial heterointerfaces are introduced to realize synergistic photocatalytic and photoelectrochemical enhancement. Liu *et al.*⁵⁸ reported in 2016 a facile two-step hydrothermal-plus-annealing route to grow a novel Bi_2S_3 -nanowire@ TiO_2 -nanorod (Bi_2S_3 NWs@ TiO_2 NRs) architecture directly on FTO glass (Fig. 10). Rather than coating Bi_2S_3 with TiO_2 , they used a pre-formed TiO_2 nanorod array as the scaffold

and grafted Bi_2S_3 nanowires onto its surface. Because the Bi_2S_3 conduction-band edge lies above that of TiO_2 , photogenerated electrons are readily injected from Bi_2S_3 into TiO_2 and then conducted along the nanorods to the FTO substrate, while holes remain confined within the Bi_2S_3 nanowires, markedly suppressing the charge recombination. Serving as a photoanode, this heterostructure delivers a visible-light-responsive H_2 -evolution rate of $35.97 \mu\text{mol cm}^{-2} \text{h}^{-1}$, outperforming previously reported $\text{Bi}_2\text{S}_3/\text{TiO}_2$ core–shell nanorods. The work underscores the synergistic benefit of 1D/1D heterostructure for light-to-electricity conversion and offers a surfactant-/template-free route that relies solely on the intrinsic anisotropic growth of Bi_2S_3 , providing a fresh concept for designing new hetero-nanostructures. Arumugam *et al.*⁵⁹ employed a reflux approach using $\text{Bi}(\text{NO}_3)_3$ and thiourea as precursors in DMF, with CTAB as surfactant, to controllably synthesize orthorhombic Bi_2S_3 nanorods at 180 °C. By tuning reaction time (1–4 h), they established a clear size–morphology–property relationship. After 3 h, uniform 1D rods ~ 233 nm in diameter and $>1 \mu\text{m}$ long with optimal crystallinity were obtained, and extending to 4 h caused deformation and shrinkage (diameter down to 140 nm). Optical measurements revealed a pronounced quantum-size effect, that is, the 75 nm rods (1 h) exhibited a 1.91 eV band gap, whereas the 233 nm rods (3 h) showed 1.81 eV. The high-aspect-ratio single-crystal architecture, preferentially grown along (130), enhances carrier mobility and yields high dielectric constant and low loss at low frequency *via* combined interface/orientation polarization. This work not only

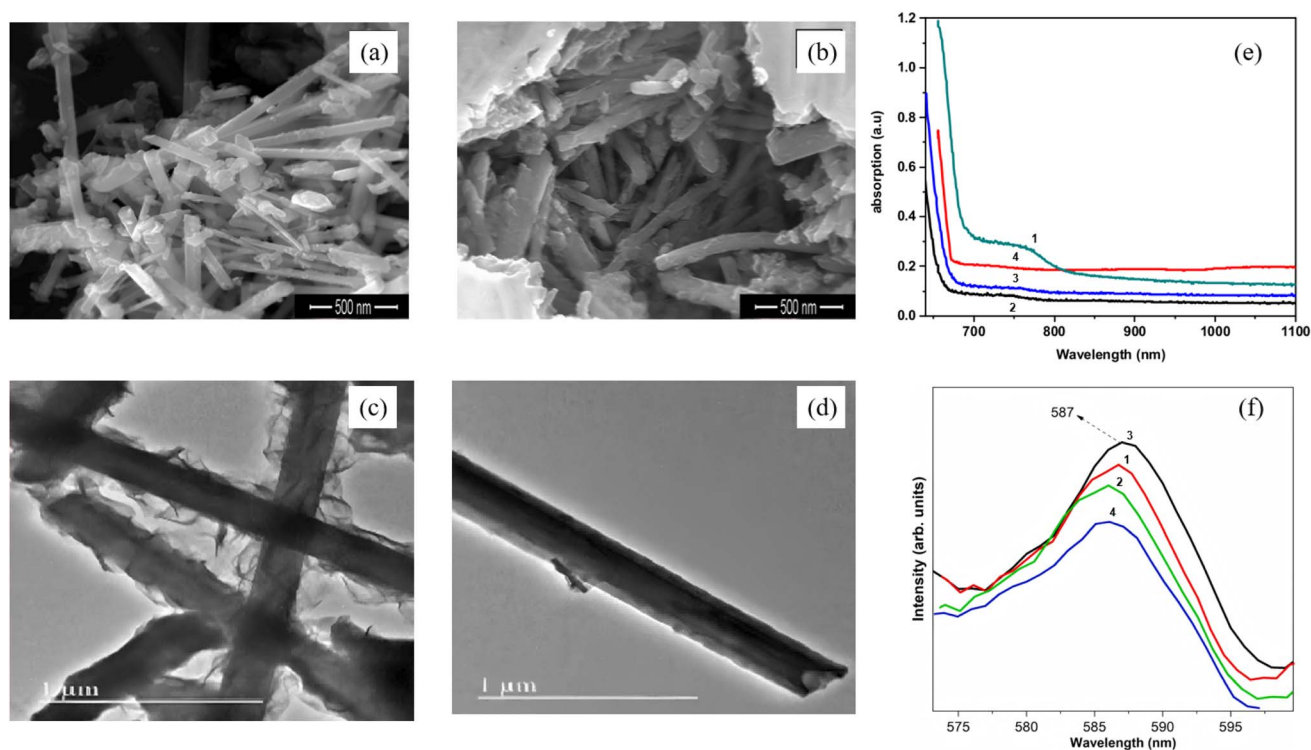


Fig. 10 SEM image of Bi_2S_3 nanorods prepared with different reaction time (a) 3 h, (b) 4 h. TEM image of Bi_2S_3 nanorods prepared with different reaction time (c) 2 h; (d) 3 h. (e) UV-vis spectrum of Bi_2S_3 nanorods prepared with different reaction time, (f) Photoluminescence spectra of Bi_2S_3 nanorods prepared with different reaction time. (1–4) 1 h, 2 h, 3 h, 4 h.⁵⁹ Copyright 2022, Elsevier BV.



maps out size-dependent performance rules for 1D Bi_2S_3 nanorods but also provides a universal materials-design paradigm for optimizing their use in photocatalysis and photoelectrochemistry.

3.2.3. Two-dimensional nanosheets. Two-dimensional Bi_2S_3 nanosheets, which feature atomic thickness, large-area exposure of active facets and tunable in-plane anisotropy, are regarded as an ideal platform for achieving efficient photogenerated charge separation and accelerated surface-reaction kinetics. Single- or few-layer structures are first obtained *via* confined growth or exfoliation, after which defects or lattice strain are introduced to tailor the band-edge positions. Finally, in-plane heterojunctions or defect sites are constructed to realize synergistic enhancements in photocatalytic performance. Messalea *et al.*⁶⁰ developed a liquid-metal-based two-step synthesis method to overcome the difficulty of large-area growth of anisotropic Bi_2S_3 crystals. First, molten-bismuth surface-limited oxidation and exfoliation on SiO_2/Si or glass substrates produced wafer-scale Bi_2O_3 nanosheets which were then sulfurized at <450 °C in a tube furnace with elemental sulfur to yield millimetre-scale and high-quality single-crystal Bi_2S_3 nanosheets with 1–3 nm thick (typically 2.5 nm) (Fig. 11). The sheets possess an orthorhombic lattice with (210) preferred orientation and pronounced in-plane anisotropy verified by polarized Raman spectroscopy. The few-layer Bi_2S_3 is a p-type semiconductor with a direct band gap of ~ 2.3 eV and a maximum hole mobility of $28 \text{ cm}^2 \text{ V}^{-1} \text{ s}^{-1}$, providing an

excellent material and structural platform for high-performance 2D optoelectronics. Li *et al.*⁶¹ devised a one-step vapor-phase sulfidation with synchronous defect creation protocol wherein high-temperature sulfur vapor reacts with Bi_2O_3 , while SO_2 released during the process breaks surface lattice bonds to generate abundant defects, yielding defect-rich 2D Bi_2S_3 nanosheets (NSs). These defective NSs undergo dynamic reconstruction into a 2D metallic Bi phase that simultaneously hosts sulfur dopants and lattice defects (Fig. 12). The work demonstrates that cooperative defect engineering and hetero-atom doping can modulate both proton supply and intermediate stabilization, offering a general design paradigm for optimizing 2D Bi-based catalysts.

3.2.4. Three-dimensional hierarchical architectures. Three-dimensional Bi_2S_3 nanoflowers, self-assembled from 2D nanosheets, combine a high specific surface area, abundantly exposed facets, and hierarchical porosity, simultaneously enhancing light harvesting, mass transfer, and active-site utilization. First, nanosheet self-assembly is achieved *via* a one-step hydrothermal route. Then, *in situ* sulfidation or hetero-epitaxy introduces a built-in electric field, ultimately constructing p-n or Z-scheme architectures that spatially separate oxidation and reduction reactions. Sang *et al.*⁴⁵ employed $\text{Bi}(\text{NO}_3)_3 \cdot 5\text{H}_2\text{O}$ and thiourea as precursors to fabricate 1–2 μm $\text{Bi}_2\text{O}_3/\text{Bi}_2\text{S}_3$ nanoflowers self-assembled from nanosheets decorated with sparse nanorods *via* a one-step hydrothermal route, generating an inter-sheet mesoporous network (Fig. 13). The intimate contact

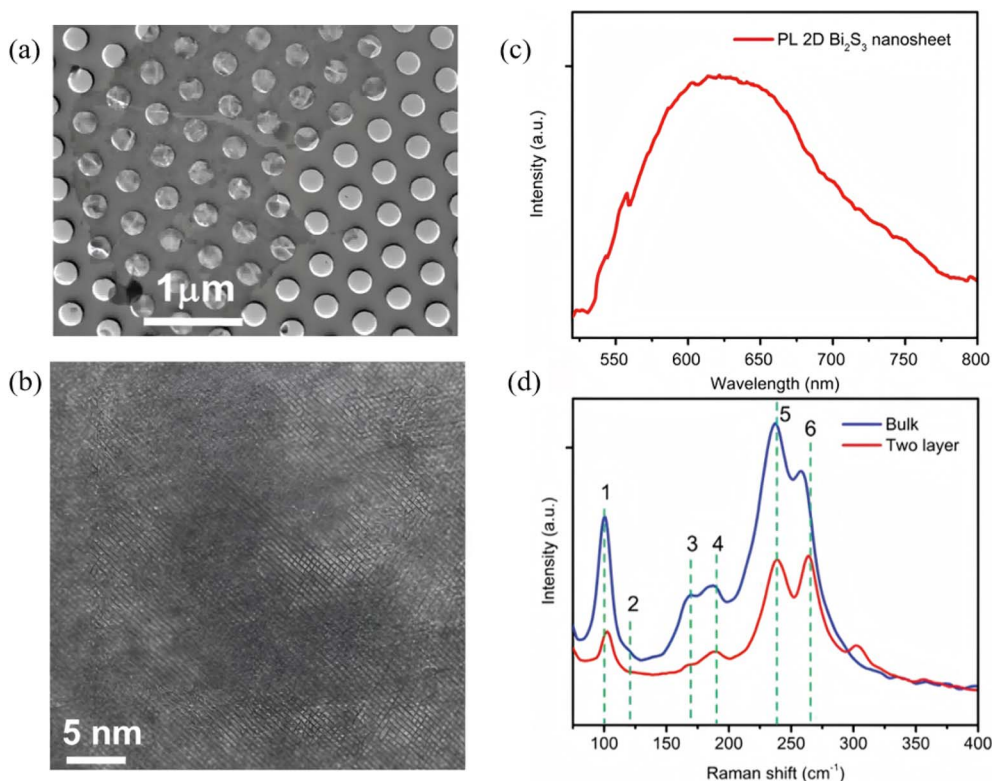


Fig. 11 (a) TEM image of Bi_2S_3 nanosheet, (b) HRTEM image of Bi_2S_3 nanosheet, (c) PL spectrum of a bilayer Bi_2S_3 nanosheet, and (d) Raman spectrum of bulk Bi_2S_3 (blue line) and 2D nanosheets (red line).⁶⁰ Copyright 2020, John Wiley and Sons Ltd.



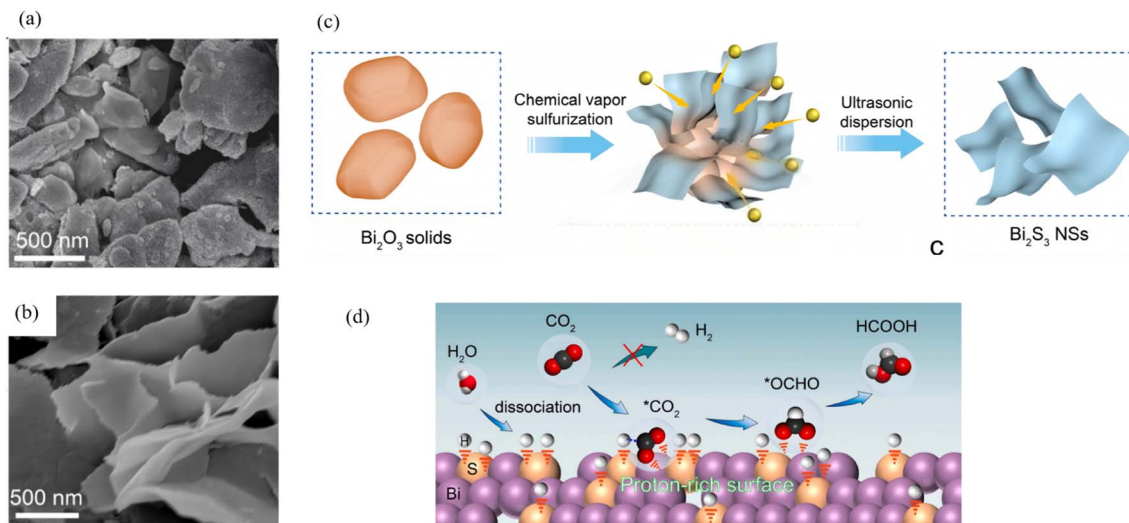


Fig. 12 (a and b) SEM images of bulk Bi_2O_3 and Bi_2S_3 NSs. (c) Schematic illustration of the chemical vapor sulfurization process for the conversion of bulk Bi_2O_3 to 2D Bi_2S_3 NSs. (d) The proposed reaction mechanism for CO_2 RR over 2D-Bi with proton-rich surface to stabilize $^*\text{OCHO}$ for CO_2 reduction to formate.⁶¹ Copyright 2024, Elsevier.

between p-type Bi_2S_3 and n-type Bi_2O_3 creates a built-in electric field across the p-n heterojunction. Under visible light, 99.72% of RhB is removed and >91.8% of $\text{Cr}(\text{vi})$ is reduced within 90 min, demonstrating that the hierarchical nanoflower simultaneously enhances pollutant adsorption and redox bi-functionality. Photogenerated holes are the main active species for RhB degradation, while photogenerated electrons dominate $\text{Cr}(\text{vi})$ reduction. Zhou *et al.*⁶² employed a sol-gel route coupled

with *in situ* growth to fabricate $\text{Bi}_2\text{S}_3/\text{BiFeO}_3$ nanoflower heterojunctions. Using $\text{Bi}(\text{NO}_3)_3 \cdot 5\text{H}_2\text{O}$ and $\text{Fe}(\text{NO}_3)_3 \cdot 9\text{H}_2\text{O}$ as BiFeO_3 precursors and L-cysteine as the sulfur source, Bi_2S_3 was grown directly on the BiFeO_3 scaffold. The narrow band gap of ferroelectric BiFeO_3 and the staggered alignment with Bi_2S_3 produce a Type-II heterojunction whose built-in field drives spatial charge separation, in which electrons migrate from the Bi_2S_3 conduction band to the BiFeO_3 conduction band, while

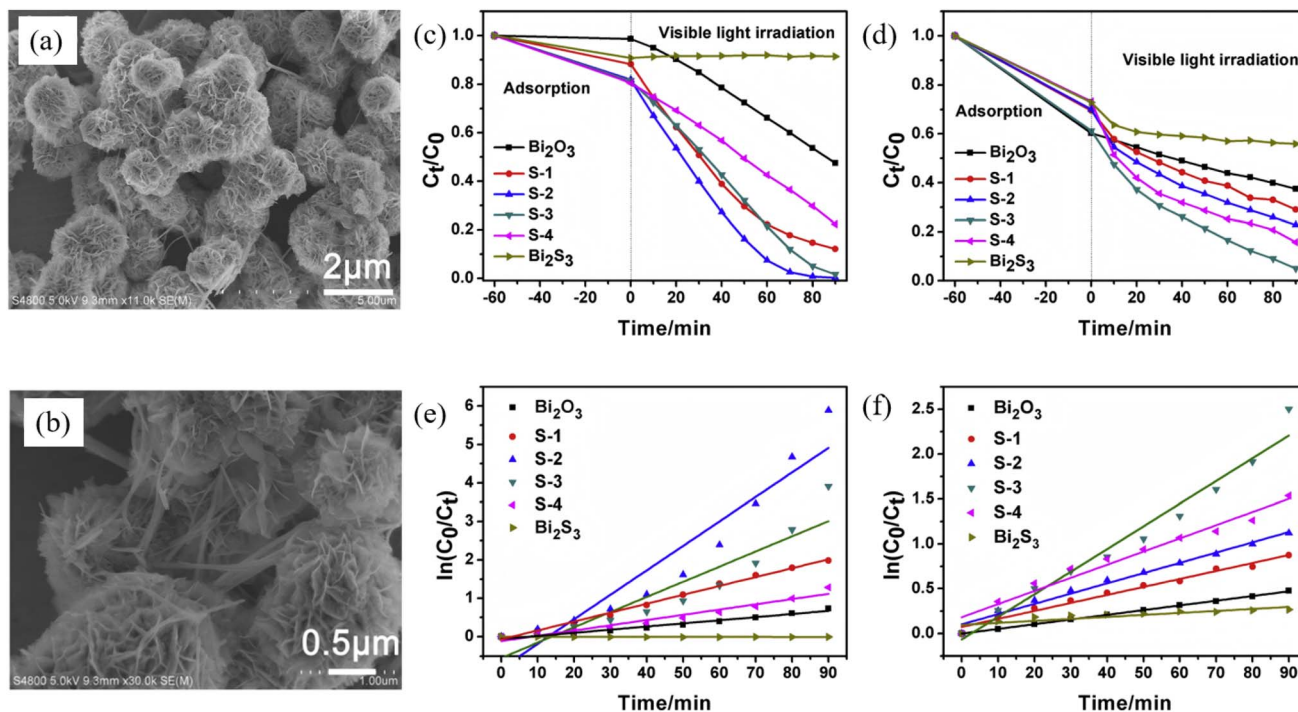


Fig. 13 (a and b) SEM images of samples S-3. Photocatalytic removal curves of RhB (c) and $\text{Cr}(\text{vi})$ (d). The corresponding kinetics of RhB oxidation (e) and $\text{Cr}(\text{vi})$ reduction (f).⁴⁵ Copyright 2019, Copyright 2020, Elsevier.



holes move in the opposite direction, maximizing photocurrent response at a 1 : 3 molar ratio. Under visible light, the composite degrades >99% of malachite green within 2 h (complete removal in 60 min) with optimal activity. The study confirms that the synergism between ferroelectric BiFeO₃ and Bi₂S₃ can amplify the photocatalytic merits of 3D nanostructures, offering a new design concept for high-efficiency Bi₂S₃-based photocatalysts in environmental remediation.

4. Optimization strategies for Bi₂S₃ photocatalysis

4.1. Heterojunction construction

4.1.1. Type-II heterojunctions. A Type-II band alignment introduces a staggered offset that spatially separates photogenerated electrons and holes, prolonging carrier lifetime and suppressing charge recombination. Owing to its narrow gap (~1.3 eV) and large absorption coefficient, Bi₂S₃ can act as either electron donor or acceptor in Type-II assemblies. Lian *et al.*⁶³ employed BiVO₄ nanorods as a core and carried out *in situ* surface sulfidation to co-grow a Bi₂S₃ shell. In this nanostructure, the two phases share Bi atoms, mutually coupling their electronic structures and reducing interfacial lattice mismatch. *In situ* impedance spectroscopy revealed a carrier-transport activation energy (CTAE) as low as 0.261 eV, markedly lowering the energy barrier for charge separation and migration. Benefiting from atomic-scale interfacial contact, enhanced visible-light absorption (edge extended to 1007 nm) and highly efficient carrier separation, BiVO₄@Bi₂S₃ exhibits dramatically improved photocatalytic Cr(vi) reduction with 50 ppm Cr(vi) completely reduced within 40 min, along with an

apparent rate constant 35.5 times that of pure BiVO₄. This work first demonstrates that sharing atoms to build an inorganic heterojunction can effectively weaken coulombic repulsion between the two phases, offering a new strategy for boosting carrier-migration efficiency in Type-II heterojunctions. Dang *et al.*⁶⁴ fabricated In₂S₃@Bi₂S₃ core-shell nanoflowers *via* a one-pot hydrothermal route (Fig. 14). Leveraging narrow band gap and high visible-light absorption of Bi₂S₃ together with strong photosensitivity and photocorrosion resistance of In₂S₃, the pair form a type-II heterojunction that spatially separates photogenerated carriers. During discharge, electrons from the In₂S₃ conduction band migrate to Bi₂S₃ to drive oxygen-reduction, while holes from the Bi₂S₃ valence band move to In₂S₃ to oxidize discharge products. Light energy deepens the reaction depth and accelerates charge exchange, delivering bifunctional catalysis. This strategy couples visible-light harvesting with electrochemical energy storage through Type-II band engineering, offering a new avenue for addressing energy shortages *via* photo-assisted Li-O₂ batteries. Yuan *et al.*⁶⁵ fabricated a Bi-TCPP/Bi₂S₃ heterojunction *via* a one-pot route. Interaction between the metalloporphyrin Bi-TCPP and Bi₂S₃ generates oxygen vacancies (Ov) that prolong carrier lifetime, enhance light absorption and activate reactants. A Type-II band alignment drives electrons from Bi₂S₃ to Bi-TCPP and holes in the opposite direction, suppressing charge recombination. For the first time the “Ov + Type-II” strategy was applied to photocatalytic Cr(vi) reduction, extending Type-II heterojunctions to environmental remediation.

Collectively, these studies push Type-II interfacial charge-transfer efficiency to new levels while achieving full visible-to-near-infrared absorption and spatial separation of oxidative and reductive sites, offering a universal design framework for

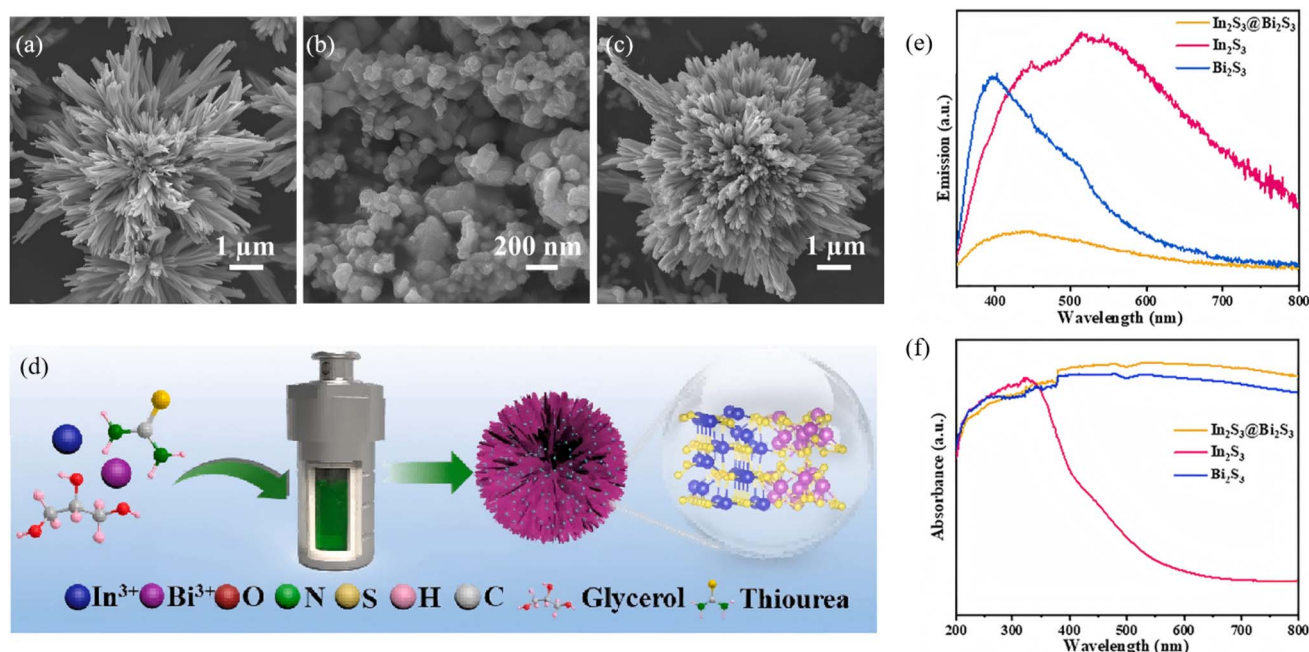


Fig. 14 SEM images of (a) Bi₂S₃, (b) In₂S₃ and (c) In₂S₃@Bi₂S₃. (d) Schematic illustration of synthesis procedures for In₂S₃@Bi₂S₃. (e) PL and (f) UV-vis absorption spectra of Bi₂S₃, In₂S₃ and In₂S₃@Bi₂S₃.⁶⁴ Copyright 2023, Elsevier.



high-performance Bi_2S_3 -based full-spectrum photocatalytic systems.

4.1.2. Z-scheme heterojunctions. Z-scheme architectures preserve the strongest oxidation and reduction potentials of each semiconductor by forcing photogenerated electrons and holes to recombine across the junction, and are therefore considered the ultimate platform for full-spectrum photocatalysis. Thanks to its narrow band gap and deep-lying valence band, Bi_2S_3 frequently serves as the visible-to-NIR-responsive electron donor in such systems. Fan *et al.*⁶⁶ fabricated a 1D $\text{Bi}/\text{Bi}_2\text{S}_3\text{-BiVO}_4$ Z-scheme composite that delivers outstanding performance for tetracycline degradation (Fig. 15). Metallic Bi broadens the light-harvesting window *via* localized surface plasmon resonance (LSPR), suppresses carrier recombination, and participates in a tri-phase heterojunction to accelerate charge transfer. Bead-like BiVO_4 decorated with needle-like Bi_2S_3 increases the specific surface area and shortens carrier-transport paths. The system simultaneously preserves the strongly oxidative holes of the BiVO_4 valence band (VB) and the highly reductive electrons of the Bi_2S_3 conduction band (CB), raising the tetracycline degradation rate by more than 3 times compared with pure BiVO_4 . Recently, Guo *et al.*⁶⁷ reported a Z-scheme $\text{Bi}_2\text{S}_3/\text{Ag}_2\text{S}$ heterojunction that harvests photons across the entire UV-to-NIR window. Within the junction, electrons in the Ag_2S conduction band recombine with holes in the

Bi_2S_3 valence band, leaving Ag_2S CB electrons with strong reducing power and Bi_2S_3 VB holes with strong oxidizing power. The optimized $\text{Bi}_2\text{S}_3/\text{Ag}_2\text{S}$ sample delivers high degradation efficiencies under all spectral regions, that is, 86% under UV (8 times that of bare Bi_2S_3), 84% under visible (5 times), and 88% under NIR (4.4 times) while retaining stable performance after five consecutive cycles. This extends Z-scheme photocatalysis into the near-infrared region, surpassing the limitations of single-phase NIR photocatalysts. The outstanding organic-pollutant purification is directly ascribed to the staggered band alignment and the internal electric field directed from Ag_2S to Bi_2S_3 , which preserves the coexistence of strongly reductive Ag_2S CB electrons and highly oxidative Bi_2S_3 VB holes.

Building on this, Chachvalvutikul *et al.*⁶⁸ fabricated a direct Z-scheme $\text{Bi}_2\text{S}_3/\text{ZnIn}_2\text{S}_4$ photocatalyst that exhibits markedly enhanced activity toward methylene-blue degradation. Photogenerated electrons in the Bi_2S_3 CB jump to the ZnIn_2S_4 VB and recombine there, leaving strongly reducing electrons in the ZnIn_2S_4 CB (-0.97 eV *vs.* NHE) to reduce O_2 to $\cdot\text{O}_2^-$, and strongly oxidizing holes in the Bi_2S_3 VB to attack MB directly. The $\cdot\text{O}_2^-$ radicals are further reduced to $\cdot\text{OH}$ radicals that assist in dye decomposition. The 12.5 wt% $\text{Bi}_2\text{S}_3/\text{ZnIn}_2\text{S}_4$ composite shows the best performance, achieving 95.4% MB removal in 300 min. It is far superior to bare ZnIn_2S_4 (64.2%) and still retains 87.4% efficiency after three cycles, confirming excellent

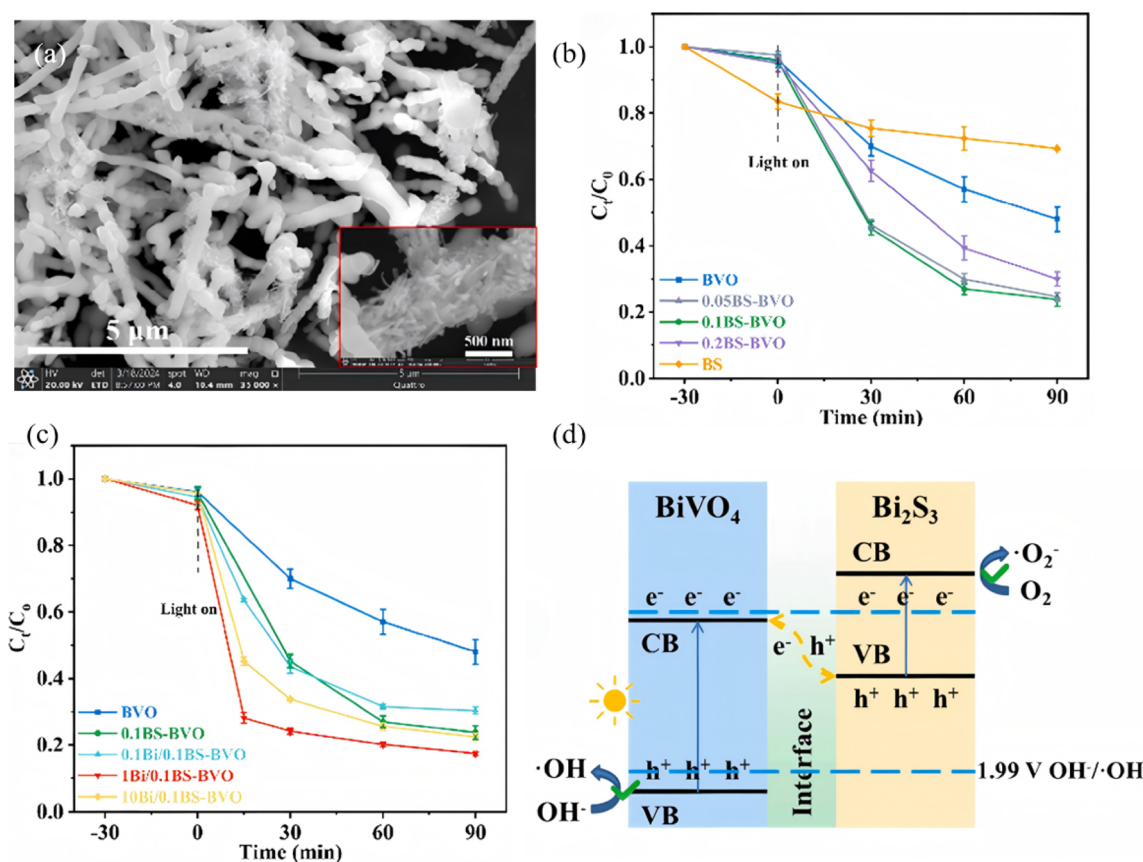


Fig. 15 (a) SEM images of 1Bi/0.1BS-BVO nano-chains. Photodegradation performance of TCH with (b) BS-BVO, and (c) Bi/BS-BVO. (d) Schematic diagram of the band structure: Z-scheme heterojunction of BS-BVO.⁶⁶ Copyright 2025, Elsevier.



stability. This fully validates the unique advantage of the Z-scheme charge-transfer pathway in simultaneously preserving the powerful reducing electrons of ZnIn_2S_4 and the strong oxidizing holes of Bi_2S_3 .

4.1.3. p-n junctions. A p-n junction separates photogenerated electrons and holes through a built-in electric field (BEF), providing a classical yet powerful route to enhance Bi_2S_3 photocatalysis. Recent studies have quantitatively correlated junction-field strength, depletion width and resulting photo-response. Sang *et al.*⁴⁵ produced self-assembled $\text{Bi}_2\text{O}_3/\text{Bi}_2\text{S}_3$ nanoflowers through a one-pot hydrothermal process, forming an intimate native p-n junction that drives efficient charge separation for enhanced photocatalytic performance. The built-in electric field drives electrons toward n-type Bi_2O_3 while holes remain in p-type Bi_2S_3 , furnishing a strong force for carrier separation. Thus, 99.72% of RhB is degraded and Cr(VI) is reduced within 90 min. Ke *et al.*⁶⁹ constructed a n- Bi_2O_3 /p- Bi_2S_3 /p- MoS_2 triple p-n heterojunction by inserting a p-type Bi_2S_3 interlayer between n-type Bi_2O_3 and p-type MoS_2 (Fig. 16). The engineered Fermi-level gradient suppresses electron-hole recombination and accelerates charge separation/transport. The resulting $\text{Bi}_2\text{O}_3/\text{Bi}_2\text{S}_3/\text{MoS}_2$ delivers a water-oxidation rate of $529.1 \mu\text{mol h}^{-1} \text{g}^{-1}$ that is 1.5 times that of bare Bi_2O_3 and 12.5 times that of bare MoS_2 . At the same time, it achieves 90% MB removal in 6 h. The Bi_2S_3 interlayer ensures favorable p-n band alignment, and the high conductivity of MoS_2 further boosts charge transfer, synergistically enhancing overall photocatalytic activity. Latifian *et al.*⁷⁰ introduced 0.3%, 0.6% and 1% Ti^{4+} into n- Bi_2S_3 (optimum 0.6%) to fabricate a Ti-doped

$\text{Bi}_2\text{S}_3/\text{NiO}$ p-n heterojunction. The study revealed that Ti incorporation not only tailors the band structure of Bi_2S_3 but also enables highly efficient separation of photogenerated carriers *via* the built-in electric field of the p-n junction with NiO. Under visible-light irradiation the optimal catalyst (0.6% Ti- Bi_2S_3 /1% NiO) degrades 80% of MB within 500 min, demonstrating markedly enhanced photocatalytic activity.

4.1.4. Schottky junction. A Schottky junction creates an ultrafast electron-extraction pathway across the metal-semiconductor interface, effectively suppressing the surface charge recombination and prolonging hole lifetime in Bi_2S_3 . Recent efforts have quantitatively linked Schottky-barrier height, charge-transfer kinetics and resulting photocatalytic activity. Hosseini *et al.*⁷¹ first converted Ti_3C_2 MXene into a 3D $\text{TiO}_2@-\text{Ti}_3\text{C}_2$ framework by hydrothermal oxidation, then electrostatically assembled 2D Bi_2S_3 nanosheets onto the surface to obtain a hierarchical $\text{TiO}_2@-\text{Ti}_3\text{C}_2/\text{Bi}_2\text{S}_3$ Schottky-Z-scheme junction. Ti_3C_2 MXene serves as an interlayer that interfaces simultaneously with TiO_2 and Bi_2S_3 , greatly accelerating charge separation. The synergistic Schottky-Z-scheme synergy makes Ti_3C_2 act as a Schottky barrier that speeds photo-carrier extraction while the Z-pathway preserves the strong redox potentials of both semiconductors, suppressing electron-hole recombination. Under visible light, $\text{TiO}_2@-\text{Ti}_3\text{C}_2/20\%$ Bi_2S_3 degrades 84.13% of 40 mg L^{-1} tetracycline in 135 min with a rate constant 3 times that of $\text{TiO}_2@-\text{Ti}_3\text{C}_2$. The $\cdot\text{O}_2^-$ and $\cdot\text{OH}$ radicals are determined as the dominant species. $\text{TiO}_2@-\text{Ti}_3\text{C}_2/1\%$ Bi_2S_3 delivers the highest H_2 -evolution rate ($14\ 141.23 \mu\text{mol g}^{-1} \text{h}^{-1}$) that is 2.37 times that of $\text{TiO}_2@-\text{Ti}_3\text{C}_2$. Both optimal catalysts

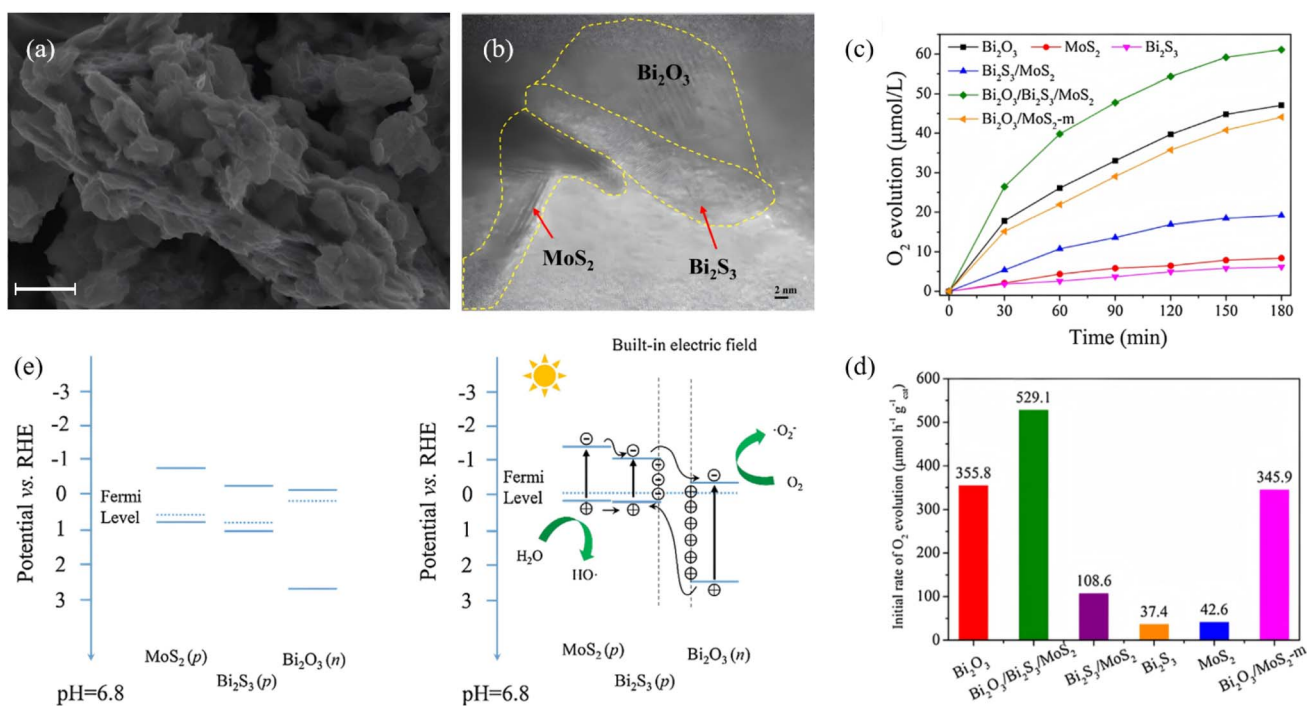


Fig. 16 (a) SEM images of $\text{Bi}_2\text{O}_3/\text{Bi}_2\text{S}_3/\text{MoS}_2$. (b) High-resolution TEM images of $\text{Bi}_2\text{O}_3/\text{Bi}_2\text{S}_3/\text{MoS}_2$. (c) Photocatalytic activity for O_2 evolution. (d) Initial water oxidation rate of the different samples under simulated solar light irradiation. (e) Schematic diagram for energy band of Bi_2O_3 , MoS_2 , and Bi_2S_3 and the formation of the three-phase p-n heterojunction and the possible charge separation.⁶⁹ Copyright 2017, Elsevier.



retain activity and crystal integrity after three cycles, demonstrating excellent recyclability. Sun *et al.*⁷² constructed an Au NSs/Bi₂S₃/TiO₂ double-heterojunction, wherein a Schottky contact between Au NSs and Bi₂S₃ and an S-scheme junction between Bi₂S₃ and TiO₂ is formed (Fig. 17). The surface-plasmon resonance (SPR) of Au NSs pushes absorption into the near-infrared (NIR) region, and the narrow-band-gap Bi₂S₃ (~1.3 eV) covers the visible region, while TiO₂ responds to UV, collectively achieving full UV-Vis-NIR spectral coverage. Under NIR excitation, hot electrons generated in Au NSs are injected into the Bi₂S₃ CB *via* the Schottky junction. The H₂-evolution rate of Au NSs/Bi₂S₃/TiO₂ reaches 5.754 mmol g⁻¹ h⁻¹, markedly higher than that of either single junction. TRPL reveals a shortened carrier lifetime (0.23 ns *vs.* 0.79 ns for pristine TiO₂), confirming that the dual junction accelerates charge separation and transfer. This synergistic double-junction design simultaneously broadens the spectral window and enhances redox power.

4.2. Element doping

4.2.1. Metal-ion doping.

Substitutional metal ions introduce extra carriers and mid-gap states into the Bi₂S₃ lattice, systematically enhancing visible-light harvesting, carrier lifetime and surface reaction kinetics. Zhou *et al.*⁷³ employed a two-step protocol, *i.e.*, SILAR followed by hydrothermal treatment to fabricate Ho³⁺-doped Bi₂S₃ thin films. Incorporation of Ho introduces an impurity level that narrows the band gap from 1.67 eV to 1.50 eV, lowering the electron transition energy and increasing the number of photogenerated carriers. As a result, the Ho³⁺-modified film exhibits a 30% higher photovoltage, a 1.97 times larger photocurrent density, and a three-order-of-magnitude increase in carrier concentration, confirming that Ho doping significantly improves the photoelectronic properties of Bi₂S₃. Nkwe *et al.*⁷⁴ prepared Cu²⁺-doped Bi₂S₃ nanorods *via* a solvothermal route (Fig. 18). Cu²⁺ substitutes for Bi³⁺, which is beneficial for injecting extra electrons into the lattice. This substitution broadens visible-light absorption, tailors the local electron density to optimize the band structure, and

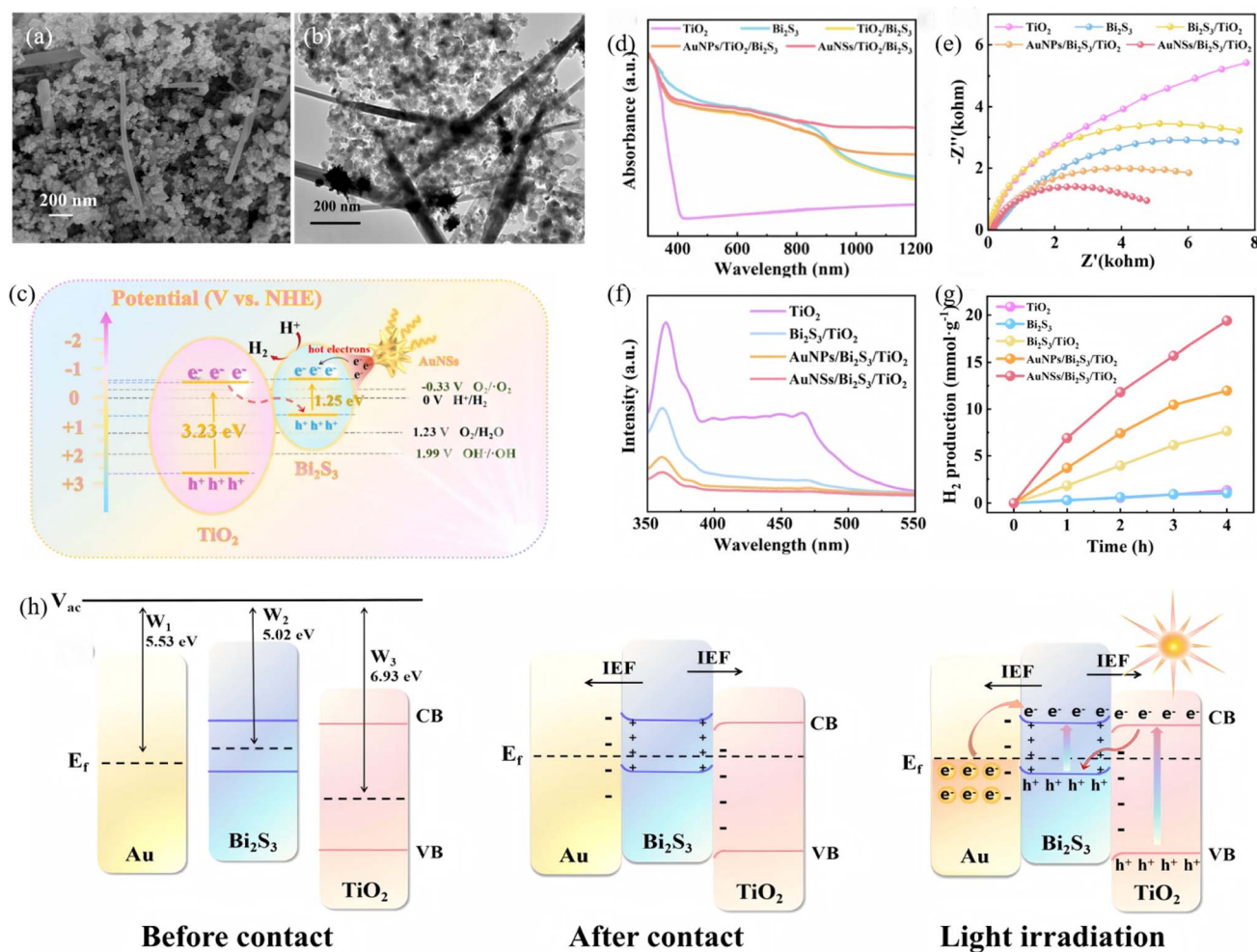


Fig. 17 (a) SEM and (b) TEM images of Au NSs/Bi₂S₃/TiO₂. (c) Schematic representation of Schottky/S-scheme charge transfer mechanisms. (d) DRS spectra, (e) Electrochemical impedance spectroscopy, (f) PL spectra, (g) H₂ evolution performances of different samples, (h) Schottky/S-scheme heterojunction mechanisms including before contact, after contact, and under light irradiation.⁷² Copyright 2025, Royal Society of Chemistry.



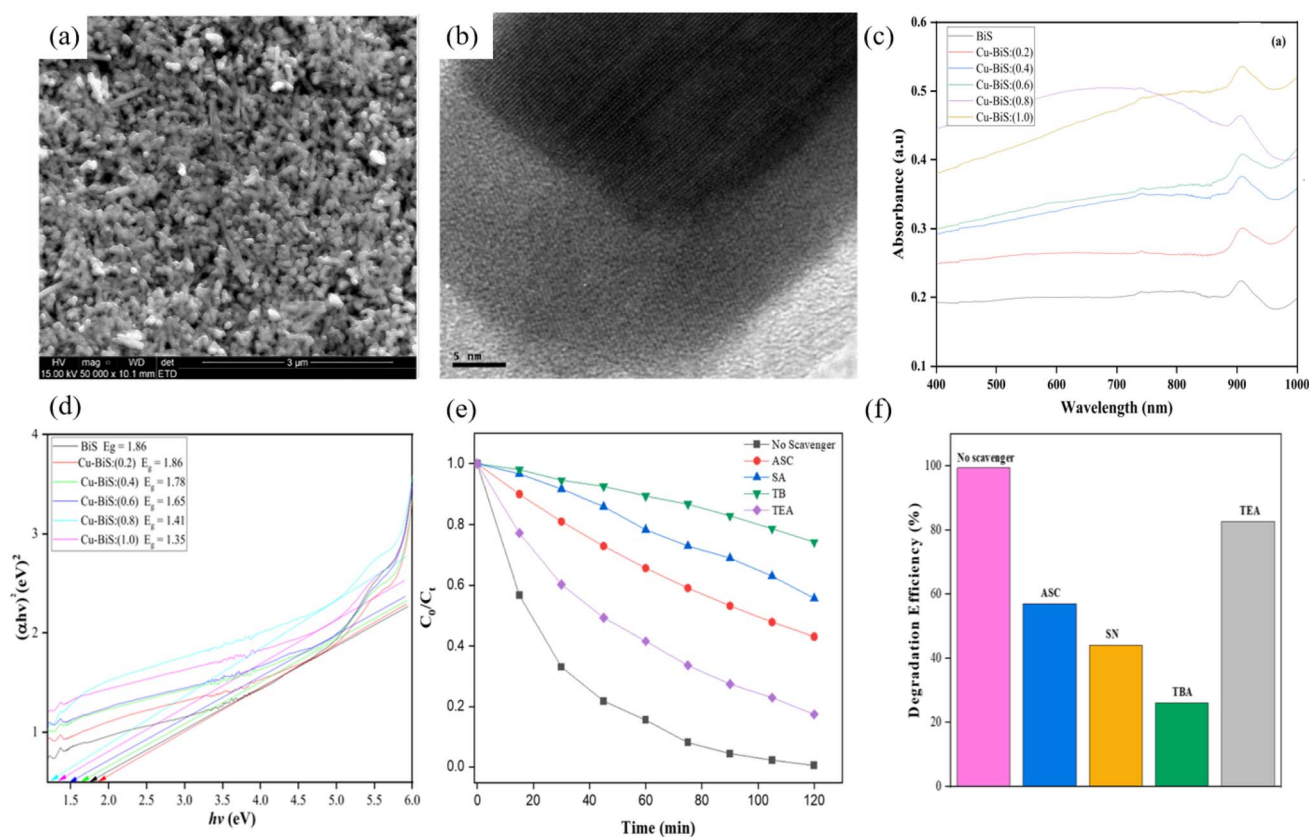


Fig. 18 (a) SEM and (b) HRTEM images of Cu-BiS (0.4). (c and d) UV-vis-NIR absorption spectra of (c) pure Bi_2S_3 and doped Bi_2S_3 nanoparticles with different dopant concentration (0.2, 0.4, 0.6, 0.8 and 1.0 mol/L) with corresponding (d) Tauc plots. (e and f) UV-visible absorption spectra of (e) degradation percentage of MO with change in time; and (f) the corresponding photodegradation efficiency (ASC, SA, TB, and TEA).⁷⁴ Copyright 2023, Elsevier BV.

markedly enhances surface reactivity. The prolonged carrier lifetime increases the photocatalytic degradation rate constant for methyl orange (MO) by 1.5 times compared with undoped Bi_2S_3 . Du *et al.*⁷⁵ hydrothermally coupled Cu-doped Bi_2S_3 with BiOCl to form an n-n $\text{BiOCl}/\text{Cu-doped Bi}_2\text{S}_3$ heterojunction. Wherein Cu^{2+} acts as an interfacial mediator that traps photoelectrons from the BiOCl CB, preventing electron-hole recombination. These captured electrons subsequently reduce O_2 to $\cdot\text{O}_2^-$ radicals, boosting oxidation power. The heterojunction accelerates charge transfer and enlarges the specific surface area to $40.54 \text{ m}^2 \text{ g}^{-1}$ (vs. $23.70 \text{ m}^2 \text{ g}^{-1}$ for BiOCl and $6.78 \text{ m}^2 \text{ g}^{-1}$ for Cu-doped Bi_2S_3), increasing reactant adsorption and the number of active sites. The composite achieves 97.1% degradation of ciprofloxacin (CIP) within 20 min, far exceeding undoped/un-coupled systems (*i.e.*, Cu-doped Bi_2S_3 5%, bare Bi_2S_3 13%, and BiOCl 67%), exemplifying the doping and heterojunction synergy that amplifies interfacial charge separation. Latifian *et al.*⁷⁰ deposited NiO onto Ti^{4+} -doped Bi_2S_3 to form a $\text{Ti-Bi}_2\text{S}_3/\text{NiO}$ p-n heterojunction (Fig. 19). The markedly enhanced visible-light-responsive photocatalytic activity provides direct evidence that metal-ion doping plays a pivotal role in complex band engineering, in which Ti^{4+} down-shifts the CB minimum, while the p-type NiO possesses a higher VB edge. The resulting graded energetics strengthen the built-in electric

field, promoting separation of photogenerated electron-hole pairs. Under visible light, the MB degradation rate is 1.76 times that of pristine Bi_2S_3 , demonstrating that multi-element codoping can simultaneously amplify both the band gradient and the internal electric field.

4.2.2. Non-metal ion doping. Non-metal ions can hybridise valence orbitals, passivate defects and induce band-edge shifts in the Bi_2S_3 framework, delivering simultaneous enhancement of visible-to-NIR response and carrier lifetime. Shi *et al.*⁷⁶ fabricated a 3D hierarchical porous $\text{BiOI-Bi}_2\text{S}_3$ S-scheme heterojunction (Ov-BBS) (Fig. 20) *via* a one-step solvothermal route in which sulfur doping was used to tune the oxygen-vacancy content. After sulfur introduction the absorption edge red-shifted and the band gap of Ov-BBS-0.1 narrowed to 1.83 eV (vs. 1.93 eV for bare BiOI). DFT calculations and photoelectrochemical tests confirmed that sulfur doping and oxygen vacancies cooperate to optimize carrier separation and suppress charge recombination. Under UV-vis illumination, Ov-BBS-0.1 efficiently degrades/reduces four typical pollutants including MB, RhB, Cr(vi) and Tetracycline (TC). This work delivers an efficient, stable and broadly applicable Ov-BBS photocatalyst and offers a new strategy for designing high-performance photocatalysts for wastewater treatment.



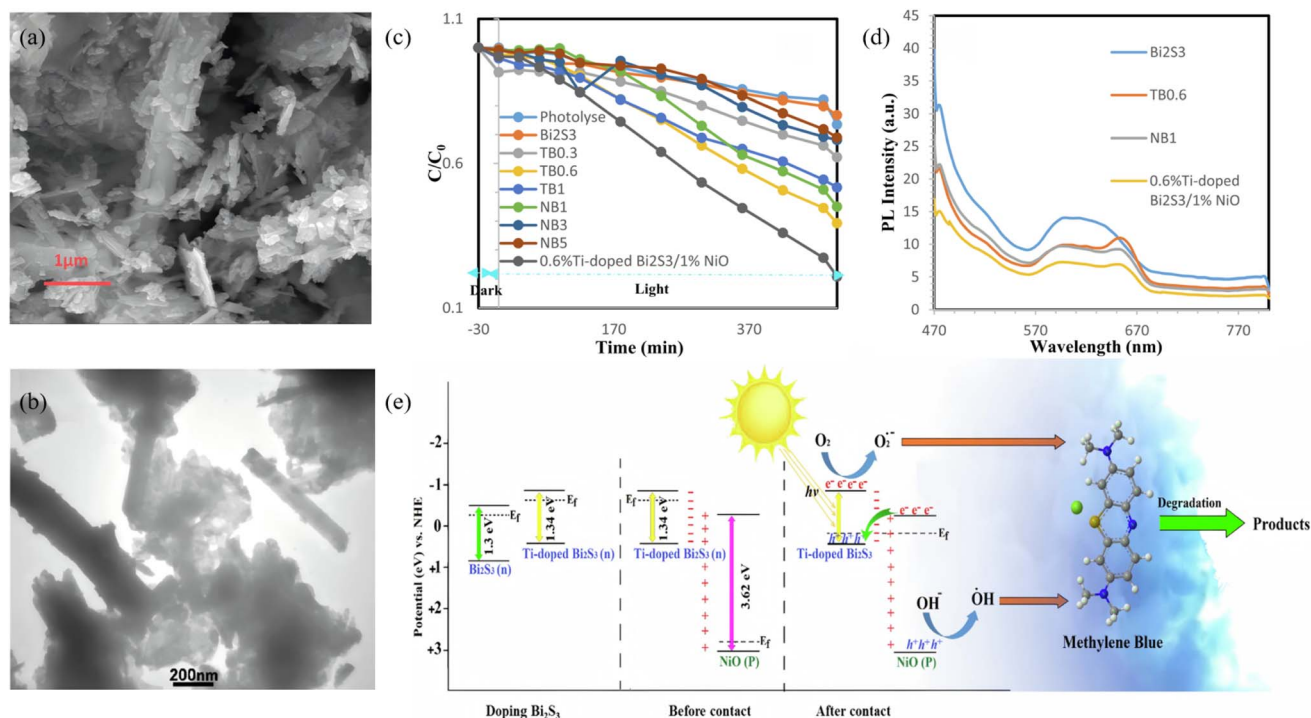


Fig. 19 (a) SEM image of 0.6% Ti-doped $\text{Bi}_2\text{S}_3/1\%$ NiO and (b) TEM image of 0.6% Ti-doped $\text{Bi}_2\text{S}_3/1\%$ NiO. (c) Photodegradation plots of MB over different samples. (d) PL spectra of Bi_2S_3 , TB0.6, NB1, and 0.6% Ti-doped $\text{Bi}_2\text{S}_3/1\%$ NiO. (e) The schematic diagrams of formation of Ti doping and p-n heterojunction and the photocatalytic degradation mechanism of MB by 0.6% Ti-doped $\text{Bi}_2\text{S}_3/1\%$ NiO.⁷⁰ Copyright 2023, Elsevier.

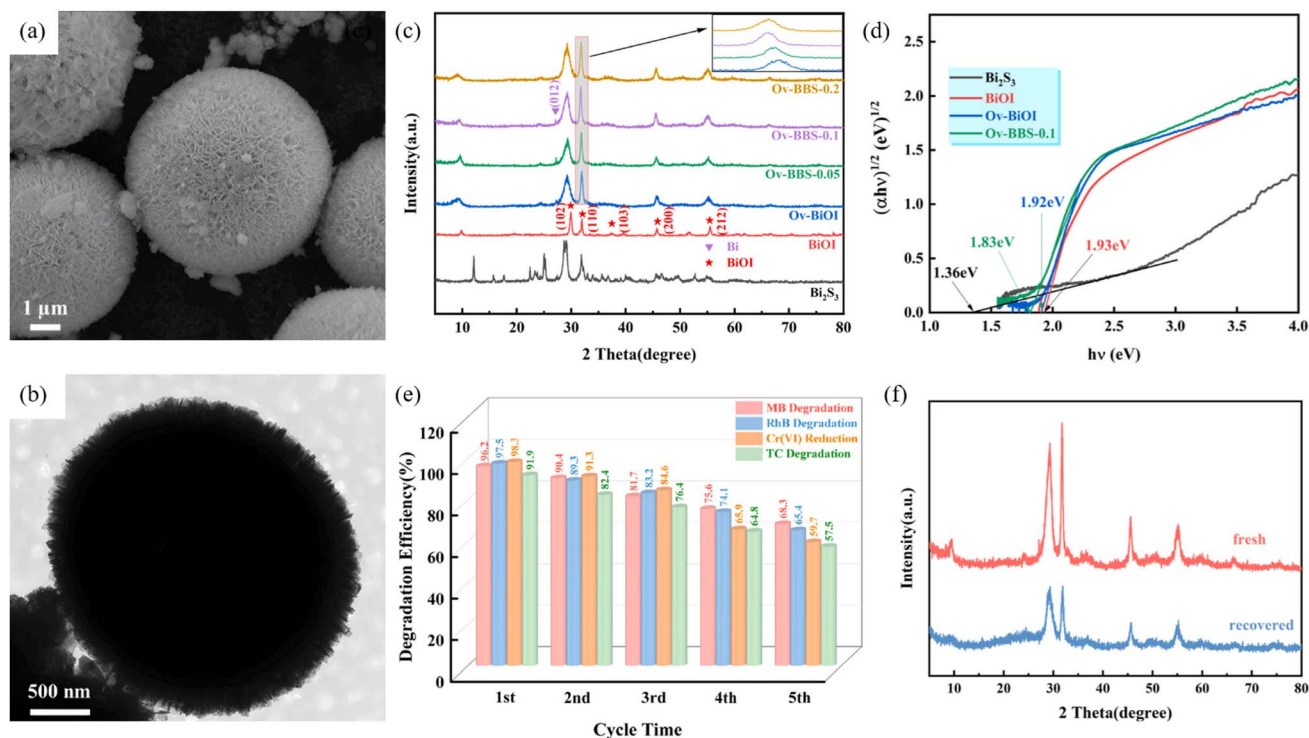


Fig. 20 (a) SEM and (b) TEM images of Ov-BBS-0.1 (c) XRD patterns of Bi_2S_3 , BiOI, Ov-BiOI, and Ov-BBS composites. (d) Curves of $(\alpha hv)^{1/2}$ versus $h\nu$ of Bi_2S_3 , BiOI, Ov-BiOI and Ov-BBS-0.1. (e) Cycling tests for the photocatalytic removal of MB, RhB, Cr(vi) and TC by Ov-BBS-0.1 catalyst. (f) XRD pattern of the fresh and recovered Ov-BBS-0.1 catalyst.⁷⁶ Copyright 2024, ELSEVIER SCI LTD.



4.3. Surface modification and defect engineering

4.3.1. Surface passivation. Surface defects are the dominant recombination centers for Bi_2S_3 photogenerated carriers. Passivation strategies therefore aim to lower surface-state density, introduce protective overlayers or create space-charge screening, thereby simultaneously extending carrier lifetime and boosting photocatalytic activity. Ganapathy *et al.*⁷⁷ prepared SrTiO_3 nanocubes and Bi_2S_3 nanorods *via* hydrothermal and microwave-assisted methods, respectively, then mixed them *via* ultrasonic dispersion, stirring, centrifugation and drying to obtain heterojunctions denoted STOB-1%, 3%, 5% and 7% (Fig. 21). Time-resolved photoluminescence (TRPL) revealed the fluorescence lifetime of bare SrTiO_3 and STOB-5%. Acting as a wide-band-gap passivation layer, SrTiO_3 creates an electron-reflecting barrier that blocks surface-defect trapping in Bi_2S_3 , reducing charge recombination and quenching the PL peak, which indirectly evidences that passivation lowers surface-state density. When the Bi_2S_3 content exceeds 5% (*e.g.*, STOB-7%), the PL intensity recovers. The authors attribute this to increased Bi_2S_3 surface-related defects, which enhances carrier recombination and slightly lower the H_2 -evolution rate (STOB-7%: $7.4 \text{ mmol g}^{-1} < \text{STOB-5%: } 7.7 \text{ mmol g}^{-1}$). Vu *et al.*⁷⁸ developed a one-step hydrothermal route that uses thiourea as the sulfur source and finely tunes the reaction kinetics of Bi^{3+} and Mo^{6+} to grow ultrathin MoS_2 flakes directly on Bi_2S_3 nanorods, yielding a hierarchical $\text{Bi}_2\text{S}_3@ \text{MoS}_2$ heterojunction. Because the solubility product of Bi_2S_3 (1.0×10^{-97}) is orders of magnitude smaller than that of MoS_2 (2.2×10^{-56}), Bi^{3+} reacts first with the sulfur source to form Bi_2S_3 nanorods; once Bi^{3+} is depleted, Mo^{6+} is reduced *in situ* to Mo^{4+} by thiourea and nucleates on the Bi_2S_3 surface, producing a conformal coating of MoS_2

nanosheets. The resultant heterostructure, with well-matched energy levels, promotes efficient separation of photogenerated carriers, achieving a total RhB removal of 97.5% and retaining stable performance after three consecutive cycles. Zha *et al.*⁷⁹ modulated oxygen vacancies (OVs) and interfacial chemistry to suppress charge recombination and stabilize active sites, thereby boosting photocatalytic NO oxidation. Annealing the $\text{BiVO}_4\text{-Bi}_2\text{S}_3$ heterojunction in N_2 at 340°C for 5 h generated Ovs that introduce defect levels which act as electron traps, capturing photogenerated electrons and inhibiting $e^- \text{-} h^+$ recombination. A subsequent O_2 atmosphere “repair” at 480°C for 4 h refilled the Ovs, demonstrating the reversible nature of the passivation. After Ovs are healed, carrier-transport efficiency drops and the photocurrent decreases from $6.4 \mu\text{A cm}^{-2}$ (OV sample) to $1.95 \mu\text{A cm}^{-2}$. The Ov- $\text{BiVO}_4\text{-Bi}_2\text{S}_3$ achieves 63.2% NO removal, 1.8 times higher than the untreated $\text{BiVO}_4\text{-Bi}_2\text{S}_3$ control (35.2%). After 20 cycles, the ESR signal of Ov- $\text{BiVO}_4\text{-Bi}_2\text{S}_3$ shows no obvious decay, confirming that the Ovs remain stable and the passivation effect is durable. By way of this post-passivation strategy, the dominant product is NO_3^- with negligible NO_2^- , minimizing secondary pollution. Collectively, these studies reduce Bi_2S_3 surface defect density by more than one order of magnitude and establish a direct correlation among defect density, carrier lifetime and photocatalytic activity, furnishing a universal passivation framework for high-efficiency Bi_2S_3 -based photocatalytic systems.

4.3.2. Engineering sulfur-vacancy-rich Bi_2S_3 . Sulfur vacancies (Sv) introduce mid-gap states and activate surface Bi sites, simultaneously enhancing visible-to-NIR absorption, prolonging carrier lifetime and tailoring reaction selectivity. Lan *et al.*⁸⁰ used $\text{SnCl}_4 \cdot 5\text{H}_2\text{O}$ as the tin source and deliberately added excess thioacetamide (TAA) to synthesize SnS_2 nanosheets rich

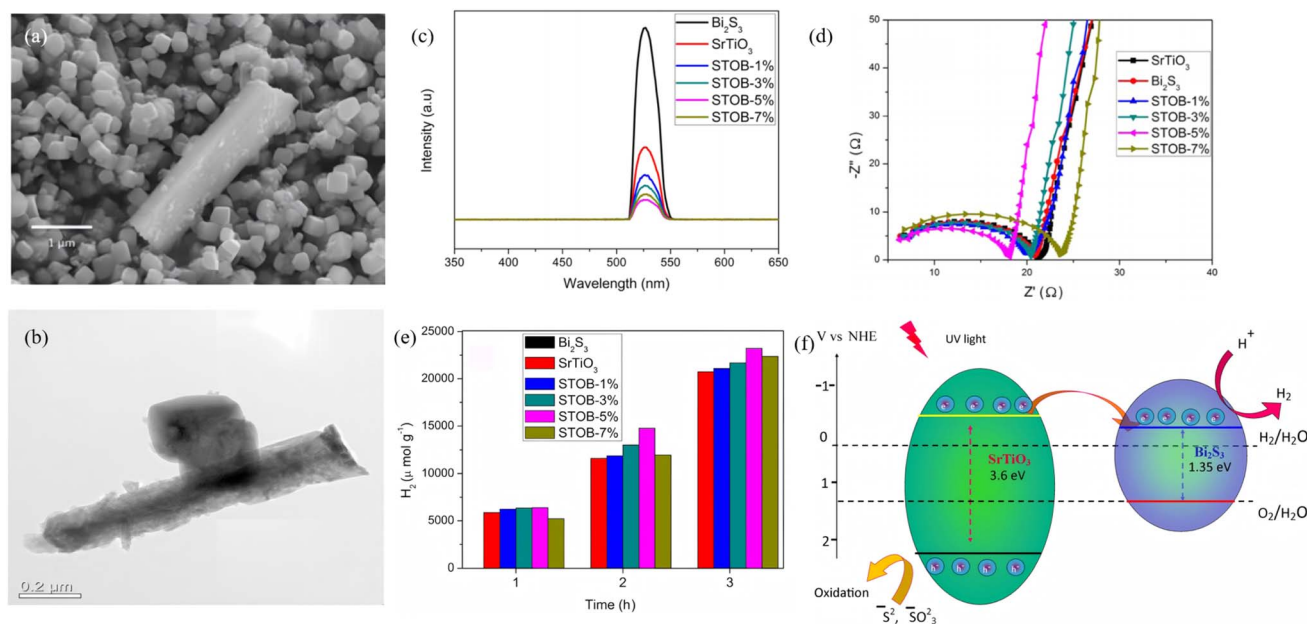


Fig. 21 (a) SEM and (b) TEM images of $\text{SrTiO}_3/\text{Bi}_2\text{S}_3$ (5%) heterojunction. (c) PL, (d) EIS analysis, and (e) photocatalytic hydrogen production performances of SrTiO_3 , Bi_2S_3 and $\text{SrTiO}_3/\text{Bi}_2\text{S}_3$ heterojunction. (f) Possible photocatalytic mechanism of the $\text{SrTiO}_3/\text{Bi}_2\text{S}_3$ heterojunction.⁷⁷ Copyright 2021, American Chemical Society.



in sulfur vacancies (Sv) *via* a hydrothermal route. The surplus sulfur in TAA is essential for vacancy formation. Ethylene glycol then served as both solvent and mild reductant for *in situ* deposition of Bi/Bi₂S₃ on the defective SnS₂ (Fig. 22). Samples containing Sv (SnS_{2-x} and Bi/Bi₂S₃/SnS_{2-x} series) exhibited markedly higher Cr(VI)-reduction and nitrogen-fixation activities than Sv-free SnS₂₋₀. Electron paramagnetic resonance (EPR) showed that the Bi/Bi₂S₃/SnS₂₋₂ heterostructure possessed the strongest Sv signal, evidencing the highest vacancy concentration. DFT calculations revealed that these high-density Sv sites act as catalytically active centers that accelerate N₂ adsorption/activation, giving the most favorable N₂ adsorption energy. Moreover, the enriched Sv sites narrow the SnS₂ band gap, extend visible-light absorption and thus enhance the overall photoresponse. Further work⁸¹ also demonstrated that a one-

step route to create a sulfur-vacancy-rich SnS/Bi₂S₃ Z-scheme photocatalyst yields intimate interfacial contact between SnS and Bi₂S₃. The resulting built-in electric field drives carriers along a Z-type pathway, effectively suppressing electron-hole recombination. The abundant sulfur vacancies additionally enhance charge separation and accelerate electron transfer, endowing the heterojunction with both high carrier separation efficiency and strong surface reaction activity. Zhu *et al.*⁸² successfully synthesized a Bi₂S₃ catalyst co-optimized by dendritic ultrathin nanosheets and sulfur vacancies. Among the samples, Vs-BS1 (annealed for 1 h) exhibited the best performance. The ultrathin architecture enhances charge separation efficiency and specific surface area, while sulfur vacancies boost photothermal conversion, stabilize reaction intermediates, and lower the thermodynamic energy barrier. The synergistic effect

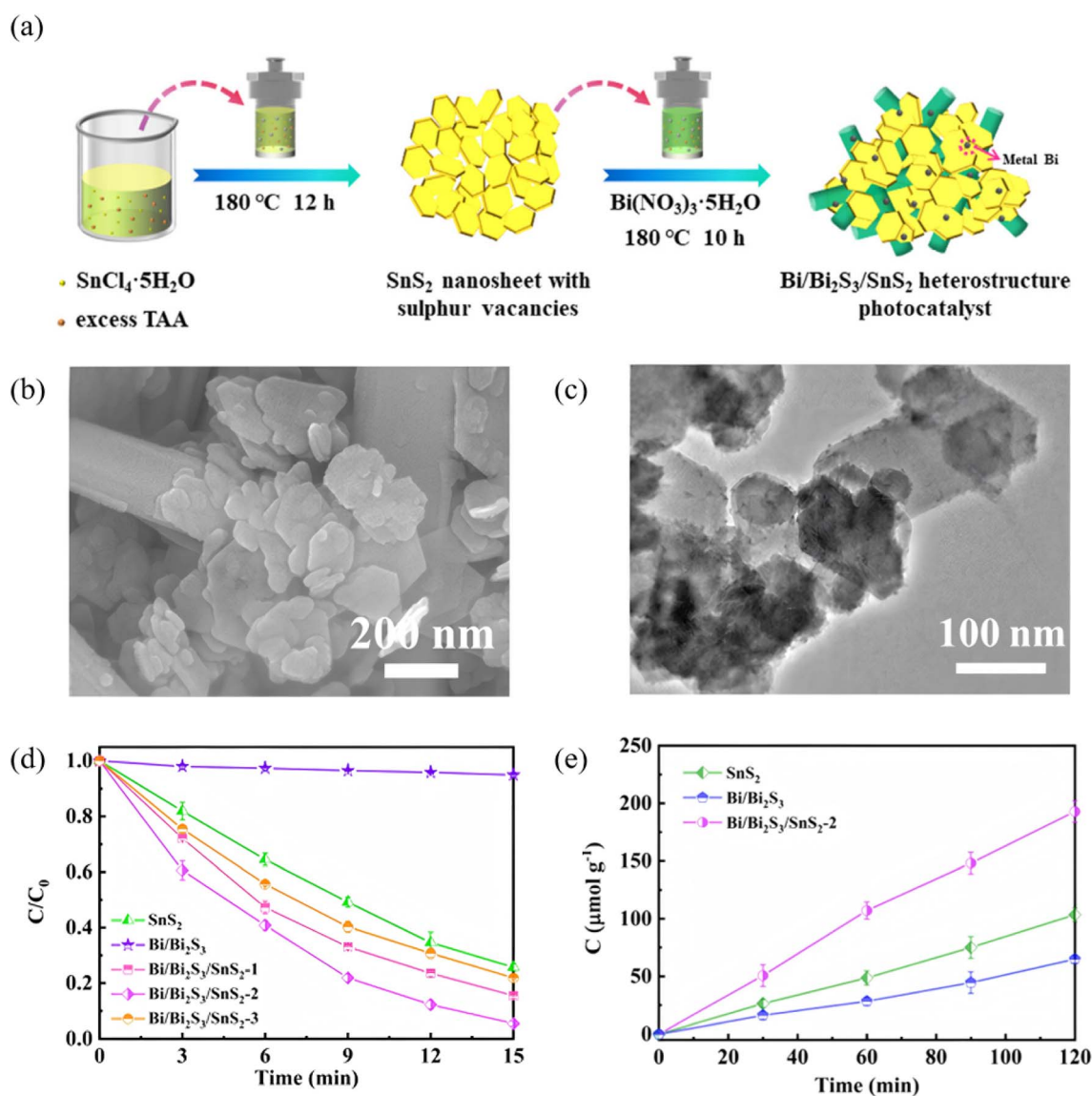


Fig. 22 (a) Diagram for the synthetic process of Bi/Bi₂S₃/SnS₂ heterostructure. (b) SEM and (c) TEM images of Bi/Bi₂S₃/SnS₂-2. (d) Reduction curves of Cr(VI) by SnS₂, Bi/Bi₂S₃, and Bi/Bi₂S₃/SnS₂. (e) Nitrogen fixation performance of SnS₂, Bi/Bi₂S₃, and Bi/Bi₂S₃/SnS₂-2.⁸⁰ Copyright 2023, Chinese Society of Metals.



achieved a CO yield of $250 \mu\text{mol g}^{-1} \text{h}^{-1}$ *via* photothermal CO₂ reduction, which is five times higher than that of pure photocatalysis and 3.5 times that of pristine Bi₂S₃. This study provides a new avenue for optimizing photothermal catalytic materials through structure design and defect engineering and offers a highly efficient candidate catalyst for CO₂ conversion and utilization. Collectively, these works establish sulfur-vacancy engineering as a pivotal tool for optimizing Bi₂S₃-based catalysis and provide a transferable roadmap for precise vacancy control in energy and environmental applications.

4.4. Co-catalyst loading

4.4.1. Noble-metal co-catalysts. Noble metals exhibit tunable Fermi levels, strong LSPR effect and high electron-storage capacity, enabling the formation of Schottky junctions or electron reservoirs on Bi₂S₃ that markedly accelerate charge separation and surface reaction kinetics. Nwaji *et al.*⁸³ developed a simple and low-cost route to prepare Au-nanoparticle-decorated Bi₂S₃ heterostructure photocatalysts (Fig. 23). A one-pot colloidal wet-chemistry protocol deposited Au NPs (~15 nm) onto Bi₂S₃ nanorods and nanoflowers, markedly boosting wastewater-treatment performance. The LSPR effect of Au NPs intensifies light absorption and accelerates charge separation, raising degradation efficiencies for MO and RhB to 97.4% and 95.1%, respectively, which 1.2 to 3 times higher than bare Bi₂S₃. ·OH and ·O₂⁻ are determined as the dominant active species, and the material retains high stability and recyclability under simulated sunlight irradiation, offering a new design concept for low-cost and high-performance photocatalysts and highlighting the dual plasmonic catalytic role of noble-metal

cocatalysts in full-spectrum environmental remediation. These studies establish that noble-metal decoration not only suppresses electron-hole recombination but also supplies abundant active sites and plasmonic heat, providing a versatile blueprint for the design of high-performance Bi₂S₃ photocatalysts.

4.4.2. Non-noble-metal cocatalysts. Earth-abundant alternatives offer low cost and high activity, forming junctions on Bi₂S₃ that enables bidirectional electron/hole shunting. Liu *et al.*⁸⁴ fabricated a Bi₂S₃/1T@2H-MoS₂ composite *via* a microwave-hydrothermal route in which Bi₂S₃ sheathes the edges of 1T@2H-MoS₂ (Fig. 24). The 1T phase accounts for 70.2%. The hybrid MoS₂ delivers dual-face synergy whereby the 2H phase acts as a photosensitizer and the metallic 1T phase accelerates charge transfer. Bare Bi₂S₃ and 1T@2H-MoS₂ reduce only 18% and 32% of Cr(VI), respectively, whereas sample S2 (1 : 1 molar ratio) achieves 89% reduction far superior to other ratios. S2 also degrades 96% of MB *versus* 28% for pure Bi₂S₃ and 70% for 1T@2H-MoS₂ alone. Leveraging the photosensitizer-cocatalyst dual role of 1T@2H-MoS₂ and the cooperative band alignment, the composite broadens light absorption and uses the metallic conductivity of 1T-MoS₂ to speed interfacial charge transfer, and thus accepts electrons from 2H-MoS₂, markedly suppressing electron-hole recombination and outperforming pristine Bi₂S₃. Vu *et al.*⁷⁸ fabricated a Bi₂S₃@MoS₂ hierarchical architecture *via* a hydrothermal route. The conformal coating of MoS₂ nanosheets boosts charge-separation efficiency, increases the number of catalytically active sites, and broadens the light-harvesting window. When the MoS₂ content reaches 50%, RhB is degraded to 97.5%. The MoS₂ shell also suppresses Bi₂S₃ photocorrosion, so the heterojunction retains its activity after

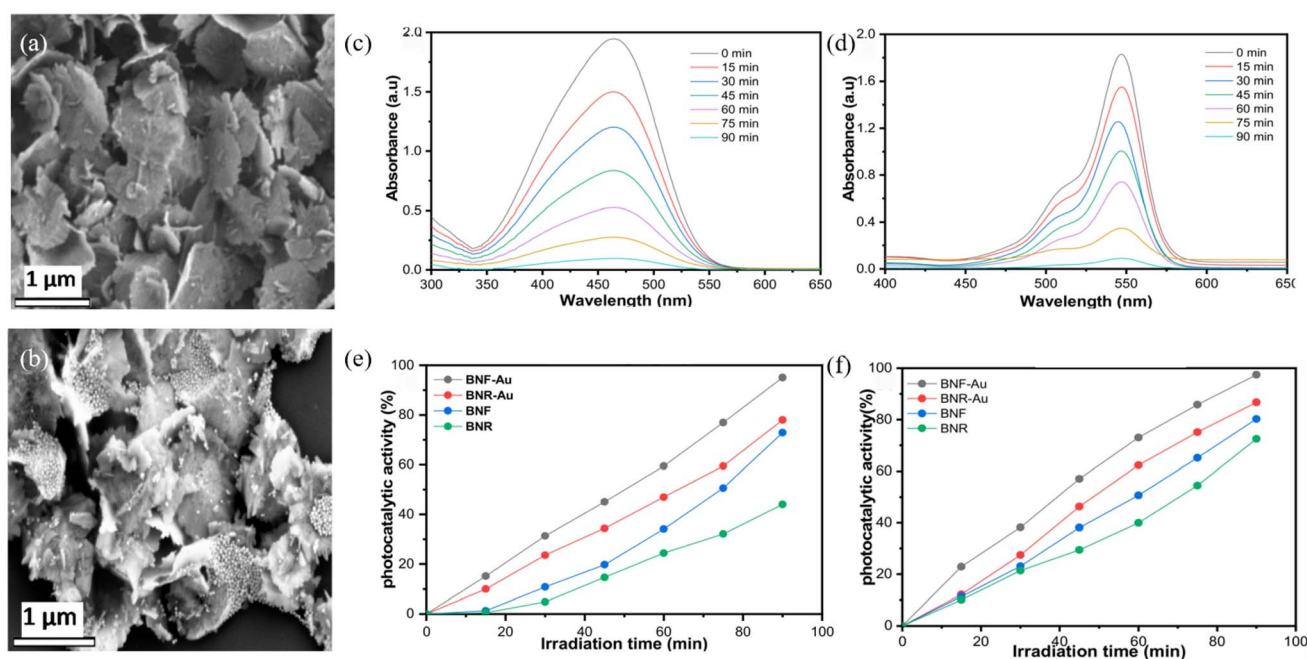


Fig. 23 (a) SEM images of flower-shaped Bi₂S₃ nanocrystals (BNF) and (b) BNF-Au. Representative absorbance changes of (c) MO, (d) RhB using BNR-Au, and the percentages degradation efficiency by the nanocrystals and corresponding gold decorated analogues for (e) RhB and (f) MO.⁸³ Copyright 2021, MDPI.



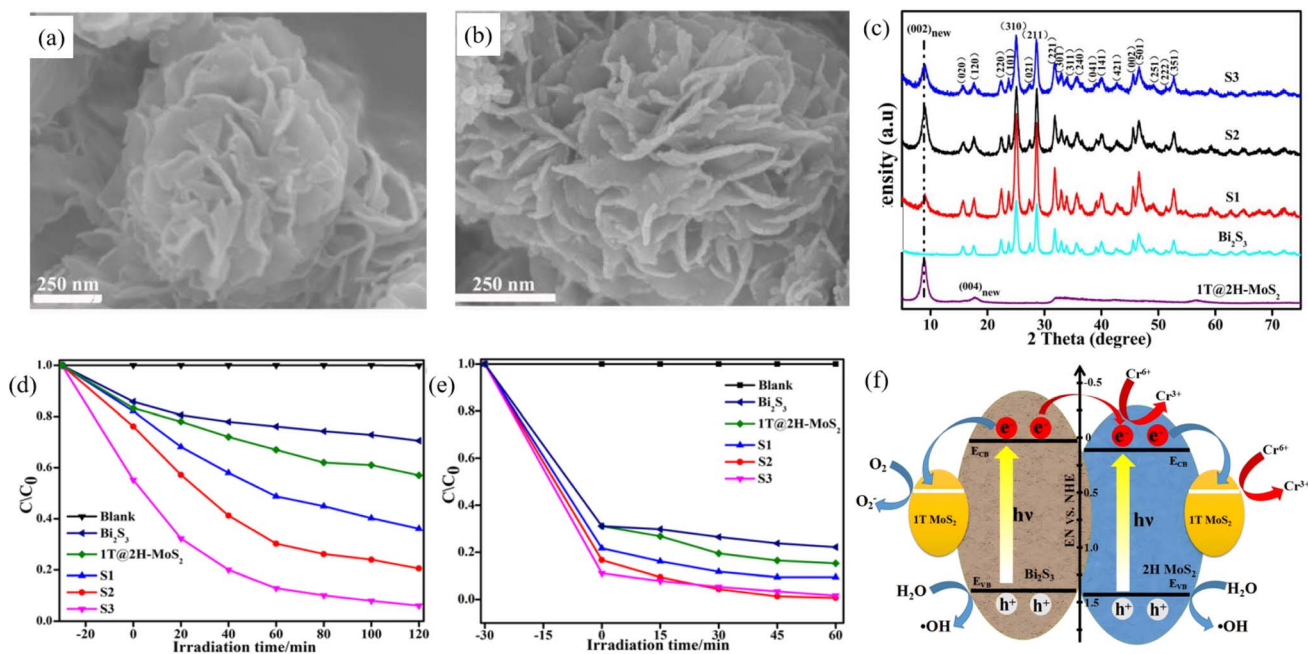


Fig. 24 SEM image of (a) 1T@2H-MoS₂, and (b) Bi₂S₃/1T@2H-MoS₂. (c) XRD pattern from 1T@2H-MoS₂, Bi₂S₃, and Bi₂S₃/1T@2H-MoS₂ heterojunctions with different molar ratios of 1T@2H-MoS₂. (d and e) Photo-reduction rates of potassium dichromate (d) and MB (e) under visible irradiation. (f) Schematic illustration of the photo-charge separation process over Bi₂S₃/1T@2H-MoS₂.⁸⁴ Copyright 2019, Elsevier.

three consecutive cycles with no noticeable decay. The composite thus exhibits both exceptional RhB adsorption and outstanding photocatalytic degradation performance. This design offers a valuable blueprint for developing low-cost and high-performance non-noble-metal cocatalyst systems. Leveraging their core advantages of natural abundance and low price, non-precious-metal cocatalysts have become the leading alternative to noble-metal counterparts. The accumulated studies have achieved significant advances in synthetic protocols, working mechanisms, application scenarios and performance optimization, laying a solid foundation for the industrial transformation of green catalysis technologies.

5. Applications of Bi₂S₃-based photocatalysts

5.1. Photocatalytic degradation of organic pollutants

Owing to its narrow band gap (~1.3 eV) and deeply positioned CB, Bi₂S₃ can generate highly reductive electrons under visible-to-NIR irradiation, making it an ideal candidate for cleaving dye conjugated systems and opening antibiotic rings, thereby achieving full-process reinforcement from rapid adsorption to complete mineralization.

Qu *et al.*⁸⁵ uniformly anchored Bi₂S₃ QDs on Bi₄NbO₈Cl nanosheets *via* an *in situ* ion-exchange strategy (Fig. 25). The pronounced quantum-confinement effect and abundant surface active sites extended the absorption edge and accelerated carrier separation. DFT calculations confirmed interfacial electron delocalisation that facilitates charge migration. Under visible light, 100% of RhB was degraded within 90 min, which is

far superior to bare Bi₄NbO₈Cl or Bi₂S₃, and the composite retained its activity after four cycles, demonstrating excellent stability. Holes (h⁺) were identified as the primary active species, assisted by [•]O₂⁻ and [•]OH radicals. When Bi₂S₃ is uniformly dispersed as quantum dots and coupled with Bi₄NbO₈Cl to form a heterojunction, a triple synergy emerges: (i) quantum-confinement intensified light absorption, (ii) heterojunction suppressed carrier recombination, and (iii) abundant active sites increase collision probability. Together these effects dramatically accelerate the photodegradation of organic pollutants such as RhB, endowing the composite with distinctive advantages in environmental remediation. Hao *et al.*⁸⁶ prepared Bi₂S₃ short nanorods (~100 nm) by a surfactant-free hydrothermal route and further assembled them with BiOBr nanosheets into a 1-D/2-D Bi₂S₃/BiOBr stack. The tight interface and morphology synergy boosted the degradation efficiency to 99.2% for RhB (15 min) and 86.2% for tetracycline (50 min). The enlarged surface area supplied sufficient active adsorption sites, while the green and scalable synthesis offers fresh insight into constructing high-performance sulfide-based heterojunctions. Nisa *et al.*⁸⁷ constructed a SnO₂/CdSe/Bi₂S₃ ternary heterojunction with a stepped band alignment that establishes an efficient electron-transfer highway. Under visible light, 100% MB removal was achieved in 60 min, while 75–99.8% degradation was obtained for RhB, MO and other dyes within the same time-frame. After five cycles, activity remained unchanged along with COD removal reached 91%, confirming effective mineralization. The superior activity originates from the narrow band gap (2.88 eV), multi-interface directional migration and spatial charge separation, which suppress charge recombination and lower charge-transfer resistance.



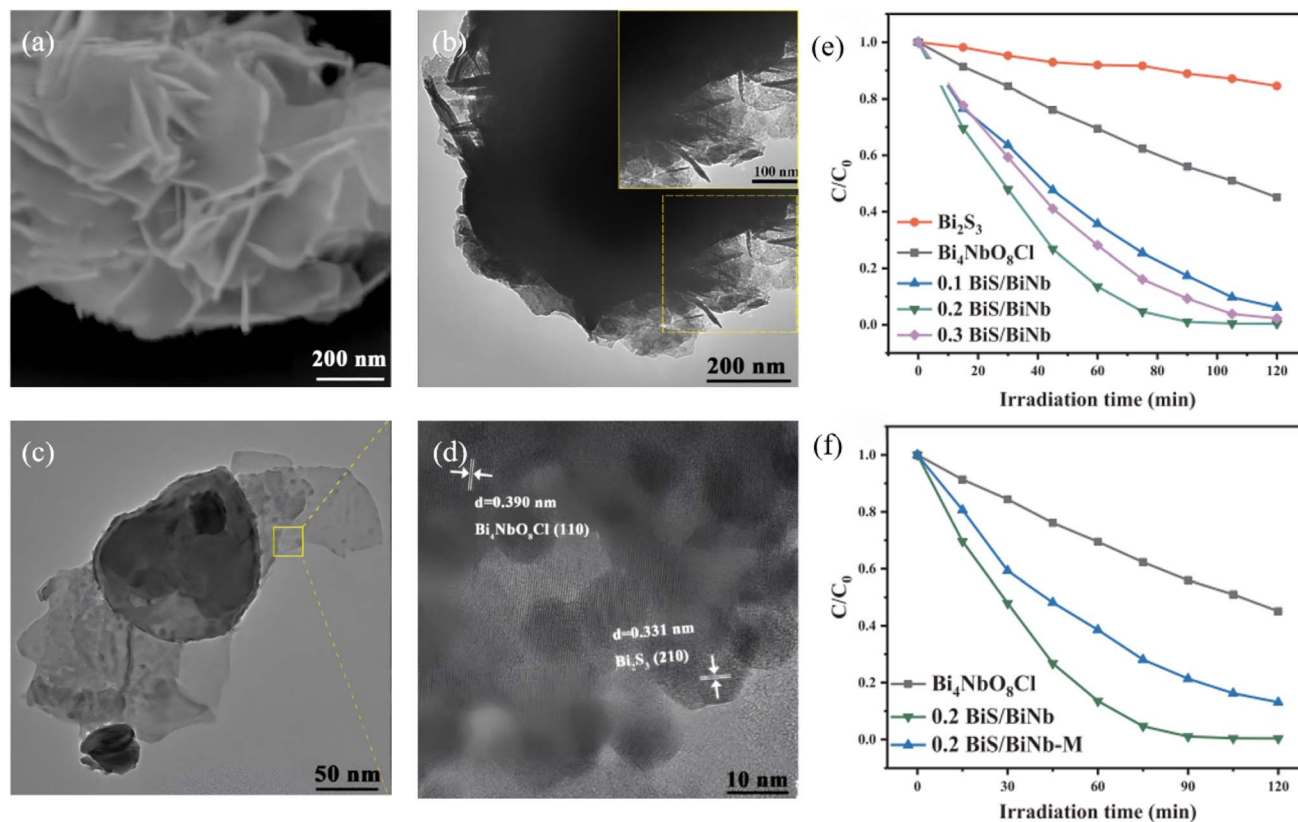


Fig. 25 (a and b) SEM, (c) TEM and (d) HRTEM image of 0.2 BiS/BiNb. (e) Photocatalytic degradation efficiencies of RhB with Bi_2S_3 , $\text{Bi}_4\text{NbO}_8\text{Cl}$, BiS/BiNb hetero-structures under visible-light irradiation. (f) Photocatalytic degradation efficiencies of RhB with $\text{Bi}_4\text{NbO}_8\text{Cl}$, 0.2 BiS/BiNb and 0.2 BiS/BiNb-M under visible-light irradiation.⁸⁵ Copyright 2020, Elsevier.

Collectively, these studies indicate that future Bi_2S_3 photocatalysts should prioritise QDs or ultrathin nanosheets as building blocks, while Type-II or stepped-band alignments can be exploited to redirect reaction intermediates, offering a tunable lever for target-specific degradation. Performance optimization has evolved from single-component modification to binary and then to multi-component heterojunction design, with the core scientific logic always centred on efficient separation, migration and utilization of photogenerated charge carriers. Future efforts should focus on atomic-scale engineering of heterointerfaces, *in situ operando* characterization of charge behaviour and pollutant degradation pathways, and the long-term stability and universality of catalysts under real and complex aquatic environments.

5.2. Photocatalytic reduction of heavy-metal ions

Among toxic aqueous contaminants, hexavalent chromium ($\text{Cr}(\text{VI})$) is priority owing to its high mobility and proven carcinogenicity. Photocatalytic reduction of $\text{Cr}(\text{VI})$ to trivalent chromium ($\text{Cr}(\text{III})$), which represents a species that readily precipitates as $\text{Cr}(\text{OH})_3$, offers an energy-efficient remediation route. Bi_2S_3 possesses a narrow band gap (~ 1.3 eV) and strong visible-light harvesting, yet suffers from rapid electron-hole recombination.

Constructing heterojunctions, elemental doping and morphology engineering have therefore been widely adopted to

accelerate interfacial charge transfer. Li *et al.*⁸⁸ fabricated a Bi_2MoO_6 (BMO)/ Bi_2S_3 framework *via* anion-exchange on MoO_3 nanobelts (Fig. 26). The open architecture increases specific surface area and shortens charge-diffusion paths. Optimal BMO/ Bi_2S_3 removes 100% of $\text{Cr}(\text{VI})$ within 15 min under visible light, with a rate constant 27.3 times higher than that of bare BMO. Photogenerated electrons are the main active species, assisted by $\cdot\text{O}_2^-$ radicals. The composite retains its activity after five cycles, confirming high stability. Wang H. *et al.*⁸⁹ prepared $\text{Bi}_2\text{S}_3/\text{BiVO}_4/\text{TiO}_2$ (BVT) films by *in situ/ex situ* methods. In the *in situ* prepared sample, Bi_2S_3 nanoribbons intimately contact $\text{BiVO}_4/\text{TiO}_2$, extending absorption into the visible region and increasing photocurrent density. Citric acid is oxidized by holes in the BiVO_4 VB, while electrons in the Bi_2S_3 CB reduce $\text{Cr}(\text{VI})$. The *in situ* BVT achieves 93.9% $\text{Cr}(\text{VI})$ reduction in 100 min, which is 14.6 times faster than bare TiO_2 , and maintains $\sim 70\%$ activity after four cycles. Wang *et al.*⁹⁰ vacuum-synthesized $\text{Bi}_2\text{S}_3/\text{Bi}$ heterojunctions in which metallic Bi nanoparticles form Schottky contacts with Bi_2S_3 . The metal phase acts as an electron mediator and additional $\text{Cr}(\text{VI})$ adsorption site. Carrier lifetime increases from 3.8 ns to 10.2 ns, and the reduction rate constant exceeds that of pristine Bi_2S_3 by a factor of 5.2. Wang *et al.*⁹¹ reported the preparation of C-doped $\text{BiOCl}/\text{Bi}_2\text{S}_3$ composite, in which the carbon insertion raises the conductivity and optimizes the band alignment. Photoelectrochemical detection of $\text{Cr}(\text{VI})$ over this catalyst exhibits a linear range of



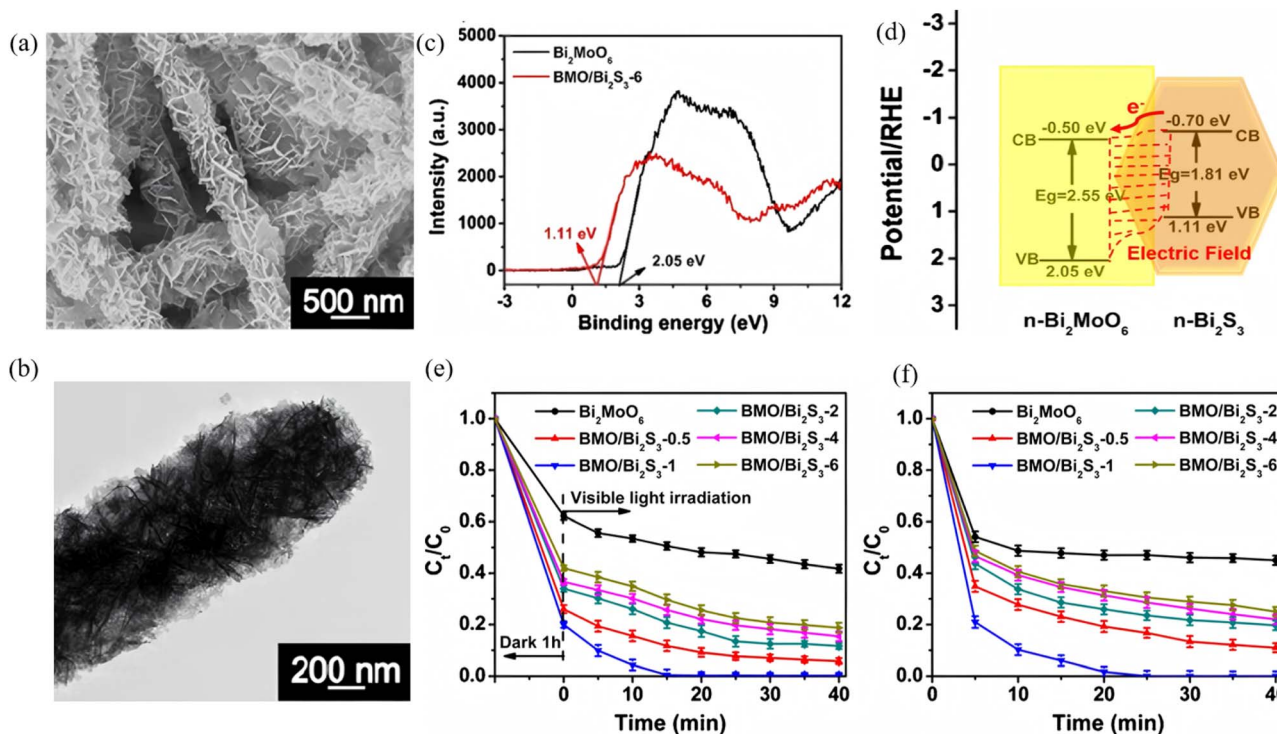


Fig. 26 (a) SEM and (b) TEM images of BMO/Bi₂S₃-1 heterojunction. (c) XPS VB spectra of pure Bi₂MoO₆ and BMO/Bi₂S₃-6. (d) Corresponding band structure of the BMO/Bi₂S₃-1 heterojunction. (e) Normal photocatalytic Cr(VI) reduction over different samples under visible light. (f) Direct photocatalytic reduction of Cr(VI) without dark treatment.⁸⁸ Copyright 2020, Elsevier.

0.02–80 μM with a detection limit of 16 nM; at pH 4, 99.5% of Cr(VI) is removed within 120 min, 336 times faster than bare BiOCl. Chahkandi *et al.*⁹² deposited Bi₂S₃ films on stainless-steel mesh by square-wave voltammetry, generating nano to micro-scale pores that enhance light harvesting and multiple scattering. Under solar light irradiation, single-component Cr(VI) is completely reduced within 100 min in a Cr(VI)/RhB binary system, in which hole capture by RhB suppresses charge recombination, enabling >93% simultaneous removal of both pollutants with good cyclic stability.

In summary, Bi₂S₃-based composite systems can markedly overcome the intrinsic shortcomings of pristine Bi₂S₃ for Cr(VI) reduction by constructing heterojunctions, doping with foreign elements, and optimizing synthetic protocols. These strategies effectively promote the separation and migration of photogenerated charge carriers, thereby greatly enhancing both the activity and stability of Bi₂S₃-based composites under visible-light irradiation. The key lies in a CB position that lies below the Cr(VI)/Cr(III) redox potential and in rapid interfacial electron transfer, endowing these materials with broad prospects for heavy-metal wastewater treatment.

5.3. Photocatalytic H₂ evolution

Bi₂S₃ has emerged as a key material for constructing high-efficiency hydrogen-evolution photocatalysts thanks to its narrow band gap and excellent visible-light harvesting capability. Nevertheless, its intrinsically rapid recombination of photogenerated charge carriers and insufficient chemical

stability severely limit its standalone performance. To overcome these bottlenecks, current research focuses mainly on two directions including building heterojunctions and optimizing interfacial charge transfer. Among them, coupling Bi₂S₃ with a well-matched semiconductor to form a heterojunction with ideal band alignment is regarded as one of the most effective strategies for promoting efficient charge separation, suppressing recombination, and enhancing stability.

Ganapathy *et al.*⁷⁷ constructed a SrTiO₃/Bi₂S₃ heterojunction that exploits the broad-spectral absorption of Bi₂S₃ and the well-aligned band positions of SrTiO₃, markedly promoting the separation and migration of photogenerated carriers and supplying abundant reductive electrons for the photocatalytic hydrogen evolution reaction. Because the SrTiO₃ CB is more negative (lower in energy), electrons transfer from the SrTiO₃ CB to the Bi₂S₃ CB, forming a Type-I heterojunction. Under UV light, the hydrogen evolution rate of composite is significantly higher than that of pure Bi₂S₃, and the composite retains good stability after three cycles. Recently, Liu *et al.*⁹³ developed an In-MOF-derived In₂S₃/Bi₂S₃ heterojunction that further boosts photocatalytic H₂ evolution (Fig. 27). Rod-like In₂S₃ obtained *via* high-temperature sulfidation was decorated *in situ* with flower-like Bi₂S₃ grown by a solvothermal method, creating an intimately contacted Type-II heterojunction. The unique architecture not only offers a large specific surface area and abundant active sites, but also enables efficient separation of photogenerated electron-hole pairs through the built-in electric field established at the heterointerface. The built-in electric field



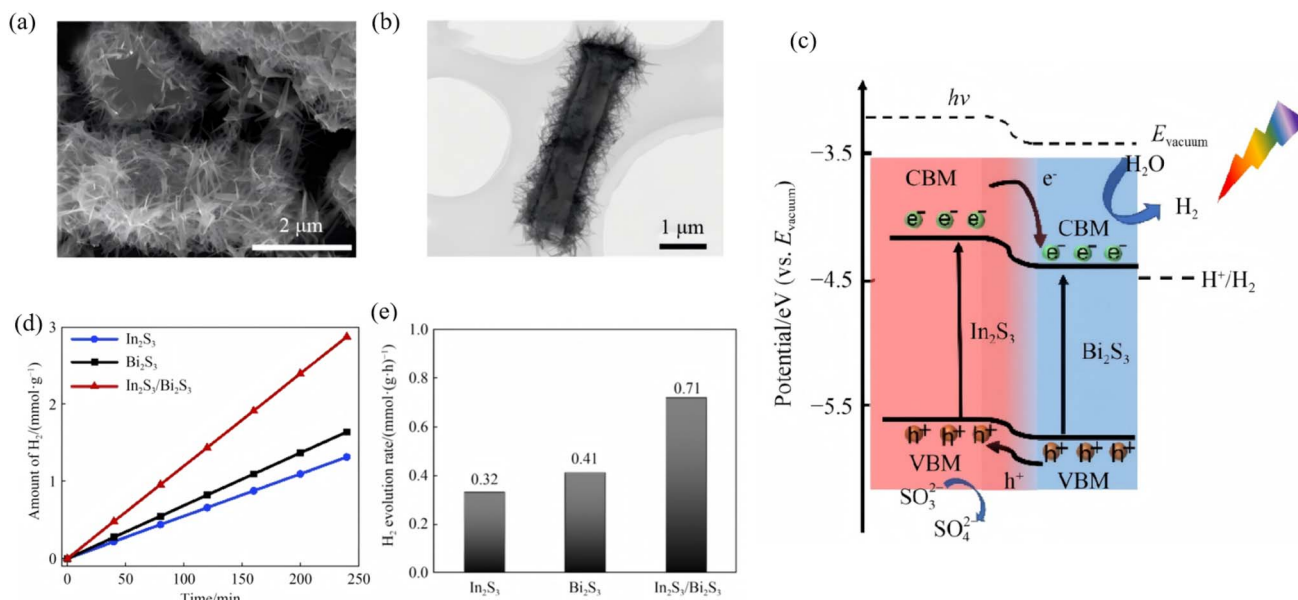


Fig. 27 (a) SEM image of In₂S₃/Bi₂S₃. (b) TEM image of In₂S₃/Bi₂S₃ heterojunction. (c) Energy level diagram and photocatalytic hydrogen production mechanism of the In₂S₃/Bi₂S₃. (d) Photocatalytic hydrogen production activity. (e) Photocatalytic hydrogen production rate.⁹⁵ Copyright 2023, Higher Education Press.

drives electrons from the In₂S₃ CB to the Bi₂S₃ CB for H₂ evolution, while holes migrate from the Bi₂S₃ VB to the In₂S₃ VB to react with the sacrificial agent, suppressing carrier recombination and S²⁻ oxidation. The exceptional H₂-evolution performance of this system is directly ascribed to the synergistic contributions of Bi₂S₃'s broad-spectral response, the rapid electron-transfer capability of the MOF-derived In₂S₃, and the intimate heterointerface formed between Bi₂S₃ and In₂S₃, which collectively enhance the photocatalytic activity of the In₂S₃/Bi₂S₃ composite. This effectively suppresses charge recombination and accelerates interfacial reaction kinetics, offering a fresh strategy for designing highly efficient and stable Bi₂S₃-based photocatalytic hydrogen-evolution systems. In terms of morphology and heterojunction construction, it also provides an innovative approach for tailoring unique photocatalysts dedicated to hydrogen production.

5.4. Photocatalytic CO₂ reduction

Since 2019, bismuth-based semiconductors have moved to the forefront of solar-fuel research because of their earth abundance, suitable band positions and visible-light response. Among them, Bi₂S₃ possesses a narrow band gap (~1.3 eV), high absorption coefficient ($\approx 10^5$ cm⁻¹) and a CB close to the CO₂/CH₄ potential, making it a promising candidate for visible-light-driven CO₂ reduction.²⁵ Stand-alone Bi₂S₃, however, suffers from ultrafast electro-hole recombination and a scarcity of surface reductive sites, leading to low selectivity and limited multi-electron kinetics.⁹⁴

Topological transformation of single-crystal Bi₂O₂S nanosheets yielded Bi₂S₃ nanorods that selectively reduce CO₂ to CH₄ under visible light,⁹⁵ while directly synthesized Bi₂S₃ nanobelts produce CH₃OH with enhanced activity⁹⁶ (Fig. 28 a-c). Beyond

shape control, heterojunction engineering has become the central strategy. An In₂O₃/Bi₂S₃ Z-scheme achieves spatial charge separation and delivers CO as the major product⁹⁷ (Fig. 28d-f), whereas a Bi/Bi₂S₃/TiO₂ S-scheme introduces a photothermal-photonic synergy. It significantly enhances CO₂ reduction performance, proving that constructing heterojunctions is an effective strategy to promote CO₂ reduction. It is worth considering that future heterojunction designs should go beyond simply choosing Z-type or S-type configurations, and instead focus more on precise control of interface states and a comprehensive analysis of carrier dynamics, in order to prevent the interface from becoming a new center for charge recombination. For example, Bi/Bi₂S₃/TiO₂ system designed by Lu *et al.*, introduced a photothermal synergistic effect⁹⁸ (Fig. 28g-i). It utilizes the LSPR effect of Bi nanoparticles to generate hot electrons, confirming that the photothermal-photonic synergistic mechanism is highly compatible. This study breaks through the limitations of traditional photocatalysis, providing a new pathway to solve critical problems and potentially surpassing the traditional photocatalytic activity limits. It signifies that research is shifting from a pure photon-driven paradigm to a multi-energy-field coupling paradigm, which may be an effective approach to addressing key issues such as low visible light utilization efficiency and slow reaction kinetics.

Despite remarkable progress, Bi₂S₃-based CO₂ photocatalysts still face severe challenges: (i) product selectivity control, (ii) suppression of both bulk and interfacial charge recombination, and (iii) long-term chemical stability under reducing atmospheres.⁹⁴ Future research may necessitate a shift from passive characterization to active design. On the one hand, theoretical calculations and *in situ* characterization techniques



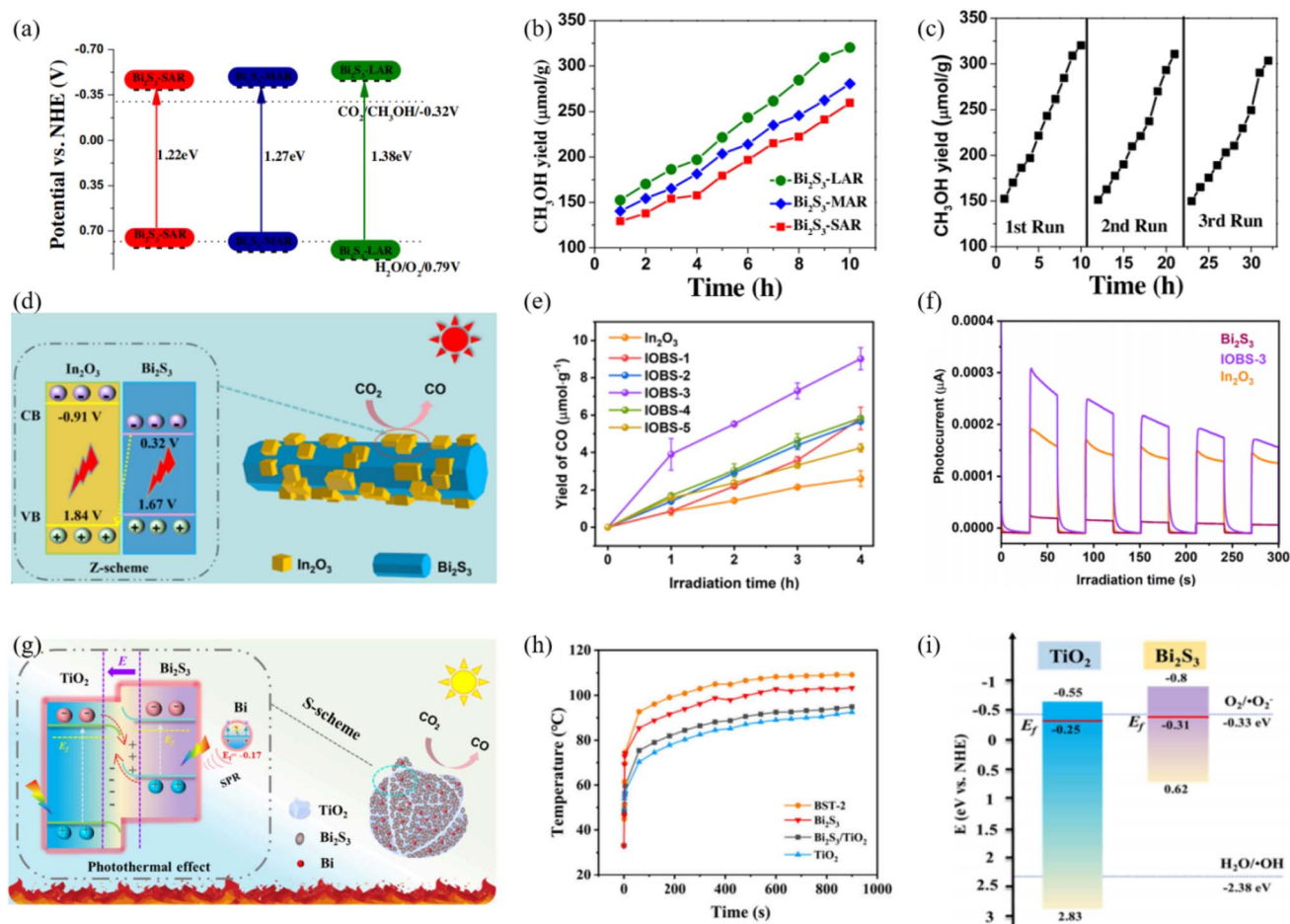


Fig. 28 (a) Energy level alignment and bandgap energy of Bi₂S₃ together with redox potential of CO₂/CH₃OH and H₂O/O₂ at pH = 7. (b) Photocatalytic CH₃OH evolution from Bi₂S₃ nanoribbons under 10 h irradiation. (c) Cycling curve of photocatalytic CH₃OH production over the Bi₂S₃ nanoribbons.⁹⁶ Copyright 2017, Elsevier. (d) Schematic illustration of photocatalytic CO₂ reduction over IOBS-3. (e) CO production curves of In₂O₃ and IOBS-X along with (f) transient photocurrent responses.⁹⁷ Copyright 2024, American Chemical Society. (g) Diagram of a possible photothermal catalytic mechanism of BST-2 composites. (h) Temperature profiles of various samples under light irradiation. (i) Energy band structure diagram of the prepared samples.⁹⁸ Copyright 2025, American Chemical Society.

can be employed to establish structure-activity relationship maps spanning from atomic-level active site structures to macroscopic catalytic performance. On the other hand, rational selection and design of co-catalysts can achieve high selectivity in CO₂ photocatalytic reduction.²⁵ Subsequent research may focus on novel co-catalysts exhibiting enhanced synergistic effects with bismuth substrates, such as single-atom or defect-engineered co-catalysts, to achieve precise adsorption and activation of key reaction intermediates. Only through such synergistic efforts will Bi₂S₃-based systems realize efficient, selective and durable solar CO₂ reduction.

5.5. Photoelectrochemical hydrolysis

Bi₂S₃ films can serve as photoanodes capable of directly converting solar energy into hydrogen energy. Elemental doping and morphology control form the cornerstone for optimizing the intrinsic properties of Bi₂S₃ photoanodes, though challenges such as photocorrosion and interfacial charge transport resistance should be effectively addressed. Chalapathi *et al.*

systematically investigated the effects of Sb doping⁹⁹ and Cu doping¹⁰⁰ on the photoelectrochemical (PEC) performance of Bi₂S₃ nanorod films. They found that both dopants effectively optimize the electrical properties and band structure of Bi₂S₃ nanorod films. Moreover, the Sb³⁺ substitution for Bi³⁺ introduces additional holes, increasing carrier concentration. This significantly enhanced photocurrent density and PEC stability. By modulating the Fermi level and conductivity of material through foreign atoms, this work optimized carrier injection efficiency and setting a new record for Bi₂S₃ photoanodes. Furthermore, Bi₂S₃ nanorod films grown using seed-layer-assisted techniques exhibit superior crystallinity and tighter substrate contact,¹⁰¹ drastically reducing interfacial contact resistance. This provides an efficient pathway for rapid charge transport, maintaining activity without degradation during continuous operation for 4 h, thereby achieving highly efficient photocatalytic water splitting performance. These studies confirm the critical role of interface engineering in enhancing PEC stability. When single-material modifications struggle to simultaneously satisfy all



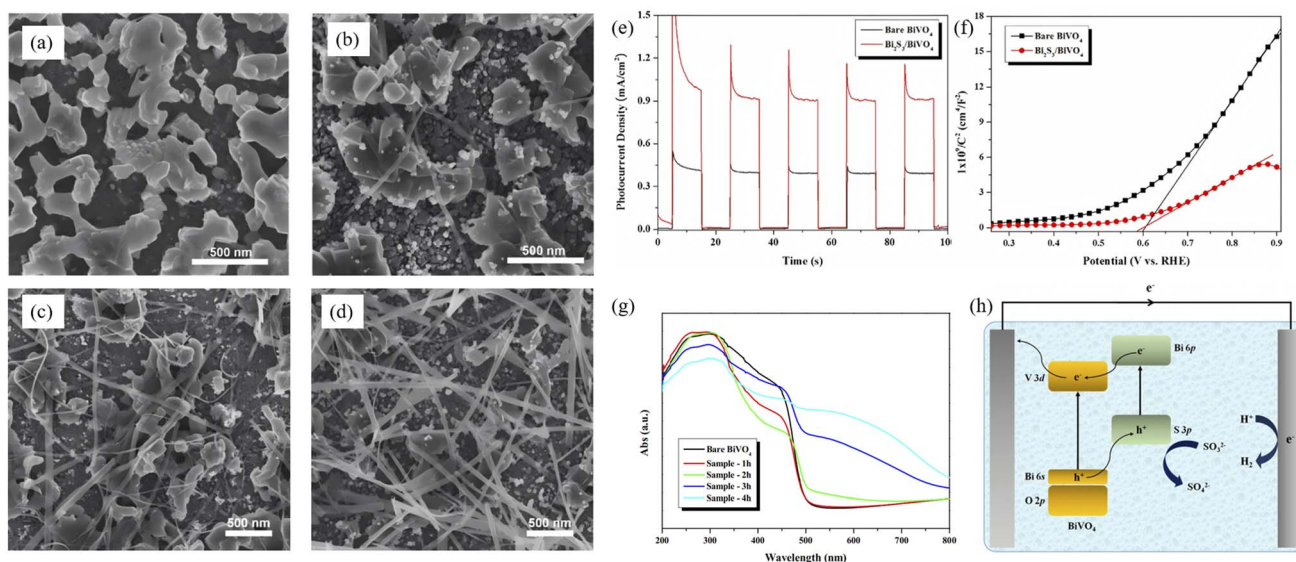


Fig. 29 (a–d) SEM images of $\text{Bi}_2\text{S}_3/\text{BiVO}_4$ hybrid electrodes of (a) sample-1 h; (b) sample-2 h; (c) sample-3 h; and (d) sample-4 h. (e) Photocurrent density and (f) Mott–Schottky plots of the as-prepared photoelectrodes measured in a 0.2 M Na_2SO_3 solution (pH = 8). (g) DRS spectra of the bare BiVO_4 photoelectrode and the $\text{Bi}_2\text{S}_3/\text{BiVO}_4$ hybrid photoelectrodes with various hydrothermal time. (h) Energy band structure of the hybrid $\text{Bi}_2\text{S}_3/\text{BiVO}_4$ photoelectrode and charge transfer pathway in the PEC hydrogen production under solar light irradiation.¹⁰² Copyright 2020, Elsevier BV.

requirements for light absorption, charge separation, and surface reactions, constructing heterojunctions has become an inevitable technical pathway, effectively promoting the separation of photo-generated electron–hole pairs. For instance, coupling Bi_2S_3 with BiVO_4 to form a $\text{Bi}_2\text{S}_3/\text{BiVO}_4$ heterojunction photoanode¹⁰² perfectly exemplifies the “complementary advantages” design philosophy (Fig. 29). Bi_2S_3 serves as a spectral sensitizer, extending the photoresponse of BiVO_4 up to 900 nm. The Type-II band alignment drives holes toward the BiVO_4 VB while electrons travel along the Bi_2S_3 CB to the external circuit, enabling bidirectional and ultrafast separation of photogenerated holes and electrons. This synergistic effect is the key to achieving a multiple performance enhancement. Through elemental doping, morphology engineering, and heterojunction construction, the light-harvesting, charge-separation, and charge-transport efficiencies of Bi_2S_3 -based photoanodes can be markedly enhanced. The critical levers are boosting electrical conductivity, lowering interfacial resistance, and establishing rapid charge-extraction pathways, all of which collectively upgrade their PEC water-splitting performance. Nevertheless, guaranteeing long-term chemical stability remains a central challenge that future research must continuously address and resolve.

5.6. Photocatalytic sterilization

The core bactericidal mechanism of Bi_2S_3 photocatalysis relies on the irreversible destruction of microbial cell structures by reactive oxygen species (ROS, $\cdot\text{OH}$, $\cdot\text{O}_2^-$, H_2O_2) generated through photo-induced charge carriers.¹⁰³ However, the rapid recombination of photogenerated electrons and holes in bare Bi_2S_3 limits its disinfection efficiency. Recent research frontiers therefore focus on constructing sophisticated heterojunction

systems that synergize multiple sterilization pathways to dramatically boost performance.

Constructing a Z-scheme heterojunction is the pivotal strategy for simultaneously optimizing charge separation and preserving strong redox capacity. For instance, a MXene/ TiO_2 / Bi_2S_3 Z-scheme system was fabricated by a facile hydrothermal oxidation followed by ultrasonic dispersion, anchoring TiO_2 nanoparticles and Bi_2S_3 microspheres uniformly on MXene nanosheets¹⁰⁴ (Fig. 30). DFT calculations and electron-spin-resonance (ESR) spectroscopy unambiguously confirm that the Z-scheme architecture retains the highly oxidative holes in the TiO_2 VB (+2.46 eV vs. NHE), enabling the generation of $\cdot\text{OH}$ radicals from H_2O without any detectable $\cdot\text{O}_2^-$ radicals. These $\cdot\text{OH}$ radicals disrupt bacterial cell membranes, diminish enzymatic activity and ultimately arrest cellular metabolism. The apparent reaction-rate constants toward *Escherichia coli* (*E. coli*) and *Staphylococcus aureus* (*S. aureus*) reach 8.4 times and 6.7 times those of pristine MXene, respectively. A $\text{Bi}_2\text{S}_3/\text{CdS}$ heterojunction,¹⁰⁵ prepared in *N,N*-dimethylformamide (BCDMF) was verified by EPR to be a Z-scheme type photocatalyst that generates abundant $\cdot\text{O}_2^-$ (no $\cdot\text{OH}$ signal detected) under visible light (Fig. 31). These $\cdot\text{O}_2^-$ radicals directly attack the *E. coli* membrane, causing intracellular content leakage. That is, a 100% kill rate is achieved within 60 min for *E. coli* and 93.85% within 100 min for *S. aureus*. Beyond efficient spatial separation of photo-carriers, the Z-scheme preserves the strong redox potentials of both holes and electrons, sustaining a high flux of ROS for potent bacterial inactivation and demonstrating the universal applicability of Z-scheme architectures against drug-resistant strains. A prominent current trend is the shift from a single-mechanism paradigm to multi-mechanism synergy. ROS attack alone is often insufficient against biofilms or deep-



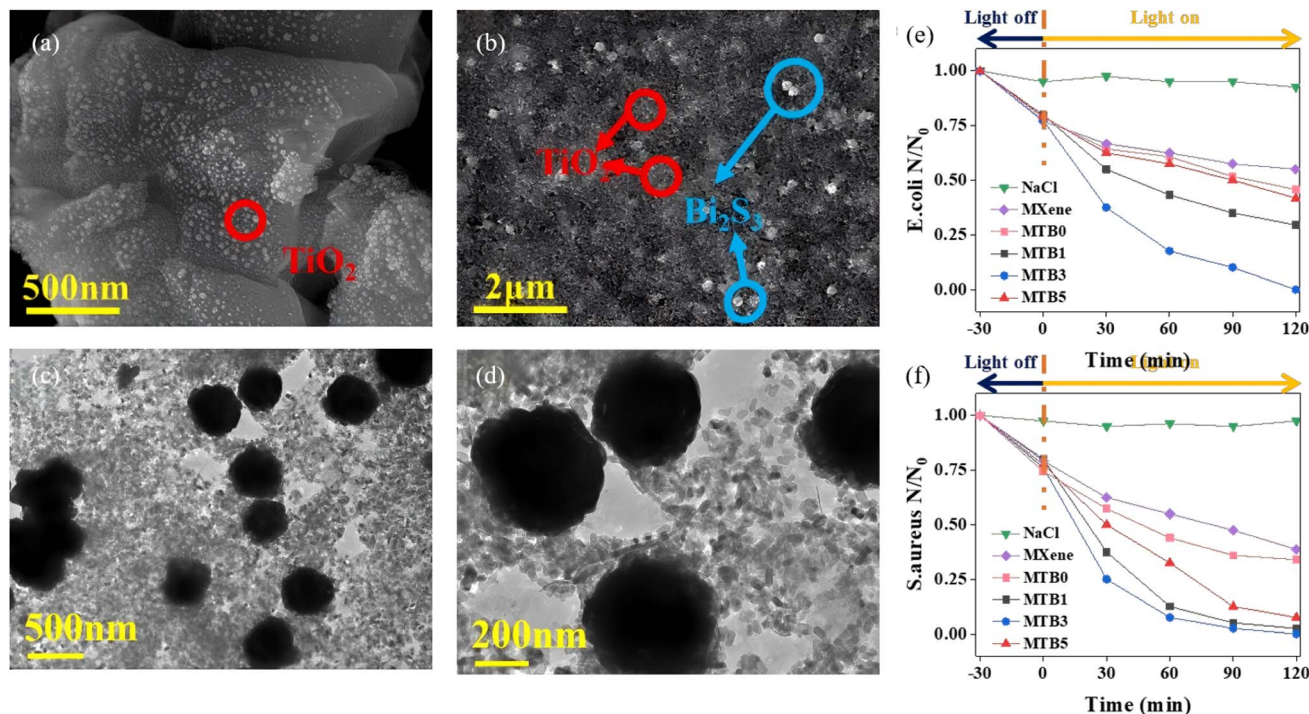


Fig. 30 SEM images of (a) MTB0 and (b) MTB3. (c and d) TEM images of MTB3. Photocatalytic sterilization performances of different samples against (e) *E. coli* and (f) *S. aureus* under visible light irradiation.¹⁰⁴ Copyright 2022, Elsevier.

seated infections. Addressing this, Feng *et al.*,¹⁰⁶ engineered a BiOI@Bi₂S₃/MXene heterostructure *via in situ* sulfidation to create intimate interfacial contact, ingeniously coupling the outstanding photothermal conversion of Bi₂S₃ (57.8% efficiency, temperature rising to 86.1 °C under 808 nm irradiation) with the robust photocatalytic activity of the heterojunction. The locally generated heat not only directly disrupts bacterial structures but also accelerates metabolic activity, rendering the bacteria more susceptible to ROS and thereby enabling efficient eradication of drug-resistant strains and biofilms. Meanwhile, the Z-scheme preserves highly oxidative holes that continuously produce $\cdot\text{OH}$ and H₂O₂. Under the synergistic action of photothermal therapy (PTT) and photodynamic therapy (PDT), bactericidal rates against *Pseudomonas aeruginosa* and *S. aureus* reach 99.7% and 99.8%, respectively, while cytotoxicity assays reveal no appreciable damage to mammalian cells.

Therefore, constructing Z-scheme heterojunctions to optimize charge separation while synergizing PTT and PDT effects is an effective strategy for boosting the photocatalytic antimicrobial performance of Bi₂S₃-based materials. Future breakthroughs must tackle the central challenges of safety, long-term stability, and adaptability to complex real-world environments that arise during practical deployment.

6. Challenges and future prospects

6.1. Key challenges at present

6.1.1. Fundamental improvement in photostability. Although Bi₂S₃ has demonstrated great potential in various photochemical energy applications, its intrinsic material

instability severely constrains practical deployment and commercialization. Foremost among the current challenges is the fundamental improvement of its photostability and chemical stability. The instability of Bi₂S₃ is manifested by the photo-oxidation of S²⁻ ions by photogenerated holes under illumination, leading to self-photocorrosion, loss of active components, and rapid performance degradation.¹⁰⁷ By inserting a hole-intercepting Type-II or Z-scheme heterojunction, the holes are rapidly shuttled to a wide-band-gap oxygen-containing semiconductor (TiO₂, BiVO₄), leaving the Bi₂S₃ side electron-rich. This was the first quantitative demonstration that a heterojunction can completely block the self-oxidation pathway.¹⁰⁷ Encapsulating Bi₂S₃ with a thin polymer overlayer creates an interfacial passivation layer that serves as a physical barrier: It not only blocks ambient O₂ and H₂O from reaching the sulfide surface, thereby suppressing indirect photocorrosion (O₂ + e⁻ → $\cdot\text{O}_2^-$, followed by S²⁻ oxidation), but also impedes hole migration to the surface, markedly lowering the probability of S²⁻/hole contact. This molecular-level protective shield thus isolates the material from both oxygen and holes.¹⁰⁸⁻¹¹⁰ Alternatively, self-healing can be engineered by creating reversible sulfur vacancies or an external sulfur reservoir that compensates for sulfur loss *in situ*, and recent work has already demonstrated the feasibility of this self-repair concept.

These combined strategies have already cut the photocorrosion rate of Bi₂S₃ by an order of magnitude, furnishing a generic stability-design framework that enables narrow-band-gap photocatalysts to operate outdoors for extended periods. Future research must therefore mount a concerted attack, ranging from intrinsic structural stabilization of the material



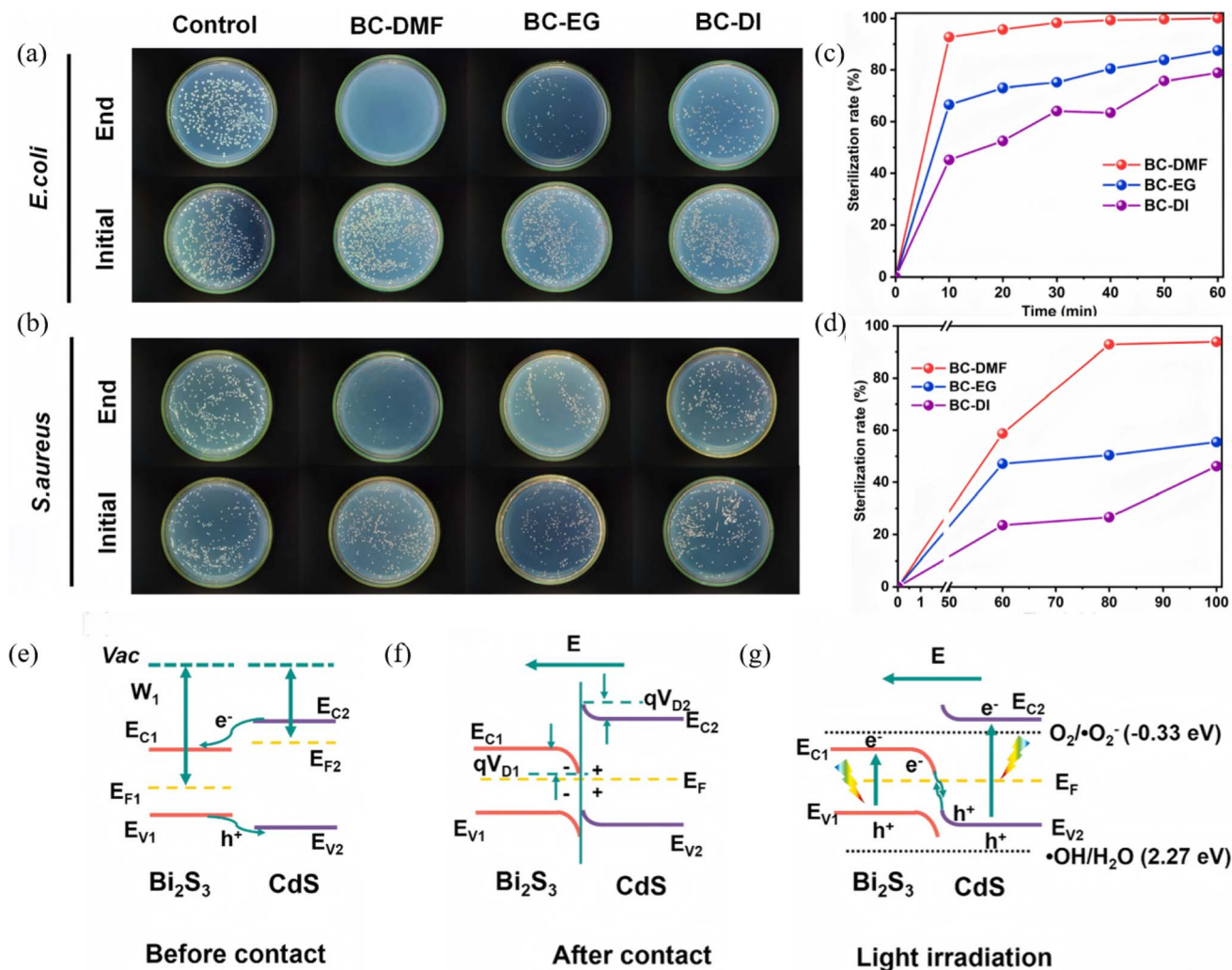


Fig. 31 Photographs of (a) *E. coli* and (b) *S. aureus* bacterial colonies sterilized by different photocatalysts under light irradiation under 100 min light irradiation and the effect of irradiation time on antimicrobial behavior against (c) *E. coli* and (d) *S. aureus*. The edge bending at the interface of Bi₂S₃/CdS (e) before and (f) after contact. (g) Charge transfer mechanism between Bi₂S₃ and CdS under light irradiation.¹⁰⁵ Copyright 2021, Elsevier.

itself to advanced interfacial passivation engineering, to deliver truly definitive solutions.

6.1.2. Further boosting charge-separation efficiency.

Despite its exceptional visible-light harvesting capability, Bi₂S₃ suffers from an intrinsically high carrier-recombination rate that severely limits the usable fraction of photogenerated electron-hole pairs, constituting a key bottleneck to higher photocatalytic performance. Present research shows that engineering multi-component heterojunctions has become the mainstream route for pushing charge-separation efficiency to the next level.

In recent years, heterojunction design has evolved from simple binary systems toward more sophisticated and multi-functional architectures. Current efforts focus on precise band-alignment and interface engineering to create multi-component heterojunctions such as dual S-scheme or Z-scheme systems with directional charge-transfer pathways that maximize the separation and utilization of photogenerated carriers. Harnessing tunable multi-component heterojunctions,

integrating synergistic mechanisms, and deploying *operando* characterization technology collectively constitute an effective approach to overcoming the inherent charge separation limitations of Bi₂S₃. Yet this progress introduces fresh challenges, that is, as junction architectures grow increasingly complex, *in situ* tracking and precise control of interfacial charge-transfer pathways become ever more demanding. Future efforts must therefore delve deeper into the charge-kinetics of these multi-ary systems, striving to maximize separation efficiency while simultaneously minimizing interfacial transport resistance, which is an essential step toward a fundamental breakthrough in charge-utilization efficiency.

6.2. Future research directions

To break the fundamental limits of Bi₂S₃-based materials in both efficiency and stability, the next frontier is to assemble ternary or even higher-order heterojunction architectures in which multiple mechanisms cooperate in light harvesting, charge separation,



and surface reaction. Rather than solving one bottleneck at a time, future designs must choreograph carrier generation, separation, transport, and utilization within a single platform. This demands the seamless integration of elemental doping, heterojunction engineering, surface functionalization, and external-field effects (*e.g.*, photothermal, piezoelectric, plasmonic, *etc.*). By coupling and amplifying these multi-mechanistic and multi-functional roles, Bi₂S₃-based artificial photosystems can be propelled toward step-change advances in energy, environmental, and optoelectronic applications.

7. Conclusions

This review summarizes the research progress of Bi₂S₃-based photocatalysts from 2019 to 2025, systematically collating their fundamental properties and controllable syntheses, and further clarifying optimization strategies. It then surveys their practical applications, charting a path from traditional pollutant degradation to CO₂ reduction, N₂ fixation, PEC H₂ evolution and antibacterial use, realizing high-value, multi-scenario deployment. Bi₂S₃-based photocatalysis has already leapt from material exploration to large performance gains, and thus future work must uncover performance truths at the atomic and electronic scale, dissect synergistic mechanisms with atomic precision, and finally transform Bi₂S₃ photocatalysts from “paper results” into “real-world products.” toward high-efficiency solar energy conversion.

Author contributions

Wei Zhao and Qing Chen wrote the manuscript and they contributed equally to this work. Jie Liang provided helps for organizing the graphs. Lifeng Cai and Fang-Xing Xiao guided this work and helped correct the manuscript.

Conflicts of interest

There are no conflicts to declare.

Data availability

No primary research results, software or code have been included and no new data were generated or analysed as part of this review.

Acknowledgements

The support by the award Program for the Minjiang scholar professorship is greatly acknowledged. This work was financially supported by the National Natural Science Foundation of China (No. 21703038, 22072025). The financial support from the State Key Laboratory of Structural Chemistry, Fujian Institute of Research on the Structure of Matter, Chinese Academy of Science is acknowledged (No. 20240018). Fujian Natural Science Foundation (No. 2024J01263), Open Project of Fujian Key Laboratory of Ecological Impacts and Treatment Technologies for Emerging Contaminants (No. PY25002) and the Research

Project of Putian University (No. 2024034, yjs2025038) are greatly acknowledged.

References

- 1 F. H. Xu and B. C. Weng, *J. Mater. Chem. A*, 2023, **11**, 4473–4486.
- 2 S. Yaghoubi, S. M. Mousavi, A. Babapoor, M. Binazadeh, C. W. Lai, R. H. Althomali, M. M. Rahman and W. H. Chiang, *Renew. Sustain. Energy Rev.*, 2024, **200**, 114538.
- 3 Y. Huang, J. F. Zhang, O. Ruzimuradov, S. Mamatkulov, K. Dai and J. X. Low, *Compos. Funct. Mater.*, 2025, **1**, 20250103.
- 4 Y. Shi, A. F. Yang, C. S. Cao and B. Zhao, *Coord. Chem. Rev.*, 2019, **390**, 50–75.
- 5 T. Y. Li, P. Wang, M. He, T. B. Zhang, C. Yang and Z. X. Li, *Coord. Chem. Rev.*, 2024, **521**, 216179.
- 6 K. Li, Y. Gao, Z. X. Dong, H. B. Zhang, X. D. Fan, L. Xu, J. Huang, F. Teng, H. B. Fan, J. M. Song, C. M. Zhang, X. X. He and P. Hu, *Environ. Res.*, 2024, **263**, 120209.
- 7 H. Y. Zhao, S. Wang, H. Y. Zhu, X. X. Zhang, D. H. Shang, X. W. Zhou, J. Wang, C. Z. Zhu, F. Du, Y. Y. Song and F. Yang, *Rare Met.*, 2024, **43**, 5905–5920.
- 8 K. Maeda and K. Domen, *J. Phys. Chem. Lett.*, 2010, **1**, 2655–2661.
- 9 I. Arora, H. Chawla, A. Chandra, S. Sagadevan and S. Garg, *Inorg. Chem. Commun.*, 2022, **143**, 109700.
- 10 A. Sienkiewicz, A. Wanag, E. Kusiak-Nejman, E. Ekiert, P. Rokicka-Konieczna and A. W. Morawski, *J. Environ. Chem. Eng.*, 2021, **9**, 104794.
- 11 Y. Chen, A. Li, X. L. Fu and Z. J. Peng, *Appl. Surf. Sci.*, 2023, **613**, 155970.
- 12 D. H. Huang, T. F. Wu, D. Y. Xie, H. N. Che and Y. H. Ao, *Compos. Funct. Mater.*, 2025, **1**, 20250104.
- 13 H. Park, Y. Park, W. Kim and W. Choi, *J. Photochem. Photobiol. C: Photochem. Rev.*, 2013, **15**, 1–20.
- 14 J. Y. Tang, J. Y. Pang, X. X. Lv and X. L. Wang, *ACS Appl. Energy Mater.*, 2025, **8**, 9683–9690.
- 15 L. Zhang, Z. Z. Ai, X. L. Xu, D. Shi, B. G. Zhang, H. X. Hu, M. Z. Yang, Y. L. Shao, Y. Z. Wu and X. P. Hao, *Ionics*, 2023, **29**, 2115–2139.
- 16 A. Chawla, A. Sudhaik, R. Kumar, P. Raizada, T. Ahamad, A. A. P. Khan, Q. V. Le, V. Nguyen, S. Thakur and P. Singh, *Coord. Chem. Rev.*, 2025, **529**, 216443.
- 17 W. Cao, M. Wang, J. Yang, B. Han, X. C. Zhu and Y. P. Wang, *J. Solid State Chem.*, 2022, **312**, 123172.
- 18 J. P. Li, B. Wang, T. Wang, Y. Zhao, T. Song, L. N. Zhang and X. Cheng, *J. Alloys Compd.*, 2020, **831**, 154829.
- 19 J. H. Wang, Y. Yang, X. J. Ye, W. Ren, L. Li, X. Z. Zheng, J. B. Ge, S. J. Zhang and S. F. Chen, *J. Am. Ceram. Soc.*, 2025, **108**, e20289.
- 20 B. Xing, T. Wang, X. B. Han, K. Zhang and B. X. Li, *J. Colloid Interface Sci.*, 2023, **650**, 1862–1870.
- 21 K. Yan, D. H. Wu, T. Wang, C. Chen, S. J. Liu, Y. G. Hu, C. Gao, H. Y. Chen and B. X. Li, *ACS Catal.*, 2023, **13**, 2302–2312.



- 22 M. Miodynska, A. Mikolajczyk, B. Bajorowicz, J. Zwara, T. Klimczuk, W. Lisowski, G. Trykowski, H. P. Pinto and A. Zaleska-Medynska, *Appl. Catal. B: Environ.*, 2020, **272**, 118962.
- 23 Q. F. Jia, M. Li and W. J. Sun, *Dalton Trans.*, 2025, **54**, 13703–13711.
- 24 P. Shen, N. Li, A. M. Nasser, B. Zhu, X. Xi, L. J. She, Y. F. Liu and J. Q. Ma, *Langmuir*, 2024, **40**, 20228–20239.
- 25 X. Li, J. G. Yu, M. Jaroniec and X. B. Chen, *Chem. Rev.*, 2019, **119**, 3962–4179.
- 26 X. Xing, L. X. Zhang, Y. Ren, Y. F. Li, H. Yu and W. W. Shi, *J. Environ. Chem. Eng.*, 2024, **12**, 112122.
- 27 A. Kyono and M. Kimata, *Am. Mineral.*, 2004, **89**, 932–940.
- 28 Q. Hao, C. Xie, Y. M. Huang, D. M. Chen, Y. W. Liu, W. Wei and B. J. Ni, *Chin. J. Catal.*, 2020, **41**, 249–258.
- 29 A. A. Al Anazi, M. Treve, A. Ali, A. Albaker, A. K. Kareem, S. Jain, A. S. Altamimi, R. M. Romero-Parra, I. H. Al-Kharsan and M. S. Alhassan, *Mater. Res. Bull.*, 2023, **166**, 112336.
- 30 L. W. McKeehan, *J. Frankl. Inst.*, 1923, **195**, 59–66.
- 31 H. Zhang and L. J. Wang, *Mater. Lett.*, 2007, **61**, 1667–1670.
- 32 M. P. Deshpande, P. N. Sakariya, S. V. Bhatt, N. Garg, K. Patel and S. H. Chaki, *Mater. Sci. Semicond. Process.*, 2014, **21**, 180–185.
- 33 M. Escoda-Torroella, C. Moya, J. A. Ruiz-Torres, A. F. Rodríguez, A. Labarta and X. Batlle, *Phys. Chem. Chem. Phys.*, 2023, **25**, 3900–3911.
- 34 E. Zahedi, *Superlattices Microstruct.*, 2015, **81**, 49–63.
- 35 W. Yan, X. Chen, Z. Q. Wang, Z. Y. Zhao, Y. Liu and A. Muhammad, *Chem. Eng. J.*, 2025, **504**, 158864.
- 36 D. Yi, X. Chen, W. F. Cai and L. C. Li, *Surf. Sci.*, 2025, **762**, 122832.
- 37 J. S. Chen, S. Y. Qin, G. X. Song, T. Y. Xiang, F. Xin and X. H. Yin, *Dalton Trans.*, 2013, **42**, 15133–15138.
- 38 H. Li, X. T. Wang, Q. Y. Wei and B. R. Hou, *Nanoscale Res. Lett.*, 2017, **12**, 80.
- 39 Y. T. Chen, W. X. Xia, Y. Zhou, Q. R. Zhang, X. B. Chen, L. Ma and S. J. Ding, *J. Environ. Chem. Eng.*, 2025, **13**, 115147.
- 40 J. Jiang, X. Che, Y. W. Qian, L. Z. Y. Wang, Y. Zhang and Z. L. Wang, *Front. Mater.*, 2020, **7**, 234.
- 41 R. Joy, B. Meena, M. Kumar, M. Joseph, S. Joseph, C. Subrahmanyam and S. Haridas, *Catal. Today*, 2024, **433**, 114669.
- 42 Y. W. Xiao, M. Y. Li, H. Y. Li, Z. Z. Wang and Y. D. Wang, *Nano Energy*, 2024, **120**, 109164.
- 43 Z. P. Liu, S. Peng, Q. Xie, Z. K. Hu, Y. Yang, S. Y. Zhang and Y. T. Qian, *Adv. Mater.*, 2003, **15**, 936–940.
- 44 L. J. Yang, Y. D. Hu and L. Zhang, *Chem. Eng. J.*, 2019, **378**, 122092.
- 45 Y. Sang, X. Cao, G. D. Dai, L. X. Wang, Y. Peng and B. Y. Geng, *J. Hazard. Mater.*, 2020, **381**, 120942.
- 46 L. J. Wang, S. Karuturi and L. Zan, *Small*, 2021, **17**, 2101833.
- 47 T. Wu, X. G. Zhou, H. Zhang and X. H. Zhong, *Nano Res.*, 2010, **3**, 379–386.
- 48 S. A. Saah, M. Afzaal and P. O'Brien, *Results Chem.*, 2022, **4**, 100618.
- 49 Y. Lu, J. M. Song, W. F. Li, Y. L. Pan, H. Y. Fang, X. L. Wang and G. Hu, *Appl. Surf. Sci.*, 2020, **506**, 145000.
- 50 H. B. Huang, N. Zhang, J. Y. Xu, Y. H. Xu, Y. F. Li, J. Lü and R. Cao, *Research*, 2022, **2022**, 9805879.
- 51 F. Xu, C. Y. Xu, H. M. Chen, D. P. Wu, Z. Y. Gao, X. M. Ma, Q. Zhang and K. Jiang, *J. Alloys Compd.*, 2019, **780**, 634–642.
- 52 W. H. Li, *Mater. Lett.*, 2008, **62**, 243–245.
- 53 M. Godzierz, K. Mistewicz, A. Gawron, K. Kurtyka, L. Otulakowski and T. K. Das, *J. Alloys Compd.*, 2024, **1008**, 176820.
- 54 D. L. Dai, J. H. Qiu, G. L. Xia, Y. Tang, Q. Y. Liu, Y. X. Li, B. Y. Fang and J. F. Yao, *Small*, 2024, **20**, 2307654.
- 55 Y. W. Mi, H. P. Li, X. Yu, Y. F. Zhang, S. Y. Zeng, L. Wang and W. G. Hou, *Appl. Surf. Sci.*, 2024, **655**, 159573.
- 56 I. Uddin, S. M. Abzal, K. Kalyan, S. Janga, A. Rath, R. Patel, D. K. Gupta, T. R. Ravindran, H. Ateeq, M. S. Khan and J. K. Dash, *ACS Omega*, 2022, **7**, 42438–42445.
- 57 Y. P. Li, J. L. Chen, S. Chen, T. T. Lu, X. L. Liao, T. T. Zhao, F. Y. Cheng and H. Wang, *Mater. Rep.*, 2020, **34**, 15033–15038.
- 58 C. J. Liu, Y. Yang, W. Z. Li, J. Li, Y. M. Li and Q. Y. Chen, *Chem. Eng. J.*, 2016, **302**, 717–724.
- 59 J. Arumugam, A. George, X. Venci, A. D. Raj, A. A. Irudayaraj, R. L. Josphine, S. J. Sundaram, W. A. Al-onazi, A. M. Al-Mohaimeed, T. W. Chen and K. Kaviyarasu, *J. Alloys Compd.*, 2022, **902**, 163785.
- 60 K. A. Messalea, A. Zavabeti, M. Mohiuddin, N. Syed, A. Jannat, P. Atkin, T. Ahmed, S. Walia, C. F. McConville, K. Kalantar-Zadeh, N. Mahmood, K. Khoshmanesh and T. Daeneke, *Adv. Mater. Interfaces*, 2020, **7**, 2001131.
- 61 Y. Z. Li, J. L. Chen, S. Chen, T. T. Lu, X. L. Liao, T. T. Zhao, F. Y. Cheng and H. Wang, *Appl. Catal. B: Environ. Energy*, 2024, **349**, 123874.
- 62 R. T. Zhou, X. M. Tu, P. Zheng, L. Zhang and Z. X. Zeng, *Molecules*, 2023, **28**, 8007.
- 63 X. Y. Lian, J. G. Zhang, Y. Zhan, Y. P. Zhang, S. L. Yang, Z. Chen, Y. Y. Dong, W. P. Fang and X. D. Yi, *J. Hazard. Mater.*, 2021, **406**, 124705.
- 64 C. C. Dang, S. X. He, Y. P. Liu, L. C. Zhao, A. D. Shan, M. Li, L. T. Kong and L. M. Gao, *Chem. Eng. J.*, 2023, **476**, 146775.
- 65 Z. H. Yuan, M. Tuerhong, X. Aisikaer and G. Mamtmin, *Appl. Organomet. Chem.*, 2025, **39**, e70021.
- 66 X. Y. Fan, H. O. Liang, M. Zhang, C. P. Li and J. Bai, *Colloids Surf. A: Physicochem. Eng. Aspects*, 2025, **707**, 135929.
- 67 Z. Z. Guo, Z. J. Ren, H. M. Gao, J. F. Guan, R. J. Zheng and P. Y. Li, *Appl. Surf. Sci.*, 2024, **644**, 158732.
- 68 A. Chachvalvutikul, W. Pudkon, T. Luangwanta, T. Thongtem, S. Thongtem, S. Kittiwachana and S. Kaowphong, *Mater. Res. Bull.*, 2019, **111**, 53–60.
- 69 J. Ke, J. Liu, H. Q. Sun, H. Y. Zhang, X. G. Duan, P. Liang, X. Y. Li, M. O. Tade, S. M. Liu and S. B. Wang, *Appl. Catal. B: Environ. Energy*, 2017, **200**, 47–55.
- 70 P. Latifian, S. F. Hosseini, M. S. S. Dorraji and M. H. Rasoulifard, *J. Mol. Liq.*, 2023, **376**, 121445.
- 71 S. F. Hosseini, M. S. S. Dorraji and M. H. Rasoulifard, *Compos. Part B: Eng.*, 2023, **262**, 110820.



- 72 Y. X. Sun, J. H. Li, Z. Y. Wang and H. C. Zhu, *J. Mater. Chem. A*, 2025, **13**, 30457–30466.
- 73 W. Zhou, Y. Li, H. X. Huang, J. Y. Wang and F. X. Zhong, *Mater. Sci. Semicond. Process.*, 2022, **143**, 106467.
- 74 V. M. Nkwe, O. C. Olatunde, Y. Ben Smida, S. M. Siddeeg and D. C. Onwudiwe, *Mater. Today Commun.*, 2023, **34**, 105418.
- 75 F. Y. Du, Z. Lai, H. Y. Tang, H. Y. Wang and C. X. Zhao, *Chemosphere*, 2022, **287**, 132391.
- 76 X. D. Shi, X. Y. Qin, X. Y. Yang, X. Y. Wei, Y. Liu, S. H. Li, G. X. Liu, J. X. Wang, X. T. Dong and F. H. Chen, *Mater. Today Chem.*, 2024, **41**, 102283.
- 77 M. Ganapathy, Y. Hsu, J. Thomas, L. Y. Chen, C. T. Chang and V. Alagan, *Energy Fuels*, 2021, **35**, 14995–15004.
- 78 T. T. H. Vu, T. A. T. Do, D. T. Nguyen, T. G. Ho, Q. N. Pham, H. T. Giang, M. H. Hoang, T. H. Nghiem, M. T. Man and D. L. Tran, *Results Mater*, 2022, **31**, 103541.
- 79 R. H. Zha, Y. H. Niu, C. Y. Liu, L. He and M. Zhang, *J. Environ. Chem. Eng.*, 2021, **9**, 106586.
- 80 M. Lan, X. L. Dong, N. Zheng, X. X. Zhang, Y. Wang and X. X. Zhang, *J. Mater. Sci. Technol.*, 2023, **167**, 237–247.
- 81 M. Lan, X. L. Dong, N. Zheng and Y. B. Zhang, *Chem. Eng. Sci.*, 2025, **311**, 121626.
- 82 Y. J. Zhu, Q. T. Han, H. Qu, Y. Shen, X. Zhou, Z. G. Zou and Y. Zhou, *Catal. Sci. Technol.*, 2024, **14**, 2876–2884.
- 83 N. Nwaji, E. M. Akinoglu and M. Giersig, *Catalysts*, 2021, **11**, 355.
- 84 H. Y. Liu, R. Wu, L. Tian, Y. Y. Kong, H. M. Fan, X. Yang and Y. F. Sun, *Mater. Lett.*, 2019, **246**, 214–218.
- 85 X. F. Qu, Z. Q. Gao, M. H. Liu, H. J. Zhai, L. Shi, Y. Li and H. B. Song, *Appl. Surf. Sci.*, 2020, **501**, 144047.
- 86 T. R. Hao, H. L. Xu, H. Yu, M. L. Li, B. Song, G. Shao, B. B. Fan, H. L. Wang, H. X. Lu and R. Zhang, *Sep. Purif. Technol.*, 2025, **360**, 131072.
- 87 M. U. Nisa, A. G. Abid, S. Gouadria, T. Munawar, Z. A. Alrowaili, M. Abdullah, M. S. Al-Buriah, F. Iqbal, M. F. Ehsan and M. N. Ashiq, *Surf. Interfaces*, 2022, **31**, 102012.
- 88 X. Q. Li, D. Y. Chen, N. J. Li, Q. F. Xu, H. Li, J. H. He and J. M. Lu, *J. Hazard. Mater.*, 2020, **400**, 123243.
- 89 H. W. Wang, Y. W. Zhu, M. K. Joshi, Y. Cheng, P. Y. Zhang, M. H. Tan, R. H. Yu, Z. P. Mao and X. L. Li, *Chem. Eng. J.*, 2024, **500**, 156640.
- 90 X. Q. Wang, F. Wang, B. Q. Xu and B. Yang, *Appl. Surf. Sci.*, 2025, **693**, 162748.
- 91 C. L. Wang, N. Z. Liu, X. Zhao, Y. Tian, X. W. Chen, Y. F. Zhang, L. Fan and B. R. Hou, *J. Mater. Sci. Technol.*, 2023, **164**, 188–197.
- 92 M. Chahkandi and M. Zargazi, *J. Hazard. Mater.*, 2019, **380**, 120879.
- 93 S. B. Liu, Y. J. Wang, Y. Z. Zhang, X. Xin, P. Guo, D. S. Deng, J. B. Ghasemi, M. Wang, R. L. Wang and X. H. Li, *Front. Energy*, 2023, **17**, 654–663.
- 94 G. Liao, H. Wang and J. Zhang, *Precis. Chem.*, 2024, **2**, 49–56.
- 95 L. S. Jiang, Y. Hu, K. Wang, C. Liang, C. Y. Liu, X. Q. Li, Y. Y. Jia and W. Liu, *Sep. Purif. Technol.*, 2023, **309**, 123039.
- 96 J. R. Jin and T. He, *Appl. Surf. Sci.*, 2017, **394**, 364–370.
- 97 M. F. Sun, K. Fan, C. Y. Liu, T. Gui, C. H. Dai, Y. S. Jia, X. Liu and C. Zeng, *Langmuir*, 2024, **40**, 12681–12688.
- 98 M. H. Lu, K. Zhang, D. M. Peng, M. Y. Luo, Y. Zhang and Y. M. Qin, *Langmuir*, 2025, **41**, 22345–22356.
- 99 U. Chalapathi, N. P. Reddy, S. Alhammadi, R. A. Alshgari, R. Dhanalakshmi, G. S. Reddy, S. Sangaraju, K. Mohanarangam, V. R. M. Reddy, C. H. Ahn and S. H. Park, *J. Solid State Chem.*, 2025, **342**, 125099.
- 100 U. Chalapathi, D. R. Cuddapah, P. B. Reddy, S. Alhammadi, R. A. Alshgari, D. Radhalayam, S. R. Golkonda, S. Sangaraju, K. Mohanarangam, V. Reddy and S. H. Park, *Opt. Mater.*, 2024, **157**, 116289.
- 101 U. Chalapathi, B. P. Reddy, R. Dhanalakshmi, G. S. Reddy, A. Divya, S. Sangaraju, S. Alhammadi, K. Mohanarangam, A. A. A. Bahajaj and S. H. Park, *Int. J. Hydrogen Energy*, 2025, **101**, 1085–1092.
- 102 F. Li and D. Y. C. Leung, *Chem. Eng. Sci.*, 2020, **211**, 115266.
- 103 L. F. Ge, W. Wang, F. T. Tan, X. Y. Wang, X. L. Qiao and P. K. Wong, *Sol. RRL*, 2023, **7**, 2300446.
- 104 H. M. Huang, J. F. Zhang, C. M. Tang, A. Y. Li, T. M. Zhang, H. P. Xue and D. F. Zhang, *J. Environ. Chem. Eng.*, 2022, **10**, 108654.
- 105 L. Y. Shi, Z. L. Ma, W. W. Qu, W. Zhou, Z. Q. Deng and H. F. Zhang, *Appl. Surf. Sci.*, 2021, **568**, 150923.
- 106 H. M. Feng, W. Wang, T. Wang, Y. A. Pu, C. C. Ma and S. G. Chen, *Acta Biomater.*, 2023, **171**, 506–518.
- 107 Y. H. Yan, Z. X. Zhou, W. Q. Li, Y. J. Zhu, Y. Cheng, F. Y. Zhao and J. G. Zhou, *RSC Adv.*, 2014, **4**, 38558–38567.
- 108 Z. P. Guo, W. Wei, Y. H. Li, Z. Y. Li, F. M. Hou and A. Wei, *J. Hazard. Mater.*, 2022, **422**, 126946.
- 109 Y. Sun, C. Liu, S. Ji, J. Ni, X. Wu, S. R. P. Silva, M. Cai, G. Shao and P. Zhang, *Compos. Funct. Mater.*, 2025, **1**, 20250202.
- 110 H. Zhang, Y. Fan, S. Guan, W.-G. Cui, M. Zhang, Z. Li, Y. Dou, J. Yang, Z. Zhuang, Z. Yuan, S. Zhao, D. Wang, B. Liu and H. Pan, *Compos. Funct. Mater.*, 2025, **1**, 20250201.

